Direct Numerical Simulation of Turbulence

U. Schumann
G. Grötzbach
L. Kleiser
Kernforschungszentrum Karlsruhe
Karlsruhe, West Germany

VKI-Course Contribution 1979, Hemisphere 1980

1. INTRODUCTION

1.1 The Subject

The intention of this paper is to describe methods for direct numerical simulation of turbulent incompressible flows - sometimes called "large-eddy simulations" - and to present various results of applications which show the usefulness and limitations of these methods. Both finite difference methods (FDM) and spectral methods (SM) will be described. For high Reynolds numbers the idea of "sub-grid scale" (SGS) models is explained. Most examples are taken from our own work.

Earlier surveys from different view points have been given by Fox & Lilly (1972), Fox & Deardorff (1972), Orszag (1974), Orszag & Israeli (1974), Schumann (1975 d), Reynolds (1976), Ferziger (1977) and Saffman (1978).

The objective of direct numerical simulation is to tackle the turbulence problem as far as possible from first principles. Viewing the Navier-Stokes equations as the simplest turbulence theory, one tries to follow the flow dynamics by direct numerical integration forward in time, starting from some suitable initial data (for example, data generated by random numbers). From the resultant flow fields, which are always three-dimensional and time-dependent even in simple geometries, and under statistically steady conditions, one can deduce afterwards any average one might be interested in.

1.2 The Resolution Barrier

Several years ago, this approach appeared much too time consuming to be feasible and there are simple obvious arguments for this pessimism: An intrinsic feature of turbulence is the huge ratio of largest to smallest relevant scales of flow at least at high Reynolds numbers. This ratio determines the required number of degrees of freedom N of the numerical flow field representation (e.g. grid points in finite difference schemes) in any of the three dimensions. The large scales, say of length L, are of the order of the geometrical size of the flow region in bounded flows or of the

size of the largest eddies in homogeneous turbulence. The smallest relevant length scale, say ℓ, can be either taken as the thickness of the viscous layer near walls or as the diameter of those eddies for which most of the viscous energy dissipation occurs. From different arguments (Schumann 1973 a, Orszag 1974) one obtains for large Reynolds numbers Re an estimate

$$N \approx L/\ell \approx Re^{n} \qquad (1 - 1)$$

with $n \approx 3/4$ for homogeneous turbulence and $7/8 \leq n \leq 1$ for channel flows if ℓ is taken as the thickness of the viscous sublayer (the upper limit of n applies for $Re > 10^6$). Thus the total number of spatial degrees of freedom is of order $N^3 \gtrsim Re^{9/4}$. In order to be useful, the calculation must proceed for a time of order L/U (U = characteristic maximum velocity), while time steps must be restricted to order ℓ/U, so that order Re^{n} time steps must be taken per simulation run. Consequently, the total number of operation scales as $Re^{4n} \gtrsim Re^{3}$. Taking $Re \approx 10^4$ and a grind time (i. e. computing time per degree of freedom and per time step, Hirt et al. 1978) which can be 0.1 ms on modern computers (Patterson 1978), this amounts to 10^8 s or about 3 years of computing time per one single run. So even with much faster computers "brute-force" numerical solutions of the equations of motion are out of discussion. Today computations with $N=32$ or 128 at most are feasible in which case the computer time will be of the order of a few hours to days.* In particular storage requirements prohibit larger values. If one is willing to spend about an hour computing time our estimate then gives $Re \approx 330$. At present, this is about the upper limit for straight-forward direct simulations.

1.3 Feasible Simulations

Two discoveries have been made, however, which allow to come around this resolution barrier:

a) Many properties of turbulence can well be studied already at rather low Reynolds numbers; this is true in particular with respect to turbulence decay.

* N is usually taken as a power of two in view of solution methods involving Fast Fourier Transforms (FFT), see Cooley & Tukey (1965).

b) The important large scale properties of a turbulent flow remain widely unchanged if rather crude models are introduced for the fine scales, i. e. for those scales which are smaller than the scales ℓ_o resolvable by the numerical scheme.

The first discovery means that in spite of all pessimistic estimates it is well worthwhile to study those cases which just can be resolved directly. The second says that after introduction of sub-grid scale models, which account for the scales not readily resolvable, the large scale flow becomes amenable to direct numerical treatment. These aspects are discussed further below.

1.3.1 Low Reynolds Number Simulations

Our resolution estimate for channel flow was based on taking the maximum velocity U as the characteristic one. This velocity is determined by the velocity profile. The turbulent fluctuations, however, amount to only a few percent of U . Typically they are of the order of $u_\tau \equiv (\tau_w/\varrho)^{1/2}$ (Hinze 1975) where τ_w is the wall shear stress and ϱ the density. Also, the most important part of a turbulent boundary layer extends over much smaller distances than the channel diameter. Typically, the range $L \approx 100\,\ell^*$ is the most interesting one, where $\ell^* \equiv \nu/u_\tau$ (ν = kinematic viscosity), so that the relevant Reynolds number is $L\,u_\tau/\nu \approx 100$.

Unfortunately, it is very difficult to define a computational domain including only the relevant boundary layer together with reasonable boundary conditions at the "free-stream" boundary. See Kollmann (1972) for further discussion.

Far away from walls it is much simpler to restrict the computational domain to a small part of the whole domain because it seems natural that turbulence is to some extent periodic in space. With such a periodicity assumption one is able to follow the development of an initially existing fluctuating flow in remarkable similarity to wind-tunnel experiments in which the decay of turbulence produced by a grid is observed for growing distances downstream the grid. Much has been learned in the

past from such real experiments where the appropriate Reynolds number is as low as 10 to 100. We will show that even more insight is gained from numerical experiments on such flow cases. More on the numerical models used for these low to moderate Reynolds number simulations will be said in § 2 and § 3.

1.3.2 High Reynolds Number Simulations

The simplest way to come around the resolution problem is simply to neglect those scales which cannot be resolved with our present computer capacities. In this case the energy dissipation is underestimated and such a simulation is likely to become unphysical, therefore, after some time. Nevertheless, at least for a certain time interval of the order L/U the large scale flow can be simulated properly by this means. Examples are the studies of Betchov (1975) on the structure of turbulence and of Schumann & Patterson (1978 b) of the energy exchange between velocity components for infinite Reynolds numbers.

Analysis of steady state turbulence, however, requires inclusion of at least a substitute for the dissipation process. Such a model has basically the same purpose as any closure model in the common statistical turbulence theories. However, simpler models are sufficient in the present context because

- the model has to account for the effect of the fine scale motion only, in contrast to statistical models which must be valid for all scales.
- the model does not have to be adjusted to the large scale geometry because the fine scale turbulence is much less dependent and of more universal nature than is the total turbulence.

These models are based mainly on the well known cascade process (Kolmogorov 1941):

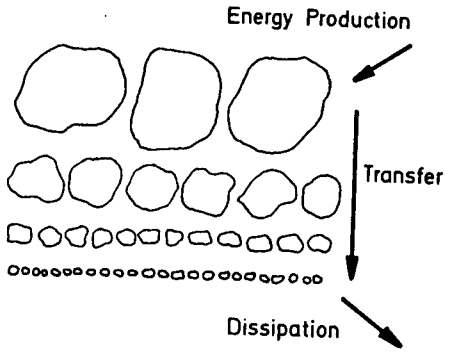

Fig. 1-1: The energy cascade according to the 1941 Kolmogorov theory. The figure indicates the generation of large eddies which break up into smaller and smaller ones and finally are dissipated.

For sufficiently large Reynolds numbers a turbulent flow is considered as to be a superposition of eddies of different scales. Only the largest of them are directly produced due to the instability of the mean flow. As indicated in Fig. 1-1 (from Rose & Sulem 1978), the motion of these large eddies is again unstable and results in smaller eddies which in turn feed even smaller ones. After many such "cascade-processes" the characteristic length scales, respectively the local Reynolds numbers are so small that the viscous forces become dominant and dissipate the kinetic energy of the motion. In any case, the length scales of these eddies are no longer related to the scales of the flow geometry. They are solely dependent on the viscosity and the amount of energy flux coming from the large scales and resulting in the dissipation ε. Therefore, from dimensional analysis according to Kolmogorov (1941), $\ell = \eta \equiv (\nu^3/\varepsilon)^{1/4}$ and the energy content at these length scales or its reciprocal, the wave-number k, varies as plotted in Fig. 1-2 like

$$E(k) = \alpha\, \varepsilon^{\frac{2}{3}}\, k^{-5/3} . \qquad (1\text{-}2)$$

Here, $E(k)$ is the so called three dimensional specific energy spectrum with $\int_0^\infty E(k)\,dk = \langle v^2 \rangle/2 \equiv E$. The parameter α is "Kolmogorov's constant" and well known from many experiments, see the recent summary by Champagne (1978):

$$\alpha = 1.6 \pm 0.06 \qquad (1\text{-}3)$$

This energy spectrum is valid in the "inertial subrange", that is for the wave-numbers k with $k_L \le k \le k_\ell$ where $k_L \ge 1/L$ and $k_\ell \le 1/\eta$.

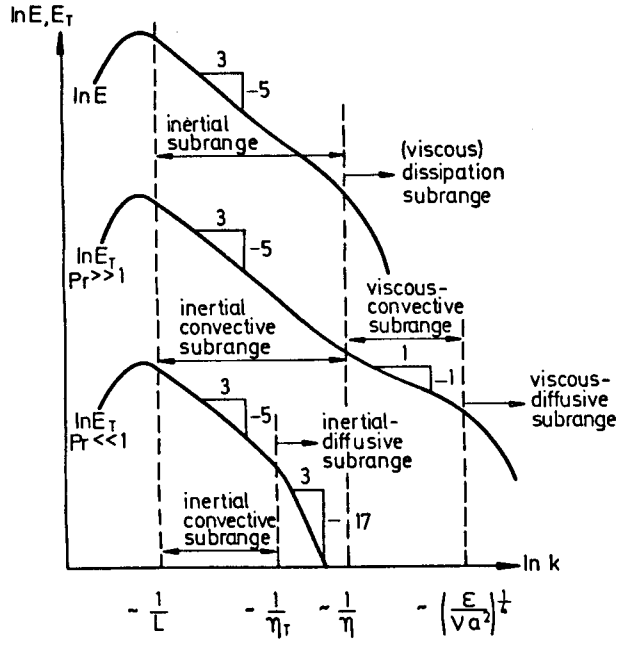

Fig. 1-2: Energy and temperature spectra, E and E_T respectively, versus wave-number k for different Prandtl numbers Pr.

One important consequence of this cascade pr ss is the "one-way" energy transfer from large to small scales. A second consequence of the cascade process is that any directional orientation which might exist at large scales (small wave-numbers) is lost at fine scales (large wave-numbers) so that we obtain a "locally isotropic" state of the turbulence for small scales (Hinze 1975). Therefore it is sufficient to use a simple model on the fine scale motion.

On the basis of these universal properties of turbulence it is possible to construct very simple SGS models. The only empirical input is Kolmogorov's constant α for momentum transport. For heat transport similar universal laws exist. These universal laws are valid, however, for extremely high Reynolds numbers only so that the validity of SGS models based on the inertial subrange is reduced at low Reynolds numbers.

This is true in particular near walls where the local Reynolds number decreases. Therefore, in the near wall region additional empirical information is required. The inertial subrange disappears at the border to the viscous sublayer and the fine scales are no longer isotropic regardless of how large the global Reynolds number becomes. Also, wall roughness and similar micro-effects become important in this part of the flow and there seems to be no chance to resolve such features in the foreseeable future. In the transition region between the viscous sublayer and the turbulent bulk flow a model of similar universality like Kolmogorov's inertial range is Prandtl's mixing layer model (see, e. g., Schlichting, 1965, p. 536). This model is known to produce surprisingly accurate results even for the large scale flow throughout boundary layers. In the viscous sublayer and for rough walls further empirical input is required (Grötzbach 1977a, 1978d). Details will be given in § 4.

Another way to overcome this problem at least partly (i. e. without accounting for roughness effects) would be to use variable resolution which focusses on the neighbourhood of the walls. Unfortunately this causes numerical problems due to stability

restrictions the integration schemes. In the common explicit calculations the time step must be kept below the minimum value of $\Delta x/u$ (Δx = grid spacing, u = local velocity) in the flow domain. Coordinate stretching, though attractive, does not avoid this difficulty. Some success in this direction has been achieved recently by Moin et al (1978). An alternative is the use of Chebyshev spectral schemes (Orszag 1971c) in which the local resolution is of order $1/N^2$ near the wall even when only N degrees of freedom are used. This aspect is discussed further in § 3.

1.4 The Basic Equations

Before we go into details, let us summarize the basic equations to be integrated. We start from the conservation laws for mass, momentum and scalar properties, e. g. temperature (or heat), in differential form for constant material properties.
Continuity equation:

$$div\ \underline{u} \equiv \partial u_j/\partial x_j = 0 \tag{1-4}$$

Navier-Stokes equations ($i = 1, 2, 3$):

$$\frac{Du_i}{Dt} \equiv \frac{\partial u_i}{\partial t} + \frac{\partial}{\partial x_j}(u_i u_j) = -\frac{1}{\varrho}\frac{\partial p}{\partial x_i} + \nu\frac{\partial^2 u_i}{\partial x_j^2} + F_i \tag{1-5}$$

Temperature equation:

$$\frac{\partial T}{\partial t} + \frac{\partial}{\partial x_i}(u_i T) = a\frac{\partial^2 T}{\partial x_i^2} + \dot{Q} \tag{1-6}$$

Here $\underline{u}=(u_1, u_2, u_3)$ = velocity vector, $\underline{x}$ = (x_1, x_2, x_3) = space vector, t = time, p = pressure, ϱ = density, ν = kinematic viscosity, $\underline{F}$ = force per unit mass, T = temperature, a = temperature conductivity, $\dot{Q}$ = heat source per unit mass divided by specific heat capacity. The summation convention applies. All quantities are taken as to be normalized by a suitable set of reference values. It might be noted that the convective terms are written in the so-called "conservative" form which has advantages with respect to the formulation of the discrete approximations because it allows for partial integration.

1.5 The Codes Used for the Present Studies

Efficient numerical solution algorithms are essential for direct numerical simulation of turbulence. Therefore in the following chapters much space is devoted to the description of the basic finite difference (§ 2) and spectral methods (§ 3). In fact, rigorous definition of the fine scale motion not resolved requires first to define the means used for resolution of the large scale part.

In § 2, a special FDM is described which has been implemented in a code "EDDY". This code integrates the Navier-Stokes equations for incompressible flow between two parallel plates, see Fig. 1-3 (Poiseuille or "channel" flow). This method is based on the same approximations as the code TURBIT-1 (Schumann 1973a), which in addition allows for an annular channel geometry in cylindrical coordinates and which employs SGS models. The successor TURBIT-2 (Grötzbach 1977a) includes temperature as an independent variable together with revised SGS models. The most recent version TURBIT-3 (Grötzbach 1979) is in addition suited for buoyancy driven flows.

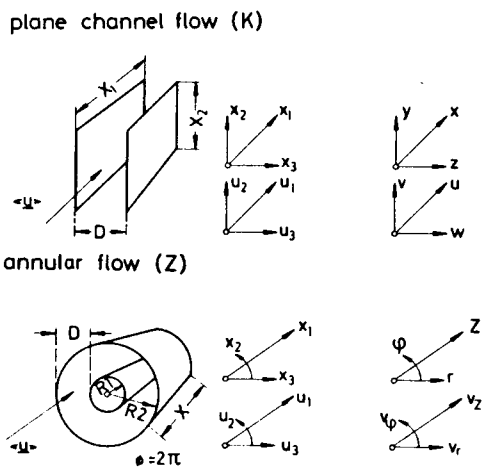

Fig. 1-3 Channel geometry

In § 3 the Fourier spectral code BOX of Orszag & Patterson (1972a, 1972b) is introduced which is applicable to a flow in a box with periodic boundary conditions in all three directions. Thereafter the basis of a Chebyshev-Fourier spectral method suitable for channel flow problems as proposed by Orszag (1971c) is explained. We are presently working on the development of a corresponding code (Kleiser & Schumann 1978).

In § 5 some results of applications of these codes will be presented for illustration purposes mainly.

2. A FINITE DIFFERENCE METHOD

2.1 The Averaged Basic Equations

We subsequently describe an averaging procedure which fulfills two purposes:

a) It brings the equations close to a finite difference formulation.

b) It helps to identify the sub-grid scale effects.

The procedure is that described in Schumann (1975 a). It differs in principle from the filtering philosophy proposed by Lilly (1967), unified by Leonard (1974), adopted by the Stanford group (Ferziger, 1977) and investigated by Love & Leslie (1977). We will explain the differences in § 4.5. Though the resultant finite difference scheme is fairly standard, the arguments used for its derivation are important for formulation of the SGS model and the boundary conditions.

In order to generate finite difference formulas from equations (1-4 to 1-6) we average them over small volumes as defined by our grid (see Fig. 2-1). Any quantity y averaged over such a volume V is denoted by $\overline{y}^{V}$.

$$\overline{y}^{V} \equiv \frac{1}{\Delta x_1 \, \Delta x_2 \, \Delta x_3} \int_{\Delta x_1} \int_{\Delta x_2} \int_{\Delta x_3} y(z_1, z_2, z_3) \, dz_3 \, dz_2 \, dz_1 \qquad (2\text{-}1)$$

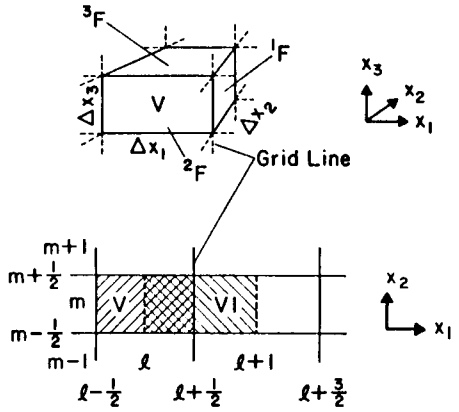

Fig. 2-1 Grid volumes and surfaces

Note that the volume over which the average is taken is fixed in space, so that $\overline{y}^{V}$ is defined only on discrete points. Then we integrate by parts using Gauss' theorem.

This results in a relationship between the time derivative of the physical quantity averaged over that volume and its transport across the surface of that volume in terms of surface averages. We denote the surface area of a grid volume, the normal of which is in the j-coordinate direction, by ^jF (presuperscripts are introduced for those indices for which the summation convention does not apply). The mean value of any quantity y averaged over ^jF is denoted by $\overline{y}^{j}$, e.g.:

$$\overline{y}^{1} \equiv \frac{1}{\Delta x_2 \, \Delta x_3} \int_{\Delta x_2} \int_{\Delta x_3} y(x_1, z_2, z_3) \, dz_3 \, dz_2 . \qquad (2\text{-}2)$$

Integration by parts gives us relationships of the form

$$\overline{\frac{\partial y}{\partial x_1}}^{V} = \frac{1}{\Delta x_1} \left\{ \overline{y}^{1}\left(x_1 + \frac{\Delta x_1}{2}\right) - \overline{y}^{1}\left(x_1 - \frac{\Delta x_1}{2}\right) \right\} \equiv \delta_1 \overline{y}^{1} \qquad (2\text{-}3)$$

Here, δ_j is the usual finite difference operator (Williams, 1969).

Applying these definitions to Eq. (1-4), the conservation law of mass, results in

$$\overline{\operatorname{div} \underline{u}}^{V} = \delta_j \overline{u_j}^{j} = 0 \qquad (2\text{-}4)$$

Now, let $\overline{u_j}^{j}$ be equal to the velocity component in the j-direction defined in a staggered grid system (see Fig. 2-2). Then we see that we do not need any approximation for this equation. This is the reason why staggered grids are used so often in hydrodynamics.

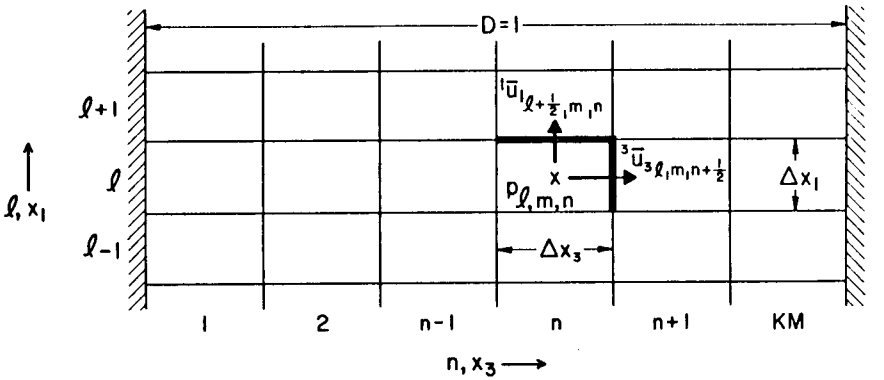

Fig. 2-2 Staggered grid. $\overline{u_i}^{i}$ fixed at the surfaces, p at the center of the mesh cells.

In order to get the averaged conservation law for the different velocity components, we average Eq. (1-5) over volumes Vi which are of the same size and form as the volume V, but shifted so as to surround the position of the velocity components within the staggered grid. Any quantity y averaged over such a volume is denoted by $\overline{y}^{Vi}$, where i corresponds to the coordinate direction in which the volume was shifted. Then we get

$$\overline{\frac{Du_i}{Dt}}^{Vi} = \overline{\frac{\partial u_i}{\partial t}}^{Vi} + \delta_j \left(\overline{u_j}^{j} \, \overline{u_i}^{i} \right) = -\delta_i \frac{\overline{p}^{i}}{\rho} + \delta_j \left(\nu \overline{\frac{\partial u_i}{\partial x_j}}^{j} - \overline{u_i' u_j'}^{j} \right) + \overline{F_i}^{Vi} . \qquad (2\text{-}5)$$

The terms

$$\overline{u_i' u_j'}^{j} \equiv \overline{(u_i - \overline{u_i}^{j})(u_j - \overline{u_j}^{j})}^{j} = \overline{u_i u_j}^{j} - \overline{u_i}^{j} \, \overline{u_j}^{j} \qquad (2\text{-}6)$$

are the SGS Reynolds stresses by which the effect of the fine-scale motion is identified. Here and below the summation convention refers to all lower subscripts on the right not enclosed in square brackets. Other indices of equal name take the corresponding values.

It should be noted that this analysis shows that the SGS stresses are essentially defined in terms of grid cell surface mean values rather than volume mean values; see also § 4.5. Moreover, these stresses would be non-zero even in laminar flows, but they are commonly assumed to be negligibly small there.

A similar average for the temperature equation, Eq. (1-6), gives

$$\frac{\overline{DT}^{V}}{Dt} = \frac{\partial}{\partial t}\overline{T}^{V} + \delta_i\left(\overline{u_i}^{i}\,\overline{T}^{i}\right) = \alpha\,\delta_i\left(\frac{\overline{\partial T}^{i}}{\partial x_i} - \overline{u_i' T'}^{i}\right) + \overline{\dot{Q}}^{V} \qquad (2\text{-}7)$$

where $\overline{u_i' T'}^{i}$ are the SGS heat fluxes.

So far no approximations have been involved. Indeed, the equations above are the conservation laws written in their integral form for grid volumes. We might have started from them right away.

2.2 Finite Difference Equations

Now, however, approximations are needed for several terms appearing in the averaged conservation equations. There are two types of unknown quantities: the SGS stresses $\overline{u_i' u_j'}^{j}$ and heat fluxes $\overline{u_i' T'}^{i}$ and those averaged quantities which must be known at positions not coinciding with the positions of the corresponding variables in the staggered grid. The latter unknown quantities can be evaluated by the usual difference formulas from the corresponding staggered grid values in their neighbourhood. A second-order energy-conserving scheme is used. The resultant finite difference equations are the same as those used by Deardorff (1970) for Cartesian and by Williams

(1969) for cylindrical coordinates, as far as the gross scale velocities are concerned. Therefore, volume balance and filter averaging procedures give the same result in this respect. The approximations used for the SGS stresses form the topics of § 4.

For the present discussion it is helpful to have the final finite difference equations at hand, i.e.

- conservation of mass (still exact):

$$\delta_j\,\overline{u_j}^{j} = 0 \qquad (2\text{-}8)$$

- momentum

$$\frac{\partial}{\partial t}\overline{u_i}^{i} + \delta_j\left(\overline{u_j}^{i}\,\overline{u_i}^{j}\right) = -\frac{1}{\rho}\,\delta_i\,\overline{p}^{V} + \delta_j\left\{\nu\,\delta_j\,\overline{u_i}^{i} - \overline{u_i' u_j'}^{j}\right\} + \overline{F_i}^{V} \qquad (2\text{-}9)$$

- temperature

$$\frac{\partial}{\partial t}\overline{T}^{V} + \delta_j\left(\overline{u_j}^{j}\,\overline{T}^{V}\right) = \delta_j\left\{\alpha\,\delta_j\,\overline{T}^{V} - \overline{u_j' T'}^{j}\right\} + \overline{\dot{Q}}^{V} \qquad (2\text{-}10)$$

Here $\overline{y}^{i}$ is the algebraic average of two values of y at two neighbouring positions separated by one grid interval in direction of the i-th coordinate.

2.3 Boundary Conditions

The purpose of this chapter is to illustrate how easily boundary conditions can be accounted for if one employs a staggered grid as proposed above.

The largest difficulties are usually raised by the common no-slip condition

$$\underline{u}\big|_W = 0 \qquad (2\text{-}11)$$

at walls. If x_3 is the normal component, then, at the wall itself, only the $\overline{u_3}^{3}$ value has to be specified in the finite difference scheme, whereas the $\overline{u_1}^{1}$ and $\overline{u_2}^{2}$ values are defined on grid cell surfaces which do not coincide with the wall. The boundary condition

$$ {}^3\bar{u}_3\big|_w = 0 \qquad (2\text{-}12) $$

can thus be taken into account without any further approximations for integration of this component.

In the equations for the remaining velocity components and the temperature at the wall not these quantities itself rather than their normal flux components are to be specified. So, in the convective terms

$$ \delta_j \left({}^j\bar{u}_i \, {}^j\bar{u}_j \right) = \delta_1 \left({}^1\bar{u}_1 \, {}^1\bar{u}_i \right) + \delta_2 \left({}^2\bar{u}_2 \, {}^2\bar{u}_i \right) + \delta_3 \left({}^3\bar{u}_3 \, {}^3\bar{u}_i \right), \; i = 1,2 \qquad (2\text{-}13) $$

only ${}^3\bar{u}_3 \, {}^3\bar{u}_i\big|_w$ has to be prescribed and it is clear from (2-11) that this convective flux is zero. Also, in the diffusive terms

$$ \delta_j \left({}^j\bar{\tau}_{i,j} \right) = \delta_1 \, {}^1\bar{\tau}_{i,1} + \delta_2 \, {}^2\bar{\tau}_{i,2} + \delta_3 \, {}^3\bar{\tau}_{i,3}, \; i = 1,2 \qquad (2\text{-}14) $$

with

$$ {}^j\bar{\tau}_{i,j} = {}^j\overline{u_i' u_j'} - \nu \, {}^j\overline{\partial u_i / \partial x_j}, \; i = 1,2 \qquad (2\text{-}15) $$

only ${}^3\bar{\tau}_{i,3}\big|_w$ has to be specified. The diffusive fluxes are not as simply approximated as the convective ones. Finite difference approximations are necessary because of the appearance of a derivative. Let us postpone discussion of the SGS flux until § 4.3. Then, an obvious approximation would be

$$ {}^3\bar{\tau}_{i,3}\big|_w \approx -\nu \frac{{}^i\bar{u}_i\big|_1}{\left(\frac{\Delta x_3}{2}\right)}, \qquad i = 1,2 \qquad (2\text{-}16) $$

where ${}^i\bar{u}_i\big|_1$ is the grid value in the middle of the first wall adjacent grid cell ($n=1$ in Fig. 2-2). Similarly for the temperature, the general basic boundary condition

$$ a_w T + b_w \, \partial T / \partial x_3 = c_w \qquad (2\text{-}17) $$

is used to give an approximation for ${}^3\bar{q} \equiv -a \, {}^3\overline{\partial T / \partial x_3}$ which is required solely in the diffusive term of the volume averaged temperature equation with the result

$$ {}^3\bar{q}\big|_w = -a \, \frac{2 \left(a_w \, {}^V\bar{T}\big|_1 - c_w \right)}{\Delta x_3 \, a_w - 2 \, b_w} \qquad (2\text{-}18) $$

These approximations suffice for laminar and low Peclet number turbulent flow because the profile is sufficiently linear near the walls.

The SGS fluxes are in fact zero at the walls because of zero fluctuating velocities u_3'. This is so in laminar and turbulent flow (at least if we assume a smooth wall). However, the underlying linearity assumption used in the finite difference approximations above is no longer appropriate for turbulent flows.

Therefore, for turbulent flow we use other boundary conditions as will be explained in § 4.3.

2.4 Time Integration

The time differencing scheme for the dominant convective terms should be of second order at least because first order schemes require numerical damping for stability as it appears if upwind differences are used (Roache 1976). In an explicit scheme, as we use it here, the diffusive terms must be treated by first order schemes, again for stability reasons. We do not recommend higher order approximations because of the increased storage requirements of such schemes. Following Deardorff (1970) a mixed procedure is employed in which an explicit first order "Euler" scheme is used with respect to diffusive terms whereas the second order "leapfrog" scheme is employed for the convective terms (Lilly 1965). The leapfrog scheme is bound to produce spurious $2\Delta t$-oscillations (Lilly 1965) which can be kept sufficiently small by means of an averaging step every, say, N_L time steps. Other researchers have used the Adams-Bashforth scheme (Lilly 1965, Deardorff 1973). We have not yet tried this alternative because the above procedure gives reasonable results. Some details of the combined Euler-Leapfrog scheme are explained below.

Let us abbreviate eqs. (2-9, 2-10) as

$$\frac{\partial u_i}{\partial t} = -\frac{1}{\rho}\delta_i p + C_i + D_i$$

$$\frac{\partial T}{\partial t} = C_T + D_T \qquad (2\text{-}19)$$

where $u_i \equiv \overset{i}{\overline{u_i}}$, $\delta_i p \equiv \delta_i \overset{v}{\overline{p}}$, $T \equiv \overset{v}{\overline{T}}$ and C_i, C_T are the convective and D_i, D_T the diffusive terms in the momentum and temperature equations, respectively. Then, at this stage, the pressure gradient is neglected and new velocities and temperatures are computed for the next time level $n+1$ (time steps Δt) from

$$\tilde{u}_i^{(n+1)} = f_1 u_i^{(n-k)} + f_2 u_i^{(n)} + f_3 \Delta t \left(C_i^{(n)} + D_i^{(n-k)}\right)$$

$$T^{(n+1)} = f_1 T^{(n-k)} + f_2 T^{(n)} + f_3 \Delta t \left(C_T^{(n)} + D_T^{(n-k)}\right) \qquad (2\text{-}20)$$

where

$$\begin{array}{llll} f_1 = 1\,, & f_2 = 0\,, & f_3 = 1\,, & k = 0 \quad \text{(Euler)} \quad \text{for } n = 0 \\ f_1 = 1\,, & f_2 = 0\,, & f_3 = 2\,, & k = 1 \quad \text{(leapfrog)} \quad n = 1, 2, \ldots, N_L - 1, N_L + 1, \ldots \\ f_1 = 1/2\,, & f_2 = 1/2\,, & f_3 = 3/2\,, & k = 1 \quad \text{(average)} \quad n = N_L, 2 \cdot N_L, \ldots \end{array} \qquad (2\text{-}21)$$

Here $\tilde{u}_i^{(n+1)}$ is a tentative result; it does not satisfy the continuity equation because of the neglected and as yet unknown pressure field.

A linear stability analysis (Schumann 1975 b) shows that this scheme is stable as long as

$$\Delta t \leq \frac{1}{2}\left[\sum_{i=1}^{3}\left(\frac{|u_i|}{\Delta x_i} + 4\,\frac{\max(\nu, a)}{\Delta x_i^2}\right)\right]^{-1} \qquad (2\text{-}22).$$

(If SGS models are used the viscosity ν or conductivity a has to be replaced by the effective total diffusivities.)

2.5 Computation of the Pressure

As stated before, the tentative velocity field does not satisfy the continuity equation. The correct new velocity field differs from the tentative one according to the pressure gradient:

$$u_i^{(n+1)} = \tilde{u}_i^{(n+1)} - f_3 \Delta t \frac{1}{\rho}\delta_i p^{(\tilde{n}+1)} \qquad (2\text{-}23)$$

The tilde above the time index n should express the fact that it is not strictly true to assign this pressure to the actual time level rather than to some intermediate level. The new velocity has to satisfy the continuity equation in its discretized form (2-8).

Therefore, the pressure has to satisfy the discretized "Poisson" equation

$$\frac{1}{\rho}\delta_i \delta_i p^{(\tilde{n}+1)} = \delta_i \tilde{u}_i^{(n+1)} / (f_3 \Delta t). \qquad (2\text{-}24)$$

At the walls, we do not integrate the normal velocity according to the momentum equation rather than set $u_3^{(n+1)}|_W = \tilde{u}_3^{(n+1)}|_W = 0$ according to the boundary condition (2-12). Therefore, from (2-23), we get the Neumann-type boundary condition

$$\delta_3 p|_W = 0. \qquad (2\text{-}25)$$

These arguments are essentially those of Amsden & Harlow (1970).

The resultant set of algebraic equations for the pressure values in each grid cell is solved very efficiently by means of fast Fourier transforms in the x_1 and x_2 directions and Gaussian elimination on the remaining sets of tridiagonal systems (Schumann 1973 a). For many other geometries similar fast elliptic solvers are available (Schumann 1978, 1979). Typical solution times are 5 s on an IBM 370/168 for a 64x32x32 grid.

We stress that

a) the pressure is computed from a set of finite difference equations (2-24, 2-25) which appear as an immediate consequence of the discrete form of the divergence and gradient operators; it would be inconsistent to use a higher order finite difference scheme for the pressure part alone.

b) the resultant velocity field, eq. (2-23), satisfies the continuity equation (2-8) exactly (except for round-off errors) and independently of the departure from continuity in the previous or initial time level velocities; so the accumulation of divergence errors is avoided.

If a non-staggered (normal) grid would have been used, then the divergence and gradient operators would include differences taken over two grid intervals so that the resultant consistent pressure equations would be of the form (written for a one-dimensional grid)

$$\frac{1}{8}\,\frac{1}{4\Delta x^2}\left(p_{i-2} - 2p_i + p_{i+2}\right) = \frac{1}{2\Delta x}\left(\tilde{u}_{i+1} - \tilde{u}_{i-1}\right)/(f_3\,\Delta t)$$

i.e., the pressure values at two adjacent grid values are decoupled (except for boundary conditions). This clearly results in $2\Delta x$ pressure oscillations as they have, in fact, been found on such non-staggered grids (Hodge 1975). This is an additional argument pro staggered and contra the classical non-staggered grid.

2.6 The Code EDDY

The above finite difference scheme, neglecting all SGS terms, has been implemented in a FORTRAN-IV code "EDDY".

An essential feature of this code is a dynamic data management (Schumann 1974) which is important for computers which do not provide a virtual memory. For this purpose the data of all three-dimensional fields (i.e. each velocity component and the

temperature three subsequent time levels as a function of the three coordinates) are splitted into blocks of two-dimensional fields each containing the data belonging to one grid plane parallel to the walls. Only those blocks actually required are kept in core storage while the others are free to be swapped on external direct access storage when the available core storage is exceeded. This technique is used also in the TURBIT-codes and has been found to be valuable with respect to job priorities even on machines with virtual memory systems (Grötzbach, 1977a, p. 74). The onliest field which is not subdivided into blocks in this way is the pressure field. During the solution process for the discretized Poisson equation the data are processed by lines alternating in all three space directions. Therefore block partitioning of the pressure data seemed not to be advisable. Recently Burridge & Temperton (1977) have described an algorithm for fast solution of the Poisson equation which would allow for partioning of the pressure data also but we have not yet applied this proposal.

Another important feature of the code EDDY (and TURBIT) is an extensive plotting package including contour line and vector plots. The code EDDY also contains a package of subroutines for tracing marker particles (as used by Peskin 1974) which are initially defined at some positions and then moved according to the velocity field in a Lagrangian manner (Dütting 1976).

For example, Fig. 2-3 shows a typical result. In this case the flow field started from an initial velocity composed of a mean Poiseuille flow profile, four vortices with axis in the axial (x_1) direction and eight vortices with axis in the normal (x_3) direction. Markers are specified initially at equidistantly spaced points. Then the flow is integrated over a certain time interval and plotted each time step perspectively. In this manner streak lines are produced which give insight in the flow dynamics. A movie generated from such plots would be even more instructive.

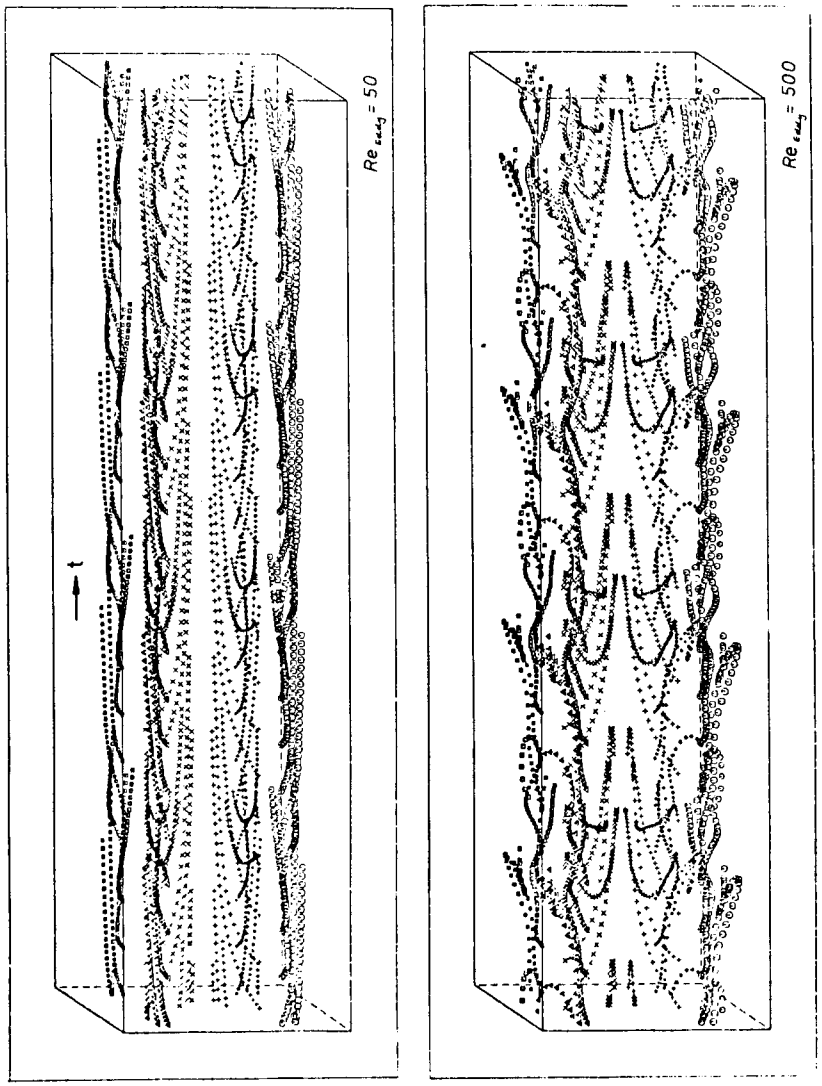

Fig. 2-3 Marker trajectories, i.e. plots of the position of several markers at a sequence of time steps,for two Reynolds numbers

Using EDDY, ..e influence of the three-dimensionality of the flow field has been investigated (Grötzbach et al. 1975) with the result that the turbulent Prandtl number, i.e. the ratio of effective diffusivities for momentum and heat is equal to one if the vortex field is two-dimensional but different from one if the flow is three-dimensional.

The code EDDY might be attractive for many further applications.

3. SPECTRAL METHODS

In this chapter the fundamentals of the spectral method (SM) are explained. In § 3.1 a definition of the SM is given and general properties are discussed. The underlying approximation principles are explained. In § 3.2 application of the SM in terms of Fourier series expansions to the "box problem" appropriate to homogeneous turbulence is described. The § 3.3 contains a description of the Chebyshev SM which is very attractive for channel flow problems but still in a developing stage.

3.1 Overview

Spectral methods have a long history (Orszag & Israeli, 1973). They are standard mathematical techniques for solution of differential equations. Most of the work in the past has been concerned with obtaining analytical solutions. The older methods have been relatively inefficient in practical use when applied to nonlinear problems. The efficient use of the SM for numerical simulations is a relatively new field. An amirable amount of fundamental ideas has been introduced by Orszag and coworkers. See the references; in particular we refer to the recent monograph of Gottlieb & Orszag (1977). In the subsequent text we will generally not cite the original papers except for references to additional informations.

3.1.1 General Properties

An alternative to the use of finite difference equations is to expand the dependent variables as a function of all or some of the independent variables in a finite series of specified ansatz functions. The resulting trial solution contains adjustable coefficients which are determined "as good as possible" using a suitable criterion. Such a criterion might be taken from the "method of weighted residuals" (e.g. the Galerkin method) or from a variational principle. In contrary to finite differences, derivatives are specified by the derivatives of the trial functions without further approximations. If the ansatz functions are only piecewise continous and nonvanishing on certain elements of the domain, we have the finite element method.

In the spect method ansatz functions are used which are infinitely differentiable on the whole domain, like polynomials or trigonometric functions. Also, they should form a complete set for the space of functions considered. If possible, the ansatz functions are taken from a set of orthogonal functions (e.g. Chebyshev polynomials). Trigonometric functions are suited for periodic solutions. For both the trigonometric and Chebyshev functions fast transform methods (using FFT) exist which allow for efficient computations.

The main advantages of the spectral methods are their high convergence order for cases where the solutions are sufficiently often differentiable and have (in case of Fourier functions) the appropriate periodicity properties. If N is the number of degrees of freedom (number of adjustable coefficients in the trial function of the spectral method or number of grid points in the finite difference scheme) then the maximum error of the finite difference approximation decreases like N^{-2} or N^{-4} (method of second order or fourth order). In the spectral method, however, it decreases faster than any power of $1/N$ for large values of N. Boundary conditions require difference approximations in a finite difference scheme whereas they can be satisfied exactly in the spectral method if suitable ansatz functions are used. Because of the higher accuracy of the SM one gets the same accuracy as with finite differences for fewer degrees of freedom. Or, at the same computational work, one can treat a given flow problem for higher Reynolds numbers.

Another main advantage of the SM is the enlarged understanding of the physical behaviour which can be gained because of the dual representation of the solution. The solution can be interpreted in terms of its variation in "real" space as well as in terms of the relative contributions of the different ansatz functions ("spectral" or "wave number" space). This is especially true with respect to simulations of homogeneous turbulence where Fourier functions arise naturally in both theoretical analysis and numerics.

One disadvantage of the SM is its restriction to simple geometries. Also, the construction and programming of an efficient algorithm for solution of a flow problem is much more complicated in the SM than using finite differences. The efficiency of the SM is reduced if more and more nonlinearities are to be taken into account. Because of the global nature of the trial functions of the SM in contrast to the local approximations of the finite differences and finite elements the SM tends to result in (linear) systems of equations with a fully populated coefficient matrix. These might be ill conditioned numerically such that a small error (either logical or numerical) has drastic effects. The numerical conditioning can be improved and the computational work reduced by suitable transformations accounting for the orthogonality of the ansatz functions. In case of Fourier ansatz functions it is possible to transform to a pure diagonal matrix so that inversion of linear systems becomes trivial. With Chebyshev ansatz functions banded matrices or close approximations to these appear which are similar in structure to those of finite difference schemes. The sensitivity to logical errors is certainly an advantage of the SM because it makes the results more reliable. The global instead of local approximation type becomes, however, a disadvantage when the number of free parameters in the trial function is too small to approximate local physical effects. In fact, the errors of the SM can be considerably larger than those of the finite difference scheme if insufficient resolution is being used.

Most of the applications of the spectral method in turbulence simulations have considered either isotropic or at least homogeneous turbulence. We will start in the following § 3.2 with explaining the particular SM ("BOX") developed by Orszag & Patterson for this purpose. The extension to channel or boundary layer flows is considerably more difficult as will be explained in § 3.3. Before, it is worthwhile to recapitulate the basic concepts which are used to determine the adjustable coefficients in the trial functions.

3.1.2 Approximatic Principles

3.1.2.1 General problem formulation

We look for the solution u on a spatial domain $\mathcal{B}$ ($x \in \mathcal{B}$) at times $t \geq 0$ to the differential equation

$$\mathcal{G}u \equiv \mathcal{D}u - \frac{\partial u}{\partial t} = 0 \qquad x \in \mathcal{B},\ t \geq 0 \tag{3-1}$$

with (linear) boundary conditions on the boundary $\partial\mathcal{B}$

$$\mathcal{R}u(x,t) = f_{\mathcal{R}}(x,t) \qquad x \in \partial\mathcal{B},\ t \geq 0 \tag{3-2}$$

and initial values f_0:

$$u(x,0) = f_0(x) \qquad x \in \mathcal{B}. \tag{3-3}$$

A (linear) trial solution is taken in the form

$$w(x,t) = \bar{w}(x,t) + \sum_{k=0}^{N} \hat{u}_k(t)\, w_k(x) \tag{3-4}$$

with specified functions $\bar{w}(x,t)$, $w_k(x)$ but adjustable time functions $\hat{u}_k(t)$. The function $\bar{w}$ satisfies the inhomogeneous and w_k the homogeneous boundary conditions

$$\begin{aligned} \mathcal{R}\,\bar{w}(x,t) &= f_{\mathcal{R}}(x,t) \\ \mathcal{R}\,w_k(x) &= 0 \qquad , k = 0,\dots,N \end{aligned} \qquad x \in \partial\mathcal{B},\ t \geq 0. \tag{3-5}$$

Then the trial function (3-4) satisfies the boundary conditions for all choices of the time functions $\hat{u}_k(t)$. The time functions can be determined from either a variational principle, if available (which is not the case for the Navier Stokes equation, see Finlayson, 1972, § 8.6), by the method of weighted residuals ("MWR") (Finlayson, 1972, part I), or by the so called tau method (Fox & Parker, 1968). The latter two principles are explained subsequently.

3.1.2.2 The method of weighted residuals (MWR)

In the MWR the trial function (3-4) is substituted into the differential equation (3-1) and one requires that the integral over the residual $\mathcal{G}w$, weighted by some prescribed functions g_j, is zero:

$$(\mathcal{G}w, g_j) = 0 \Leftrightarrow \left(\frac{\partial w}{\partial t}, g_j\right) = (\mathcal{D}w, g_j), \; j = 0, \ldots, N. \qquad (3\text{-}6)$$

The "inner product" (u, w) is defined by

$$(u, w) = \int_{\mathcal{B}} u(x)\, w^*(x)\, P(x)\, dx \qquad (3\text{-}7)$$

If $(u, w) = 0$ the functions u and w are said to be orthogonal. $P(x) > 0$ is a weighting function which is taken to emphasize the important regions of the domain and possibly specified such that the functions w_k form an orthogonal set. In addition one requires orthogonality for the initial values

$$\left(w(x,0) - f_0(x), \; g_j\right) = 0, \; j = 0, \cdots, N. \qquad (3\text{-}8)$$

Several well known methods appear if suitable weighting functions g_j are specified. Some are:

1. The least squares method

   $$(\mathcal{G}w, \mathcal{G}w) = \min_{\hat{u}_k}$$

   gives (3-6) with $g_j = \partial(\mathcal{G}w)/\partial\hat{u}_j$

2. In the Galerkin method $g_j = w_j$.

3. The collocation method, usually identified by

   $$\mathcal{G}w(x_j) = 0, \; j = 0, \cdots, N$$

   using selected points x_j, appears if $P(x) = 1$ and the weighting functions are chosen to be the displaced Dirac delta functions $g_j = \delta(x - x_j)$. These have the property

$$\int_{\mathcal{B}} g_j \, dx = u_j = u(x_j).$$

From these principles one obtains in case of $\bar{w} = 0$ (homogeneous boundary conditions) and for a linear operator $\mathcal{D}u \equiv Lu - r$

method	g_j	equations $(j = 0, \ldots, N)$	
1. least squares	Lw_j	$\sum_{k=0}^{N} \frac{d}{dt}\hat{u}_k (w_k, Lw_j) = \sum_{k=0}^{N} \hat{u}_k (Lw_k, Lw_j) - (r, Lw_j)$	(3-9a)
2. Galerkin	w_j	$\sum_{k=0}^{N} \frac{d}{dt}\hat{u}_k (w_k, w_j) = \sum_{k=0}^{N} \hat{u}_k (Lw_k, w_j) - (r, w_j)$	(3-9b)
3. collocation	$\delta(x-x_j)$	$\sum_{k=0}^{N} \frac{d}{dt}\hat{u}_k w_k(x_j) = \sum_{k=0}^{N} \hat{u}_k Lw_k(x_j) - r(x_j)$	(3-9c)

i.e. a linear system of ordinary differential equations for $\hat{u}_k$ and in the steady case a system of algebraic equations. Time integration is done by conventional time differencing using low order (typically second order) methods like those discussed by Lilly (1965). Orszag identifies the Galerkin method using smooth global ansatz functions with the spectral method and the collocation method for the same type of ansatz functions with the "pseudo-spectral method". The main difference appears with respect to the approximation of nonlinear terms in the differential equation. In the pseudo-spectral method so called "aliasing" contributions appear as will be explained by reference to Fourier ansatz functions in § 3.2.4.

3.1.2.3 The tau-method

In the tau-method the trial function w is introduced in the differential equation $\mathcal{G}u = 0$ for the unknown solution u. The resulting expression is expanded in terms of the w_k. By comparing the coefficients one obtains usually a certain number r more equations than unknowns $\hat{u}_k$. This set would be unsolvable because the problem in general has no exact solution in terms of the w_k $(k = 0, \ldots, N)$. Therefore, r of these equations are

dropped or, what is the same, are disturbed by adding (unknown) error terms $\tau_i(x,t)$ (therefore the name) so that they are consistent with the $N+1$ other equations. That means, a disturbed problem is solved exactly by the trial function w. Often, the knowledge of the τ-functions can be used for error estimations (Fox & Parker, 1968).

3.1.3 General Remarks on the Accuracy

Neglecting time differencing errors, we have to distinguish between the approximation errors which appear for very large numbers N of ansatz functions (ultimate convergence order) and those for moderate values of N. It will be seen (§ 3.2.5) that the errors decrease faster than any power of $1/N$ if the velocity field is infinitely differentiable and the ansatz functions are chosen properly. However, this range of "infinite order accuracy" (Orszag & Israeli, 1974) is reached only if N is sufficiently large, say larger than N_{min}. The value of N_{min} depends on the smallest important scales of the flow like the thickness of boundary layers or the size of eddies with maximum dissipation. In this respect, the SM is only marginally superior to finite difference approximations. See also further discussions in § 3.2.5 and § 3.3.3.5.

3.2 The Box-Problem

The spectral method was spectacularily successful in turbulent flow simulations first for homogeneous turbulence in which the velocity field (and the pressure etc.) may be approximated by a finite Fourier series. Subsequently, we will describe the numerical method developed by Orszag and Patterson (1972a, 1972b) which is implemented in the code BOX (Patterson 1971, Riley & Patterson 1974). For illustration, typical flow fields are shown in Fig. 3-1 and 3-2 (from Schumann & Patterson 1978a).

Similar codes have been discussed and developed by Sicilian & Leonard (1974), Fornberg (1975), Salu & Knorr (1975), Schamel & Elsässer (1976). The effect of a constant strain is included

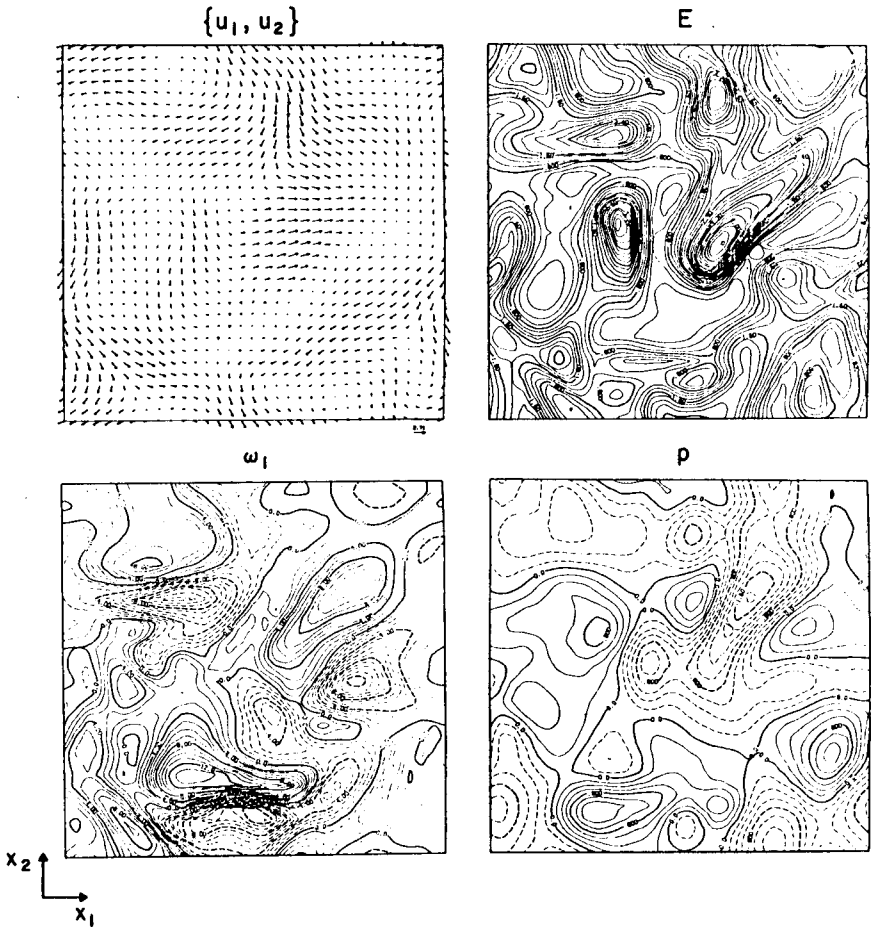

Fig. 3-1 Velocities $\{u_1, u_2\}$, kinetic energy E, vorticity ω_1 and pressure p for isotropic turbulence with $Re_\lambda \approx 30$ obtained from the Fourier spectral-method.

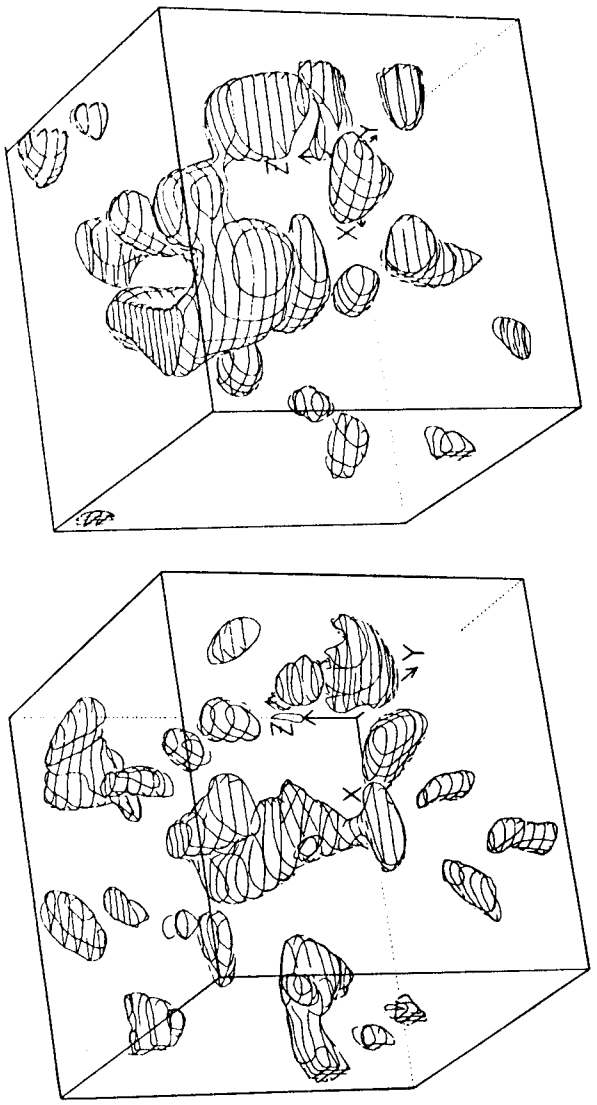

Fig. 3-2 Isosurfaces of kinetic energy E and pressure p in real space $\{x_1, x_2, x_3\} = \{X, Y, Z\}$ for isotropic turbulence at $Re_\lambda = 30$. Inside the "clouds" the kinetic energy is larger than a mean value, whereas the pressure is smaller than a mean value. One observes a small correlation between these quantities.

in the code Rogallo (1978). Magnetohydrodynamics has been included by Schumann (1976) and Pouquet & Patterson (1978). We will explain first the pseudo-spectral approach using a rectangular equidistant grid as collocation points with N^3 grid points. The actual code uses the Galerkin method with $N = 32$.

3.2.1 The Fourier Transform

Let us assume that the energy associated with flow scales greater than the side length L_{box} of a cubic box is negligible. Then, we may assume that the flow is periodic in all three coordinate directions $\underline{e}_i$ so that the velocity vector $\underline{u} = (u_1, u_2, u_3)$ and similarly other flow quantities satisfy

$$\underline{u}(\underline{x}, t) = \underline{u}(\underline{x} + L_{box}\,\underline{e}_i, t), \quad i = 1,2,3 . \tag{3-10}$$

Then, the velocity field may be expanded in a Fourier series

$$\underline{u}(x,t) = \sum_{all\ \underline{k}} \sum\sum \hat{\underline{u}}_{\underline{k}}(t)\, exp(i\,\underline{k}\cdot\underline{x}) \tag{3-11}$$

where $i = \sqrt{-1}$, $\underline{k} = (2\pi/L_{box})\underline{n}$ is the "wave number" vector, $\underline{n} = (n_1, n_2, n_3)$, and the n_i are integers with $-\infty < n_i < \infty$. Because of the orthogonality of the Fourier functions, the "modal amplitudes" $\hat{\underline{u}}_{\underline{k}}(t)$ are given by

$$\hat{\underline{u}}_{\underline{k}}(t) = \frac{1}{L_{box}^3} \iiint_0^{L_{box}} \underline{u}(\underline{x}, t)\, exp(-i\,\underline{k}\cdot\underline{x})\, d\underline{x} . \tag{3-12}$$

For a numerical calculation, $\underline{n}$ must be restricted to a finite set of numbers, say

$$-\frac{N}{2} \le n_i < \frac{N}{2}, \qquad -\left(\frac{2\pi}{L_{box}}\right)\frac{N}{2} \le k_i < \left(\frac{2\pi}{L_{box}}\right)\frac{N}{2}, \quad i = 1,2,3 \tag{3-13}$$

which we notate as $\|\underline{n}\| < \frac{N}{2} \equiv K$ or $\|\underline{k}\| < k_{max} \equiv (2\pi/L_{box})K$. So, our trial function is

$$\underline{w}(\underline{x}, t) = \sum_{\|\underline{k}\| < k_{max}} \sum\sum \hat{\underline{u}}_{\underline{k}}(t)\, e^{i\,\underline{k}\cdot\underline{x}} \tag{3-14}$$

Let us define

$$\underline{x}_{\underline{j}} = \frac{L_{box}}{N}\left(j_1, j_2, j_3\right), \quad \|\underline{j}\| < \frac{N}{2} \tag{3-15}$$

as being the collocation points. Let

$$\underline{u}_{\underline{j}}(t) \equiv \underline{u}(\underline{x}_{\underline{j}}, t) \tag{3-16}$$

be the values of the trial solution at these collocation points. Then the coefficients or modal amplitudes $\hat{\underline{u}}_{\underline{k}}(t)$ in the trial function

$$\underline{u}_{\underline{j}}(t) = \sum\sum\sum_{\|\underline{k}\| < k_{max}} \hat{\underline{u}}_{\underline{k}}(t)\, exp\left(i\, \underline{k}\cdot\underline{x}_{\underline{j}}\right) \tag{3-17}$$

are related to $\underline{u}_{\underline{j}}(t)$ by

$$\hat{\underline{u}}_{\underline{k}}(t) = \frac{1}{N^3} \sum\sum\sum_{\|\underline{j}\| < K} \underline{u}_{\underline{j}}(t)\, exp\left(-i\, \underline{k}\cdot\underline{x}_{\underline{j}}\right) \tag{3-18}$$

due to orthogonality of the finite discrete Fourier series. Eqs. (3-17, 18) define the finite discrete Fourier transform pair

$$\hat{\underline{u}}_{\underline{k}} \longleftrightarrow \underline{u}_{\underline{j}}. \tag{3-19}$$

As a consequence of truncation the $\hat{\underline{u}}_{\underline{k}}$ outside the discrete interval $\|\underline{k}\| < k_{max}$ are misrepresented by eq. (3-18) as being periodic. This "aliasing" or "Umklapp" effect gives erroneous contributions in the non-linear terms (see § 3.2.4). Note that, because of $\underline{u}_{\underline{j}}$ being real valued, $\hat{\underline{u}}_{\underline{k}}$ is complex but conjugate symmetric, $\hat{\underline{u}}_{\underline{k}} = \hat{\underline{u}}^{*}_{-\underline{k}}$. One can take advantage of this fact in the transform algorithm (Cooley et al., 1970).

3.2.2 The Tranformed Navier-Stokes Equations

For the present purpose it is convenient to write the Navier-Stokes equations and continuity equation in vector form:

$$\frac{\partial}{\partial t}\underline{u} + (\underline{u}\cdot\underline{\nabla})\underline{u} = -\underline{\nabla}(p/\rho) + \nu\nabla^2\underline{u} \tag{3-20}$$

$$\underline{\nabla}\cdot\underline{u} = 0 \tag{3-21}$$

As will be explained later it is advantageous to use the vector identity

$$(\underline{u}\cdot\underline{\nabla})\underline{u} = -\underline{u}\times\underline{\omega} + \underline{\nabla}E \tag{3-22}$$

$$\underline{\omega} \equiv \underline{\nabla}\times\underline{u}, \quad E \equiv \tfrac{1}{2}\underline{u}\cdot\underline{u}$$

for rewriting eq. (3-20) as

$$\frac{\partial}{\partial t}\underline{u} = -\underline{\nabla}\left(p/\rho + E\right) + \underline{s} + \nu\nabla^2\underline{u} \tag{3-23}$$

$$\underline{s} \equiv \underline{u}\times\underline{\omega}.$$

Now, we insert the trial function (3-14) noting

$$\underline{\nabla}\cdot\underline{w} = \sum\sum\sum_{\|\underline{k}\| < k_{max}} i\,\underline{k}\cdot\underline{u}_{\underline{k}}\, exp\left(i\,\underline{k}\cdot\underline{x}\right)$$

$$\underline{\nabla}\times\underline{w} = \sum\sum\sum_{\|\underline{k}\| < k_{max}} i\,\underline{k}\times\underline{u}_{\underline{k}}\, exp\left(i\,\underline{k}\cdot\underline{x}\right). \tag{3-24}$$

The resulting set of equations written for each collocation point $\underline{x}_{\underline{j}}$ can be Fourier transformed to give

$$\frac{d}{dt}\hat{\underline{u}}_{\underline{k}} = -i\,\underline{k}\left(\tfrac{1}{\rho}\hat{p}_{\underline{k}} + \hat{E}_{\underline{k}}\right) + \hat{s}_{\underline{k}} - \nu k^2\hat{\underline{u}}_{\underline{k}} \tag{3-25}$$

$$i\,\underline{k}\cdot\underline{u}_{\underline{k}} = 0 \tag{3-26}$$

in which $k^2 = \underline{k}\cdot\underline{k}$ and the Fourier pairs

$$\hat{\underline{u}}_{\underline{k}} \leftrightarrow \underline{u}_{\underline{j}}, \quad \hat{p}_{\underline{k}} \leftrightarrow p_{\underline{j}}, \quad \hat{E}_{\underline{k}} \leftrightarrow E_{\underline{j}}, \quad \hat{s}_{\underline{k}} \leftrightarrow s_{\underline{j}}$$

appear.

It is a consequence of the orthogonality a the simple form (3-24) by which derivatives can be computed that the resulting set of equations forms a diagonalized system of equations at least with respect to the linear terms. This property is unique to the Fourier spectral method.

From eq. (3-25) one can eliminate the pressure head $\hat{p}/\rho + \hat{E}$ by twice cross-multiplying with $\underline{k}$, using the identity $\underline{k}\times(\underline{k}\times\hat{\underline{u}}) = \underline{k}(\underline{k}\cdot\hat{\underline{u}}) - \hat{\underline{u}}(\underline{k}\cdot\underline{k})$, where the first summand is zero because of eq. (3-26), and dividing by k^2:

$$\frac{d}{dt}\,\hat{\underline{u}}_{\underline{k}} = -\frac{1}{k^2}\,\underline{k}\times(\underline{k}\times\hat{\underline{s}}_{\underline{k}}) - \nu k^2\,\hat{\underline{u}}_{\underline{k}} \quad . \tag{3-27}$$

The pressure is obtained from eq. (3-26) and (3-25):

$$\hat{p}_{\underline{k}} = -\frac{1}{k^2}\,i\,\underline{k}\cdot\hat{\underline{s}}_{\underline{k}} - \hat{E}_{\underline{k}} \tag{3-28}$$

Eq. (3-27) could be used to integrate the modal amplitudes in time. For divergence free initial values, the resultant velocity field should satisfy the continuity equation because the forcing term does not produce any divergence. However, one can enforce continuity and reduce the storage requirements at the same time, by using a mapping to a divergence free space. In fact, because of continuity only two of the three components $\hat{\underline{u}}_{\underline{k}}$ for each $\underline{k}$ can be specified independently. Therefore, $\hat{\underline{u}}_{\underline{k}}$ is expressible in terms of two parameters $u^a_{\underline{k}}$ and $u^b_{\underline{k}}$:

$$\hat{\underline{u}}_{\underline{k}} = u^a_{\underline{k}}\,\underline{a}(\underline{k}) + u^b_{\underline{k}}\,\underline{b}(\underline{k}) \tag{3-29}$$

where $\underline{a}$ and $\underline{b}$ are vectors which are orthogonal to each other and to the wave number vector $\underline{k}$ so that $\underline{k}\cdot\hat{\underline{u}}_{\underline{k}} = 0$:

$$\underline{a}(\underline{k}) = k_0\,(\underline{k}\times\underline{c}), \quad \underline{b} = \underline{k}\times(\underline{k}\times\underline{c}) \tag{3-30}$$

The vector $\underline{c}$ must be specified such that it is not parallel to any wave-number vector $\underline{k}$ appearing in the computations. One possibility would be $\underline{c} = (N/2+1, N/2+2, N/2+3)$. The factor k_0 is introduced so that $\underline{a}$ and $\underline{b}$ have the same order of magnitude. Obviously,

$$u^a_{\underline{k}} = \frac{1}{a^2}\,\underline{a}\cdot\underline{u}_{\underline{k}}, \quad u^b_{\underline{k}} = \frac{1}{b^2}\,\underline{b}\cdot\underline{u}_{\underline{k}}, \tag{3-31}$$

so that instead of eq. (3-27), one has to integrate

$$\frac{d}{dt}\,u^a_{\underline{k}} = -\frac{1}{a^2}\,\frac{\underline{a}\cdot[\underline{k}\times(\underline{k}\times\hat{\underline{s}}_{\underline{k}})]}{k^2} - \nu k^2 u^a_{\underline{k}} \tag{3-32}$$

$$\frac{d}{dt}\,u^b_{\underline{k}} = -\frac{1}{b^2}\,\frac{\underline{b}\cdot[\underline{k}\times(\underline{k}\times\hat{\underline{s}}_{\underline{k}})]}{k^2} - \nu k^2 u^b_{\underline{k}} \quad . \tag{3-33}$$

This can be done, e.g., by using the second order accurate leapfrog scheme on the non-linear terms together with Crank-Nicholson on the viscous terms (Lilly 1965). In order to get the integration started, an Euler-step is used, which is also used every, say, N_L-th step $(N_L \approx N)$ to smooth out the possible zig-zag instability of the leapfrog scheme. No rigorous stability analysis exists for this scheme but experience indicates stability for a time step $\Delta t \lesssim (L_{box}/N)/|\underline{u}|_{max}$.

3.2.3 Treatment of Nonlinearities

It remains to discuss how the non-linear terms $\underline{s} = \underline{u}\times\underline{\omega}$ and $E = \frac{1}{2}\,\underline{u}\cdot\underline{u}$ and their Fourier transforms $\hat{\underline{s}}_{\underline{k}}$, $\hat{E}_{\underline{k}}$ are evaluated. Let us discuss this problem for the case of a scalar non-linear term

$$h(\underline{x}) = f(\underline{x})\,g(\underline{x})$$

or

$$h_{\underline{j}} = f_{\underline{j}}\,g_{\underline{j}} \tag{3-34}$$

with $h_{\underline{j}} = h(\underline{x}_{\underline{j}})$, e.g..

Let

$$\hat{f}_{\underline{k}} \leftrightarrow f_{\underline{m}}, \quad \hat{g}_{\underline{k}} \leftrightarrow g_{\underline{m}}, \quad \hat{h}_{\underline{k}} \leftrightarrow h_{\underline{m}}$$

then

$$h_{\underline{j}} = \Big(\sum_{\underline{m}} \hat{f}_{\underline{m}} \, e^{i \underline{m} \cdot \underline{x}_{\underline{j}}} \Big) \Big(\sum_{\underline{n}} \hat{g}_{\underline{n}} \, e^{i \underline{n} \cdot \underline{x}_{\underline{j}}} \Big)$$

$$= \sum_{\underline{m}} \sum_{\underline{n}} \hat{f}_{\underline{m}} \, \hat{g}_{\underline{n}} \, e^{i (\underline{m}+\underline{n}) \cdot \underline{x}_{\underline{j}}} . \qquad (3\text{-}35)$$

Obviously, the non-linear terms result in contributions at wave numbers $\underline{m}+\underline{n}$, some of which lie outside the interval $\|\underline{k}\| < k_{max}$. Due to periodicity these contributions are not neglected (as they should be) rather than misrepresented by terms inside the interval. Elimination of these aliasing contributions is possible as described in § 3.2.4. In the pseudo-spectral scheme the discrete finite Fourier transform results in

$$\hat{h}_{\underline{k}} = \sum_{\underline{m}} \hat{f}_{\underline{k}-\underline{m}} \, \hat{g}_{\underline{m}} = \sum_{\underline{m}} \hat{f}_{\underline{m}} \, g_{\underline{k}-\underline{m}} . \qquad (3\text{-}36)$$

So, in order to compute the nonlinear terms a convolution sum has to be evaluated. This would require N^d multiplications per mode $\hat{h}_{\underline{k}}$, of which there are N^d many, if d is the number of dimensions. So, a total of N^{2d} multiplications appears. In three dimensional space, the operation count N^6 would make the present scheme useless for practical purposes.

This efficiency problem can be surrounded, however, by explicitely computing the forward and backward transform either by FFT (in an order $N^d \log N$) or by direct summation (in an order N^{d+1} operations; this operation count stems from the fact that the d-dimensional transforms can be evaluated as a sequence of one-dimensional transforms). The computational steps (and the corresponding operation counts) are as follows:

Operation count using

	FFT	direct transforms
$\hat{f}_{\underline{k}}, \hat{g}_{\underline{k}}$ ↓	$\sim 2N^d \log N$	$\sim 2N^{d+1}$
$f_{\underline{j}}, g_{\underline{j}}$ ↓	N^d	N^d
$h_{\underline{j}} = f_{\underline{j}} g_{\underline{j}}$ ↓	$\sim N^d \log N$	$\sim N^{d+1}$
$\hat{h}_{\underline{k}}$		
order of the total operation count:	$N^d \log N$	N^{d+1}

For modest values of N ($\lesssim 32$) the FFT version is faster by only a factor of one to four than the direct transform method. However, both methods are at least a factor of the order N^{d-1} faster than direct evaluation of the convolution sum. In three dimensions this is a saving of the order of $N^2 \approx 1000$ if $N \approx 32$.

In summary, for computation of $\hat{s}_{\underline{k}}$ and $\hat{E}_{\underline{k}}$, the transforms of $\underline{u} \times \underline{\omega}\,(\underline{x}_{\underline{j}})$ and $\frac{1}{2}\,\underline{u}\cdot\underline{u}\,(\underline{x}_{\underline{j}})$, respectively, the procedure is as follows: One starts with $\hat{\underline{u}}_{\underline{k}}$, computes $\hat{\underline{\omega}}_{\underline{k}} = i\,\underline{k} \times \hat{\underline{u}}_{\underline{k}}$ and transforms into real space to get $\underline{u}_{\underline{j}}$ and $\underline{\omega}_{\underline{j}}$. In real space we perform $\underline{s} = \underline{u} \times \underline{\omega}$ and $E = \frac{1}{2}\,\underline{u}\cdot\underline{u}$ for each point $\underline{x}_{\underline{j}}$. Then we return to wave number space by transforms on all three components of $\underline{s}$ and on E. This procedure requires six fields $u_1, u_2, u_3, \omega_1, \omega_2, \omega_3$ to be transformed into real space. If we use $(\underline{u}\nabla)\underline{u}$ instead of $\nabla(\underline{u}^2/2) - \underline{u} \times \underline{\omega}$ then eleven transforms are necessary ($u_1, u_2, u_3, \partial u_1/\partial x_1, \partial u_1/\partial x_2, \partial u_1/\partial x_3, \partial u_2/\partial x_1, \ldots, \partial u_3/\partial x_2$; using $\partial u_3/\partial x_3 = -\partial u_1/\partial x_1 - \partial u_2/\partial x_2$).

3.2.4 Aliasing Errors

Returning to the problem of aliasing, one can choose between tolerating this error (which is the essence of the "pseudo-spectral" approach) or spending additional computations for elimination. In fact, an aliasing free convolution sum can be computed. For this purpose first we append zeros to extend the domain of definition of $\hat{f}_{\underline{k}}$ and $\hat{g}_{\underline{k}}$ to $\|\underline{k}\| \le 2\, k_{max}$, then we find the $(4K)^d$ transforms $f_{\underline{j}}, g_{\underline{j}}$ respectively, of the extended spectral fields, compute $h_{\underline{j}} = f_{\underline{j}}\, g_{\underline{j}}$ from which we compute $\hat{h}_{\underline{k}}$, the inverse extended transforms, and finally neglect the contributions $\hat{h}_{\underline{k}}$ with $\underline{k}$ outside the original range. It can be shown (Orszag 1971a) that this approach is consistent with a Galerkin approximation. Advanced transform methods have been designed which compute the same result with considerably reduced effort. Patterson and Orszag (1971) have shown, that an aliasing free computation is possible if one accepts truncating modes $\hat{f}_{\underline{k}}, \hat{g}_{\underline{k}}$ that lie outside a sphere of radius αK, $\alpha = 2\sqrt{2}/3 \approx 0.94$. This already eliminates some of the aliasing terms. The remainder is eliminated by averaging over the transforms of $h_{\underline{j}}$ and $h_{\underline{j}+\frac{1}{2}(1,1,1)}$. Thus, the (Galerkin) spectral approach only doubles the number of operations of the pseudo-spectral approach.

The necessity for eliminating aliasing terms has been deserved much discussion (see Orszag 1971b, 1972, Fox & Orszag 1973, Salu & Knorr 1975, Schamel & Elsässer 1976). The main results are:

- Although aliasing may result in instabilities this instability can be prohibited (as in finite difference schemes), if the numerical scheme conserves the energy integral $\frac{1}{2}\int |\underline{u}|^2\, d\underline{x}$ in the absence of forcing, viscous dissipation and time-differencing errors. This is the case in the present scheme since the non-linear term $\underline{u} \times \underline{\omega}$, because it is orthogonal to $\underline{u}$, cannot produce any kinetic energy regardless of which approximation is being used and the pressure contributions are eliminated, see eq. (3-27).

- Aliasing contributions are small if the velocity modes $\hat{u}_{\underline{k}}$ are small outside the inner sphere $|\underline{k}| < K/2$; if they are not, a finer resolution is indicated.

- In fact, experiences show that aliasing errors become important only when the solution to the continuum problem develops some structure like a shock or a shear layer that can not be resolved with the used number of modes.

Finally, one should note, that it is only in the spectral schemes that one is able to eliminate the aliasing effects. In all finite difference schemes one simply ignores such errors.

3.2.5 Accuracy

For accurate numerical simulation a fast decrease in the error of the approximating function with increasing spatial resolution N is crucial. We shortly discuss the accuracy of a Fourier series approximation

$$f_N(x) = \sum_{|k|<N} a_k\, e^{ikx}$$

to some function f defined for $0 \le x < 2\pi$ and extended to $-\infty < x < \infty$ by periodicity. If f has continuous derivatives up to order $p-1$ everywhere in $0 \le x \le 2\pi$ (including the end points), $f^{(p)}$ is continuous except for possible jumps at a finite number of points $0 = x_1 < x_2 < \dots < x_D = 2\pi$ and $f^{(p+1)}$ is integrable, then repeated integration by parts gives

$$\begin{aligned}
2\pi a_k &= \int_0^{2\pi} f(x)\, e^{-ikx}\, dx \\
&= \frac{1}{ik}\left\{ -\underbrace{\left[f(x)\, e^{-ikx} \right]_0^{2\pi}}_{=0} + \int_0^{2\pi} f^{(1)}(x)\, e^{-ikx}\, dx \right\} = \dots = \\
&= \left(\frac{1}{ik}\right)^p \left\{ -\underbrace{\left[f^{(p-1)}(x)\, e^{-ikx} \right]_0^{2\pi}}_{=0} + \int_0^{2\pi} f^{(p)}(x)\, e^{-ikx}\, dx \right\} \\
&= \left(\frac{1}{ik}\right)^p \sum_{d=1}^{D-1} \int_{x_d}^{x_{d+1}} f^{(p)}(x)\, e^{-ikx}\, dx \\
&= \frac{1}{(ik)^{p+1}} \left\{ f^{(p)}(0^+) - f^{(p)}(2\pi^-) + \sum_{d=2}^{D-1} e^{-ikx_d} \left[f^{(p)}(x_d^-) - f^{(p)}(x_d^+) \right] \right. \\
&\qquad \left. + \int_0^{2\pi} f^{(p+1)}(x)\, e^{-ikx}\, dx \right\}. \qquad (3\text{-}37)
\end{aligned}$$

This shows that $a_{\pm k} = O(1/k^{pm})(k\to\infty)$. Therefore the approximation error is

$$|f_N(x) - f(x)| = O\left(\frac{1}{N^p}\right) \qquad (N \to \infty), \tag{3-38}$$

and the exponent cannot be improved as long as there is a discontinuity in $f^{(p)}$. Even if f is infinitely differentiable in $0 < x < 2\pi$ so that the sum in (3-37) vanishes, the convergence order is limited by a "terminal discontinuity" in f or some higher derivative (Gibbs' phenomenon). In case of a perfectly smooth function, however, the approximation is "infinite order" accurate (Orszag & Israeli 1974) since the error decreases more rapidly than any finite power of $1/N$. However, as noted in § 3.1.3, this result is relevant only if $N > N_{min}$, where N_{min} is the minimum required for resolution of all important scales. But even with respect to the required N_{min} Fourier approximations are superior to finite difference methods (FDM) at least for periodic fields as explained below.

For a FDM at least 4 grid points per wave length are required to give reasonable representation of derivatives. A Fourier representation, on the other hand, requires only two degrees of freedom (real and imaginary part) per wave. I.e., one can expect that in a d-dimensional space a FDM should include of the order 2^d more degrees of freedom than the Fourier SM for the same resolution. In fact, a finite difference simulation of the present box problem has been performed by Clark et al. (1977) using a 64^3 grid. The results are comparable to those of Orszag & Patterson (1972b) for $N=32$. It is interesting to note that the computing time of the finite difference simulation is larger by a factor of more than ten than that of the spectral scheme.

3.3 The Channel-Problem

We now consider again the non-steady flow of an incompressible fluid between two parallel plates. As in the finite difference scheme the flow field is assumed to be periodic in the x_1- and

x_2 -directions but satisfies the no-slip condition at the walls to which x_3 is the normal coordinate. For the spectral approach it is convenient to normalize the length scales such that the walls are at $x_3 = \pm 1$ and the computational domain extends between

$$\begin{aligned} 0 \le x_i \le L_i \qquad & i = 1,2, \\ -1 \le x_3 \le 1 \, . & \end{aligned} \tag{3-39}$$

Because of the assumed periodicity, our trial functions are composed of Fourier components

$$e_{k_1 k_2}(x_1, x_2) = \exp\left[i 2\pi \left(k_1 x_1 / L_1 + k_2 x_2 / L_2 \right) \right] \tag{3-40}$$

with respect to the x_1 and x_2 coordinates but a different set of functions $T_{k_3}(x_3)$ for the normal coordinate.

3.3.1 Why not Fourier Functions for the Normal Coordinate?

Fourier functions would not be appropriate for the x_3-direction due to the following reasons:

a) It seems not to be possible to construct an ansatz function in terms of Fourier components for all three coordinates which individually satisfies the Dirichlet boundary condition and the continuity equation while being complete in the sense of allowing for symmetric and anti-symmetric solutions. For example

$$\underline{u}(\underline{x}) = \begin{Bmatrix} \frac{L_1}{i 2\pi k_1} & \sin(\pi k_3 x_3) \\ \frac{L_2}{i 2\pi k_2} & \sin(\pi k_3 x_3) \\ \frac{2}{\pi k_3} & \left(\cos(\pi k_3 x_3) - (-1)^{k_3} \right) \end{Bmatrix} \cdot e_{k_1, k_2} \tag{3-41}$$

$$|k_i| > 0 \, , \quad i = 1,2,3$$

satisfies $\underline{u}(x_3=\pm 1)=0$ and $div\ \underline{u} = 0$ but represents only anti-symmetric u_1, u_2 and symmetric u_3 solutions. If $\cos(\pi k_3 x_3) - (-1)^{k_3}$ is used instead of $\sin k_3 x_3$ we satisfy the boundary conditions but not the continuity equation.

b) If we drop the request for ansatz functions, which satisfy the boundary conditions and the continuity equation term by term, trigonometric functions are still not attractive because the resultant accuracy would by no means be better than that of finite difference schemes with a low, finite order of accuracy. This is so because our solutions are non-periodic in the x_3 direction so that either the solutions or at least a low order normal derivative of it are different at the two end points $x_3=\pm 1$. As a consequence the approximation is of order $N^{-q}\ (N\to\infty)$ where q is low (one or two) and fixed. This is commonly known as Gibbs' phenomenon; see § 3.2.5.

c) Finally, trigonometric functions behave very bad if the solution contains a narrow boundary layer at the walls as it typically appears in solutions of Helmholtz' problems like the following one-dimensional one:

$$\frac{d^2}{dx^2}u(x) - H^2 u(x) = -1\ ,\quad -1\le x\le 1$$
$$u(-1) = u(+1) = 0\ ;\quad H^2 \ge 0 \qquad (3\text{-}42)$$

This equation describes e.g. the axial velocity in a channel flow of conducting fluid under an imposed constant magnetic field perpendicular to the walls. In this case H is known as the Hartmann number. Similar problems arise in the channel flow problem if the Navier Stokes equations are solved by a spectral method with implicit treatment of the viscous terms. The exact solution to (3-42) is

$$u(x) = \frac{1}{H^2}\left(1 - \frac{\cosh(Hx)}{\cosh H}\right)\ , \qquad (3\text{-}43)$$

see Fig. . We see that for $H\gg 1$ such a problem exhibits a narrow boundary layer the thickness of which is of order $1/H$. It approaches a step function for $H\to\infty$ so that Gibbs' phenomenon is to be expected.

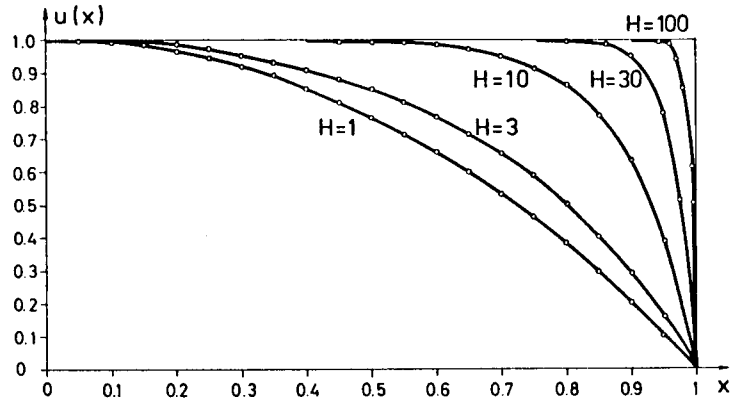

Fig. 3-3 Solution $u(x)$ (normalized by $u(0)$) of the one-dimensional Helmholtz equation (Hartmann flow profile) for different values of the Hartmann number H or Helmholtz coefficient H^2. Note the thin boundary layer for large values of H .

Statements b) and c) can be easily demonstrated. Let us use ansatz functions

$$w_k(x) = \cos\left(\tfrac{\pi}{2}(2k-1)x\right)\ ,\quad k=1,2,\ldots \qquad (3\text{-}44)$$

which satisfy the boundary conditions $w_k(\pm 1)=0$. With

$$(w_m, w_n) = \int_{-1}^{1} w_m(x)\, w_n(x)\, dx = \delta_{m,n}$$
$$(1, w_m) = \frac{4(-1)^{m+1}}{\pi(2m-1)} \qquad m,n\in\{1,2,\ldots\} \qquad (3\text{-}45)$$

one obtains from eq. (3-9a) or (3-9b), i.e., from the least squares or the Galerkin approximations equally and also from the tau-method the solution

$$w(x) = \sum_{k=1}^{N} \hat{u}_k \, w_k(x) \qquad (3\text{-}46)$$

with

$$\hat{u}_k = \frac{(-1)^{k+1} \cdot 4/\pi}{(2k-1)\left[(2k-1)^2\pi^2/4 + H^2\right]}.$$

The truncation error is

$$\varepsilon = \left| \sum_{k=N+1}^{\infty} \hat{u}_k \, w_k(x) \right| \le \sum_{k=N+1}^{\infty} |\hat{u}_k| \qquad (3\text{-}47)$$

which is of order N^{-2} for $N \to \infty$ but the error varies like N^0 as long as H^2 is not small compared to N^2. In Fig. 3-4 the well known Gibbs phenomenon becomes obvious.

All these deficiencies are avoided if we specify the ansatz functions $T_{k_3}(x_3)$ or - for shortness - $T_m(x)$ to be suitable orthogonal polynomials. In particular Chebyshev polynomials are attractive because they are so closely related to the cosine functions that fast transform algorithms can be used. Gottlieb & Orszag (1977) have shown that Legendre polynomials may have even better convergence properties, but no fast and stable Legendre transform is available. (As noted by Orszag & Kells (1978) this drawback might be not so serious because fast transform methods change the operation count only from N^{d+1} to $N^d \log N$ for a d-dimensional transform, see § 3.2.3.)

Subsequently we first discuss the basic properties of Chebyshev polynomials, then show its superior convergence properties for the above one-dimensional test problem and then discuss applications to the Navier-Stokes equations.

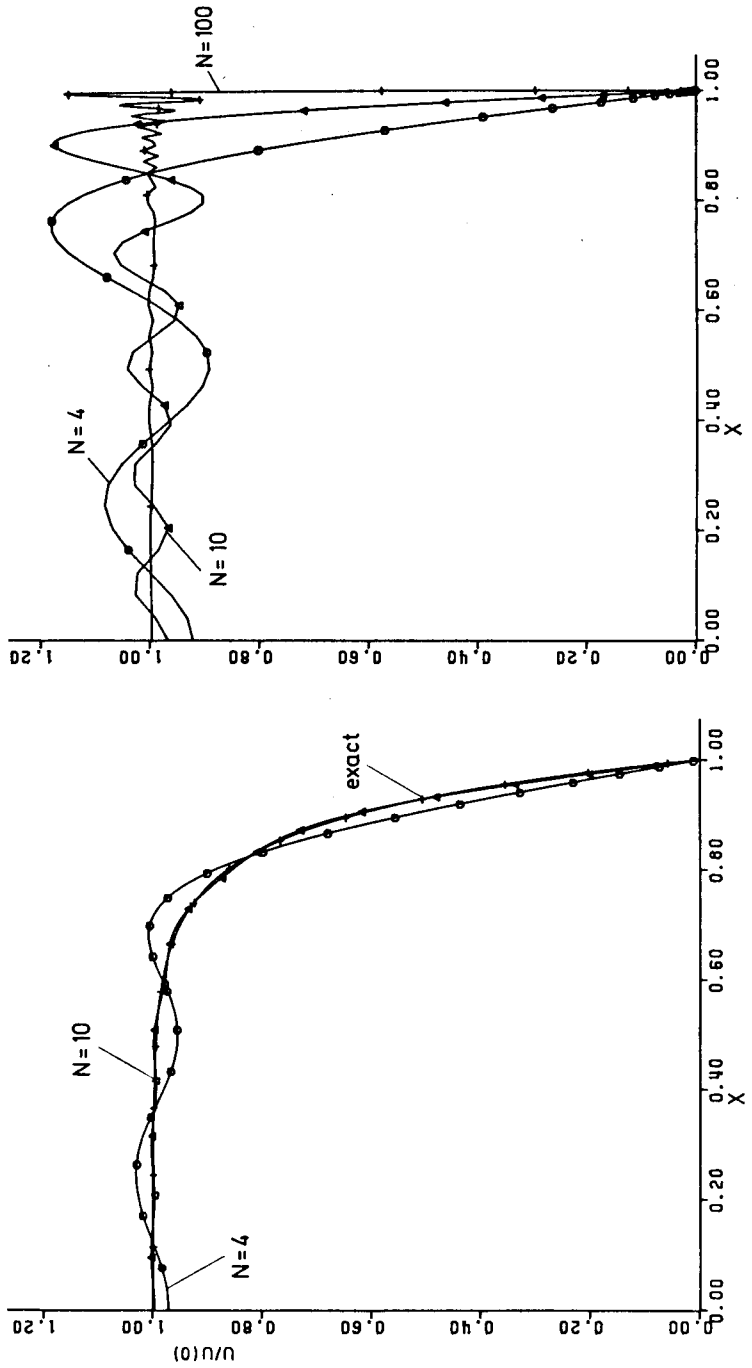

Fig. 3-4 Fourier SM solution to the model equation for different numbers of degrees of freedom N for $H=10$ (left) and $H=1000$ (right). Note the strong oscillations which appear for insufficient resolution.

3.3.2 Chebyshev Polynomials

The definition and properties of Chebyshev polynomials are summarized in the appendix. See also Fox & Parker (1968) and Gottlieb & Orszag (1977). In short, Chebyshev polynomials are defined by

$$T_n(x) = \cos(n \arccos x), \quad n = 0,1,2,\ldots \quad ,|x| \le 1 \qquad \text{(T-1)}$$

(Here the equation numbers T-1,... refer to the equations of the appendix). They form a set of orthogonal polynomials with respect to the inner product

$$(f,g) \equiv \int_{-1}^{1} \frac{f(x)\,g(x)}{\sqrt{1-x^2}}\,dx \qquad \text{(T-12)}$$

which contains a weighting function that emphasizes the boundary regions of the interval $[-1, 1]$. The zeros and extrema of $T_N(x)$ lie at points which concentrate near the boundaries. In the inner region the distance between these points is of order N^{-1}, near the endpoints it is of order N^{-2}. So, if collocation is used at these points, e.g., it is intuitively clear that the resolution of the boundary layer is good.

The orthogonality of the finite discrete cosine transform carries over to the discrete Chebyshev transform if the discrete points are the points of the extreme values of the highest polynomials. Therefore, fast cosine transform algorithms can be used for the discrete Chebyshev transform.

Derivatives are not quite as simple to compute as for Fourier functions, but nearly. Whereas the derivative of a Fourier function can be described by the same function, the derivatives of two Chebyshev polynomials can be expressed by one Chebyshev polynomial. Therefore we do not get diagonal systems as in case of Fourier approximations rather than tridiagonal systems.

The essential advantage of Chebyshev polynomials is the fact that it eliminates the Gibbs phenomenon. Let $f(x)$ be infinitely differentiable in $|x| \le 1$ (with one-sided derivatives at the end-points). Let $x = \cos\vartheta$ and $g(\vartheta) \equiv f(\cos\vartheta)$. Then $g(\vartheta)$ is an

infinitely di rentiable, even, periodic function of ϑ. Therefore, the partial sums of the cosine expansion of $g(\vartheta)$ do not exhibit the Gibbs phenomenon. But, from (T-1),

$$f(x) = g(\vartheta) = \sum_{n=0}^{\infty} a_n \cos n\vartheta = \sum_{n=0}^{\infty} a_n T_n(x)\,; \qquad \text{(3-48)}$$

consequently the same is true for the Chebyshev series approximation of $f(x)$ no matter which boundary conditions are used.

3.3.3 The One-Dimensional Helmholtz Problem

For illustration of the use of Chebyshev polynomials we solve our test problem, the Helmholtz' equation (3-42). It will be shown that the accuracy of the Chebyshev SM is far better than that of the Fourier SM for this problem and also superior to finite difference schemes as long as the boundary layer is not exceedingly small.

3.3.3.1 The trial function

Ansatz functions which satisfy the boundary conditions are

$$w_k(x) = \begin{cases} T_k(x) - T_0(x) & , k \text{ even} \\ T_k(x) - T_1(x) & , k \text{ odd} \end{cases} \quad , k \ge 2\,. \qquad \text{(3-49)}$$

However, the analysis becomes simpler and the resultant system of equations has a nearly tridiagonal matrix if we instead use

$$w(x) = \sum_{k=0}^{N} a_k T_k(x) \quad ; \; N \text{ even} \qquad \text{(3-50)}$$

together with the "boundary condition"

$$\begin{aligned} w(1) &= \sum_{k=0}^{N} a_k = 0\,. \\ w(-1) &= \sum_{k=0}^{N} (-1)^k a_k = 0\,. \end{aligned} \qquad \text{(3-51)}$$

Addition and subtraction gives

$$a_0 = -\sum_{\substack{k=0 \\ k\ even}}^{N} a_k \,, \qquad a_1 = -\sum_{\substack{k=0 \\ k\ odd}}^{N} a_k \,. \tag{3-52}$$

In fact, all odd coefficients are zero for this problem which has an even solution.

3.3.3.2 Galerkin (GAL)

Application of the Galerkin method, eq. (3-9b), and use of the orthogonality (T-13) and recurrence relations (T-21) results after some algebra in the following system of equations

$$\begin{aligned}
&\frac{c_{j-2}}{4j(j-1)}\,a_{j-2} - \left(\frac{1}{2(j^2-1)} + \frac{1}{H^2}\right)a_j + \frac{\alpha(j)}{4j(j+1)}\,a_{j+2} = -\frac{1}{4H^2}\,\delta_{j,2} \qquad j = 2,4,\dots,N-2 \\
&\frac{c_{j-2}}{4j(j-1)}\,a_{j-2} - \left(\frac{\alpha(j)}{4j(j-1)} + \frac{1}{H^2}\right)a_j = 0 \qquad j = N \\
&a_0 + a_2 + \dots + a_N = 0
\end{aligned} \tag{3-53}$$

which are $N/2+1$ equations for the $N/2+1$ unknowns $a_0, a_2, \dots, a_N$. In this Galerkin approach $\alpha(j)$ comes out to be unity for all j (it will be different in the collocation approach). This system of equations possesses a coefficient matrix as given schematically below:

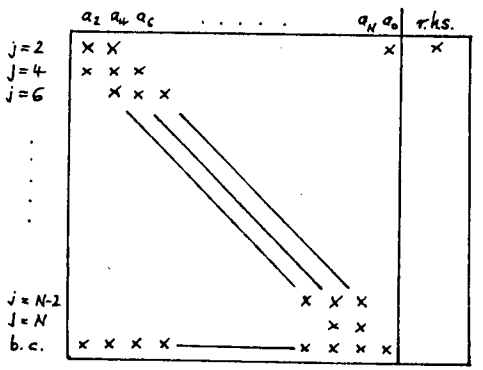

(3-54)

Except for the last all equations are diagonally dominant so that the equations can be solved numerically stable using a tailored variant of the Gaussian elimination method with an order $8N$ multiplications and divisions. The resultant solution for specific values of H and N is plotted in Fig. 3-5.

3.3.3.3 Collocation (COL)

Next we construct the corresponding system from collocation. Different possibilities exist for choice of the collocation points x_j. Here we use the two boundary points $x = \pm 1$ plus $N-1$ internal points. The latter are chosen to be

$$x_j = \cos\frac{j\pi}{N}\,, \qquad j = 1,2,\dots,N-1. \tag{3-55}$$

If additional unknowns are introduced for x_0 and x_N, this allows one to use the transformation (T-27); the unknowns can be eliminated thereafter. The resultant system is identical to (3-53) except that $\alpha(j)=2$ for $j=N-2,N$. Fox & Parker (1968) and Wright (1964) proposed to use $x_j = \cos j\pi/(N-2)$, $j=0,\dots,N-2$ instead of (3-55). However, we found the resultant system to be numerically unstable.

3.3.3.4 Tau-method (TAU)

Finally the tau-method is used. Inserting the trial solution (3-50) into (3-42) and comparing coefficients of T_k for $k=0,\dots,N-2$ gives

$$a_k^{(2)} - H^2 a_k = -\delta_{k,0}\,, \qquad k = 0,\dots,N-2.$$

Combining this set of equations with the recurrence relations (T-21) and the boundary conditions as before we obtain

$$\begin{aligned}
&\frac{c_{k-2}}{4k(k-1)}\,a_{k-2} - \left(\frac{e_{k+2}}{2(k^2-1)} + \frac{1}{H^2}\right)a_k + \frac{e_{k+4}}{4k(k+1)}\,a_{k+2} = -\frac{1}{4H^2}\,\delta_{k,2} \\
&a_0 + a_2 + \dots + a_N = 0.
\end{aligned} \tag{3-56}$$

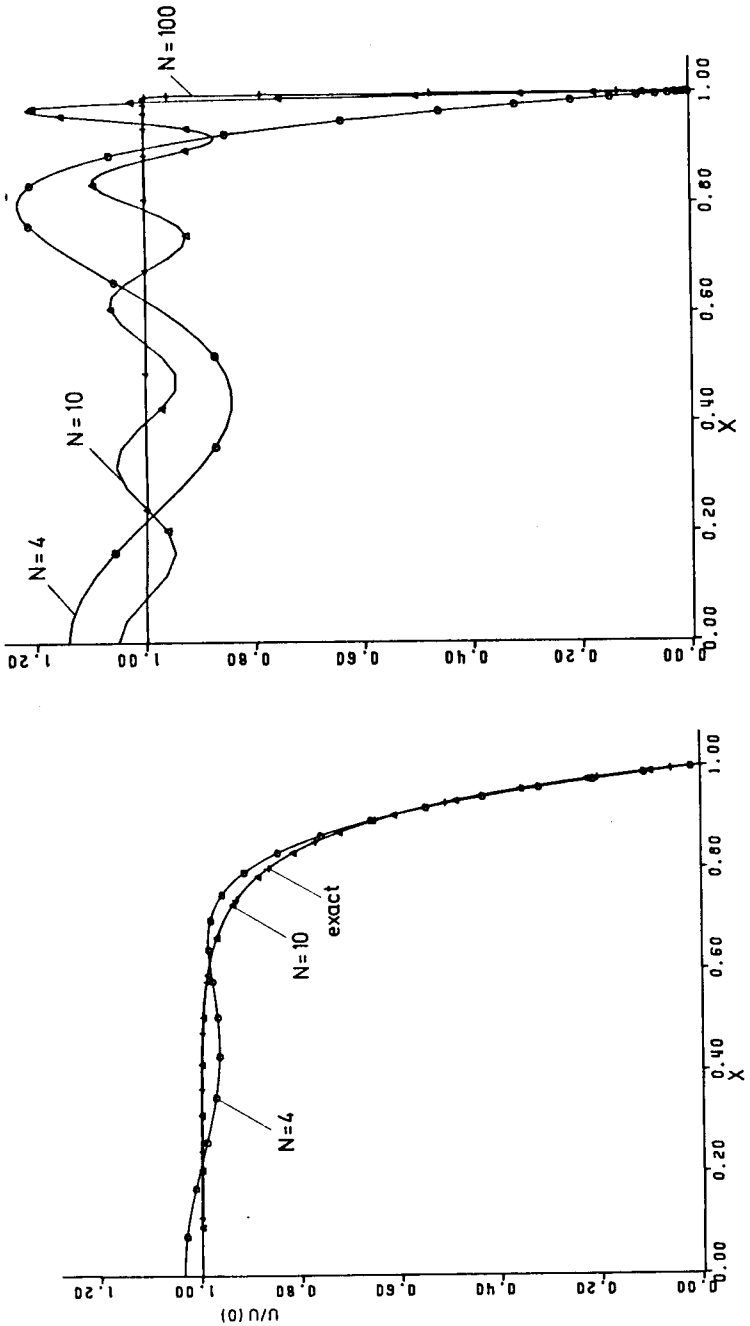

Fig. 3-5 Same as Fig. 3-4 for the Chebyshev SM ($H=10$, left; $H=1000$, right).

The only differences from the Galerkin equations appear in the equations for $k = N-2$ and N . The function w determined by these equations is an exact solution of the modified problem

$$w'' - H^2 w = -1 + \tau_{N-1} T_{N-1} + \tau_N T_N . \qquad (3\text{-}57)$$

Here the unknown parameters τ_n are equal to $-H^2 a_n$.

3.3.3.5 Results of the Chebyshev spectral method in comparison with finite difference and Fourier spectral methods

Subsequently, results are presented which are obtained from the above Chebyshev SM. Its accuracy is compared to the Fourier SM solution given in §3.3.1. Also, the same problem has been solved by two variants of a second order accurate finite difference scheme. In the first the given differential equation is solved on an equidistant grid. The results are denoted by "FD". In the second ("FDV") variable grid spacings, respectively a coordinate transformation, are used such that the transformed coordinates are

$$x_i = \frac{1}{\sqrt{1-d}} \tanh\left(\frac{1}{C}\,\frac{i-1}{M}\right), \quad i = 1, \ldots, M+1$$

$$(d \equiv 1/H, \; C \equiv 1/\operatorname{artanh}\sqrt{1-d}\,) . \qquad (3\text{-}58)$$

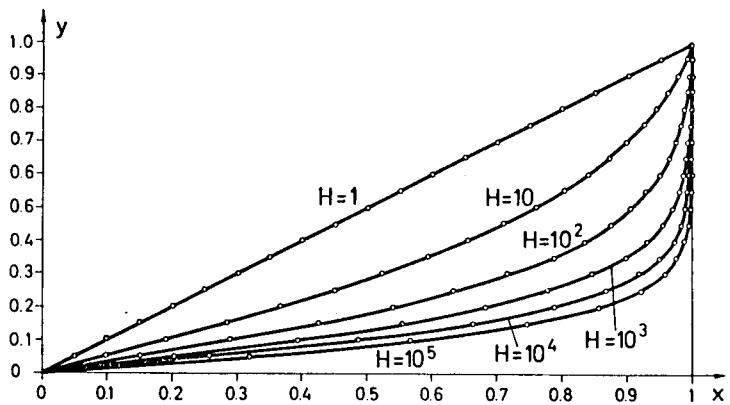

Fig. 3-6 Transformation $y(x)$ used for the finite difference scheme FDV.

These points are very densly distributed in the l ıdary layer of thickness d , see Fig. 3-6. The maximum relative error of the approximate solutions u_i at these points in comparison to the exact solution $u(x_i)$ is

$$e_{max} \equiv \max_{i=1,\dots,M+1} \left| \frac{u_i - u(x_i)}{u(0)} \right| . \qquad (3\text{-}59)$$

In Fig. 3-7 the error e_{max} is plotted over the number M of degrees of freedom (even Chebyshev or Fourier coefficients or rid points in the interval $0 \le x < 1$). The number of multiplications and divisions is of order $8M$ in the SM (excluding function evaluation from computed Chebyshev coefficients) and $5M$ in the finite difference schemes so that the methods are roughly comparable for about the same values of M .

Fig. 3-7 shows the maximum errors for a fixed Hartmann number $H = 10^3$. The errors decrease like $1/M^2$ in both FD and FDV (it is noteworthy that a variable spacing does not change the convergence order if the spacing varies continously). The errors of the Fourier SM are even larger than those of FD but of the same order. In the Chebyshev SM, GAL and COL give results which cannot be distinguished at the scales of the drawing. The errors of TAU are slightly larger. For large M the effect of round-off errors is such that e_{max} grows for the finite difference schemes but remains constant at a low level in the SM. In contrast to the second order accuracy of both FD, FDV and Fourier SM the Chebyshev SM is infinite order accurate. This is demonstrated in Fig. 3-8, where e_{max} is plotted against M^2/H for GAL and TAU. Four different values of H have been used ($H = 10^2$ to $H = 10^5$) giving the same straight line. This shows that

$$e_{max} \approx const \cdot 10^{-M^2/H} \qquad (3\text{-}60)$$

with const of order one. Therefore, for sufficiently (though perhaps impractical) large M the Chebyshev SM always becomes most accurate.

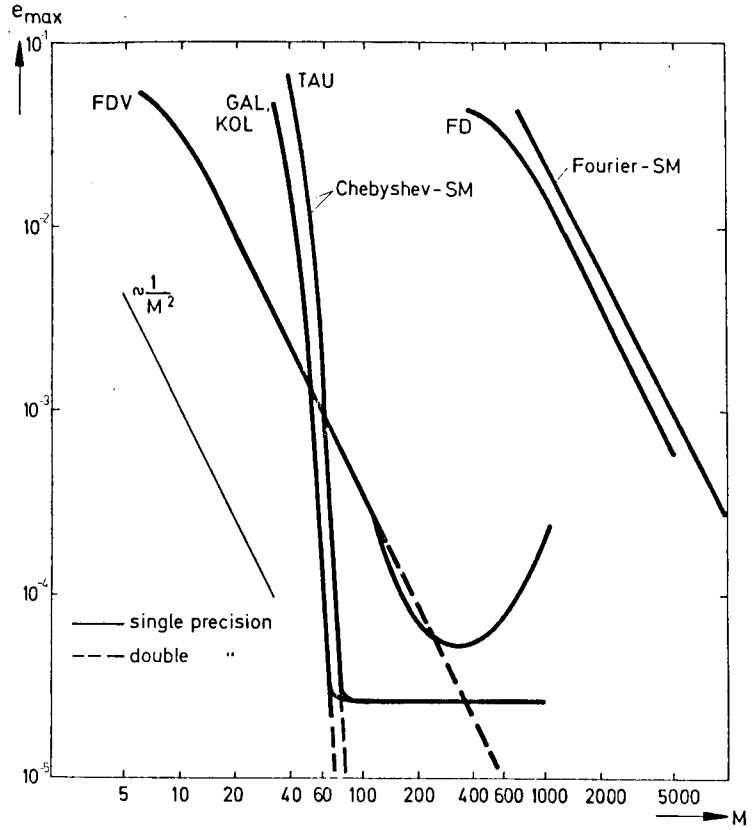

Fig. 3-7 Maximum relative error e_{max} for the model problem with $H = 1000$ for the Chebyshev spectral method variants (Galerkin GAL, collocation COL, tau method TAU), for the Fourier spectral method and for second order finite difference solutions with fixed (FD) or variable (FDV) grid spacings. M = number of degrees of freedom. (single precision=7 digits, double precision=15 digits.)

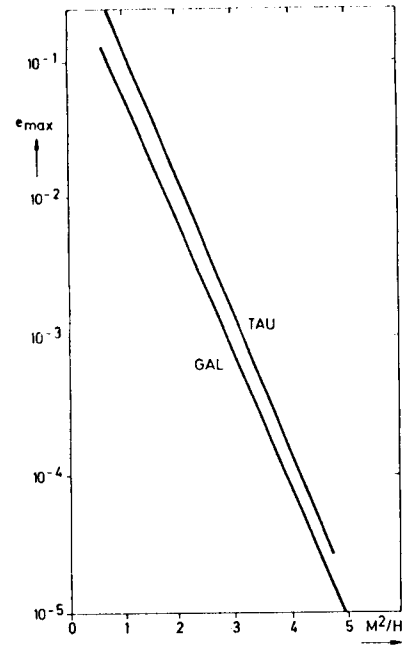

Fig. 3-8
Maximum relative error e_{max} for the model problem in the Chebyshev SM (Galerkin and tau versions); M = number of degrees of freedom, H = Hartmann number. Note the exponential error decay, eq. (3-60).

Fig. 3-9 shows that this "turn-over" value of M is dependent on H. For small to moderate values, the SM is clearly superior to the finite difference scheme. The latter is very inaccurate if constant spacings are being used. For large H, however, the FDV method is clearly competitive. One can show that

$$
\begin{aligned}
M &\sim H && \text{(FD or Fourier SM)} \\
M &\sim \log \sqrt{H} && \text{(FDV)} \qquad (3\text{-}61) \\
M &\sim \sqrt{H} && \text{(Chebyshev SM)}
\end{aligned}
$$

degrees of freedom are required in the different methods in order to resolve the boundary layer properly. Perhaps it is not fair to compare the FDV-version, in which a transformation, which is tailored to the present problem, is employed, to the SM applied to the non-transformed equations. One might consider combining SM with coordinate transformation, e.g. by using other

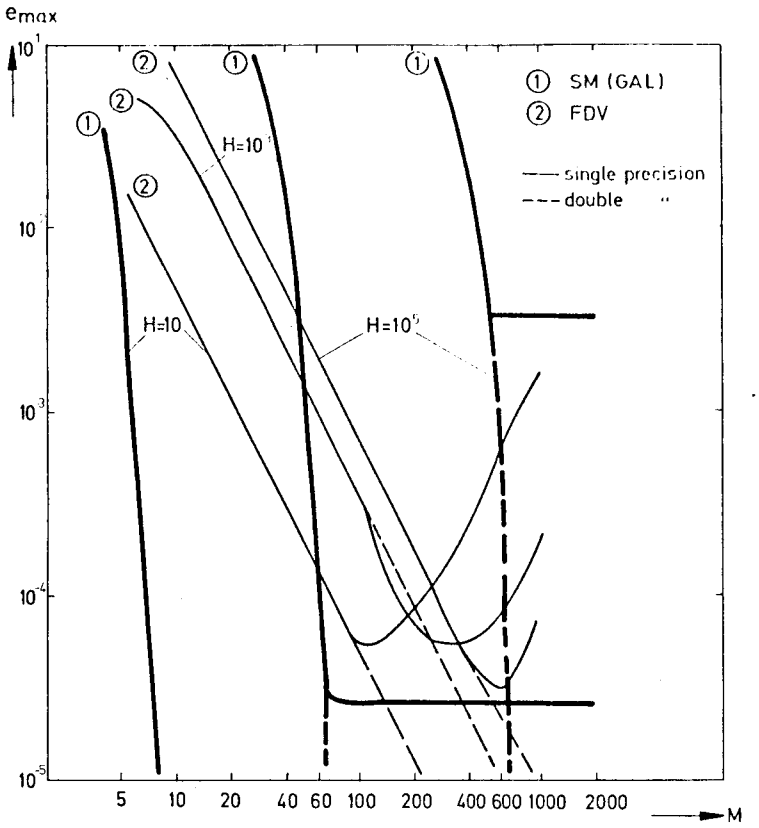

Fig. 3-9 Maximum relative error for $H = 10, 10^3, 10^5$ in ① the Chebyshev Galerkin spectral method and ② the finite difference scheme with variable spacings (FDV) versus M, the number of degrees of freedom.

grid points for collocation. However, this would result in a set of linear equations with a full coefficient matrix because the orthogonality relation no longer applies. The increased effort for solving this linear system is comparable to the effort of the original collocation formulation at increased M both having the same accuracy.

In summary, the SM gives very accurate results if the number of polynomials is sufficiently large ($e_{max} \leq 10^{-5}$ for $M \gtrsim \sqrt{5}\#$). A higher accuracy requires only a slightly increased number of M since the error decreases exponentially fast with M, see eq. (3-60). In any case, a finite difference scheme with properly transformed coordinates or continously varying grid spacings (FDV) is preferable to a scheme with constant spacings (FD). The SM is superior to the FDV method for moderately large values of the Hartmann number # (or Helmholtz coefficient $\#^2$), whereas for very thin boundary layers FDV is more effective for practical accuracy requirements.

Finally it should be noted that the above solution procedures can easily be generalized to Helmholtz problems with a non-constant right hand side and mixed Dirichlet-Neumann boundary conditions. If the boundary conditions are either Dirichlet or Neumann at both sides then a separation of even and odd solution parts is possible.

3.3.4 Application to the Solution of the Navier Stokes Equations

Application of Fourier and Chebyshev expansions to the solution of the channel flow problem has been proposed already in 1971 (Orszag, 1971c) in terms of a Galerkin approximation. However, a successful construction of a corresponding computer code has not become known until recently. The present authors have been working on such a code for some time but have found difficulties with respect to satisfying the boundary conditions and the continuity equation rigorously while using a second order time integration scheme for the Navier Stokes equations with implicit formulation of the viscous terms (Kleiser & Schumann, 1978).

This problem has also been discussed by Moin et al. (1978). Therefore we will not report on results of this work which is still in progress. Recently, Orszag & Kells (1978) have developed such a method and applied to the transition process from laminar to turbulent flow. A fractional time stepping scheme is used. The time differencing truncation errors are of the order $\sigma(\Delta t^2)$ for the nonlinear terms but of $\sigma(\Delta t)$ only for the viscous terms. Orszag & Kells claim that the latter errors are negligible because of the smallness of the inverse Reynolds number. It is not obvious whether this is correct because of the high derivatives which are relevant for the viscous forces. In the fractional integration scheme the continuity equation is not satisfied after completion of the time step but only in an intermediate step. This might be acceptable but further investigations are necessary.

Finally we mention the nonlinear transition studies of Murdock (1977) and Wray et al. (1977) using different spectral methods for boundary-layer problems. In all these cases the Navier-Stokes equations are integrated in time. Non-linear eigenvalue problems for the transition of several flow cases have been investigated by means of the SM by Herbert (1977).

APPENDIX: CHEBYSHEV POLYNOMIALS

A.1 Definition and Simple Properties

Chebyshev polynomials $T_n(x)$ can be defined for $-1 \le x \le 1$ by

$$T_n(x) \equiv \cos(n \arccos x), \quad n = 0, 1, 2, \ldots . \tag{T-1}$$

$(\pi \ge \vartheta \equiv \arccos x \ge 0)$. From

$$T_{n\pm1}(x) = \cos(n\vartheta \pm \vartheta) = \cos n\vartheta \cos\vartheta \mp \sin n\vartheta \sin\vartheta \tag{T-2}$$

one obtains the recurrence relation

$$T_{n+1}(x) + T_{n-1}(x) = 2x\, T_n(x), \quad n \ge 1. \tag{T-3}$$

Obviously from (T-1) $T_0(x) = 1$, $T_1(x) = x$, so that from (T-3):

$$\begin{aligned} T_0(x) &= 1 & T_1(x) &= x \\ T_2(x) &= 2x^2 - 1 & T_3(x) &= 4x^3 - 3x \\ T_4(x) &= 8x^4 - 8x^2 + 1 & T_5(x) &= 16x^5 - 20x^3 + 5x \\ &\ldots & &\ldots \end{aligned} \tag{T-4}$$

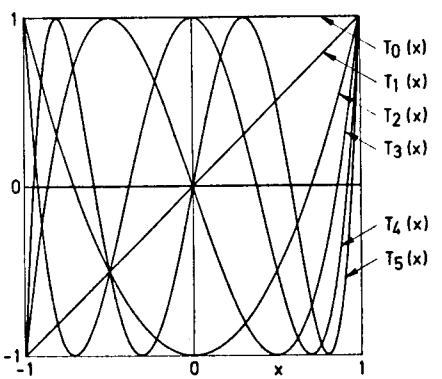

Fig. A-1:
The Chebyshev polynomials $T_0(x)$ to $T_5(x)$

See Fig. A-1. The polynomials are even or odd depending on n

$$T_n(-x) = (-1)^n T_n(x). \tag{T-5}$$

A recursion for the even and odd polynomials separately is obtained combining (T-3) for $n = k, k+1,$ and $k+2$:

$$T_{n+2} - (4x^2 - 2) T_n + T_{n-2} = 0 \tag{T-6}$$

Some general statements on the values of $T_n(x)$ follow from the above equations:

$$-1 \le T_n(x) \le 1 \qquad \text{for } -1 \le x \le 1 \tag{T-7}$$

$$T_n(\pm 1) = (\pm 1)^n \tag{T-8}$$

$$T_n(0) = \begin{cases} 0 & n \text{ odd} \\ 1 & n = 0, 4, 8, \ldots \\ -1 & n = 2, 6, 10, \ldots \end{cases} \tag{T-9}$$

$T_n(x_k) = 0$ for $\cos(n\vartheta_k) = 0 \Rightarrow$
$\vartheta_k = (2k-1)\pi/(2n) \Rightarrow$ the roots are

$$x_k = \cos\left(\frac{2k-1}{n}\frac{\pi}{2}\right), \quad k = 1, \ldots, n. \tag{T-10}$$

The extreme values $T_n(x_j) = \pm 1$ are reached if $\cos n\vartheta_j = \pm 1 \Rightarrow$

$$x_j = \cos\left(\frac{j\pi}{n}\right), \quad j = 0, \cdots, n \tag{T-11}$$

with $T_n(x_j) = (-1)^j$.

A.2 Orthogonality

The polynomials T_n are orthogonal on $[-1, 1]$ with respect to the inner product

$$(f, g) = \int_{-1}^{1} \frac{f(x)\, g(x)}{\sqrt{1-x^2}}\, dx \qquad \text{(T-12)}$$

for which

$$(T_m, T_n) = \int_{-1}^{1} \frac{T_m(x)\, T_n(x)}{\sqrt{1-x^2}}\, dx = \int_0^{\pi} \cos m\vartheta \cos n\vartheta \, d\vartheta .$$

From the orthogonality of the cosine functions follows:

$$(T_m, T_n) = \frac{\pi}{2} c_n \delta_{m,n} \quad , \quad m, n \in \{0, 1, \dots\} \qquad \text{(T-13)}$$

with $c_0 \equiv 2$, $c_n \equiv 1$, $n \geq 1$. Also the "discrete" orthogonality carries over: For the points of extreme values given by (T-11), $x_j = \cos(j\pi/M)$ we have

$$\sum_{j=0}^{M} b_j T_k(x_j)\, T_l(x_j) = \frac{M}{2 b_k} \delta_{k,l} \quad , \quad k, l \in \{0, \dots, M\} \qquad \text{(T-14)}$$

with $b_0 \equiv b_M \equiv 1/2$, $b_1 \equiv \dots \equiv b_{M-1} = 1$. This reduces to well known formulae by noting $T_r(x_j) = \cos(r j \pi / M)$. See Fox & Parker (1968).

A.3 Series Expansions and Derivatives

If

$$w(x) = \sum_{k=0}^{N} a_k T_k(x) \qquad \text{(T-15)}$$

then the r-th derivative is denoted by

$$\frac{d^r}{dx^r} w(x) = w^{(r)}(x) = \sum_{k=0}^{N-r} a_k^{(r)} T_k(x) \qquad \text{(T-16)}$$

($a_k^{(0)} = a_k$). For $a_k^{(r)}$ recurrence relations can be given which follow from

$$T_n'(x) = \frac{d}{dx} T_n(x) = \frac{d}{d\vartheta} \cos n\vartheta \cdot \frac{d\vartheta}{dx} = n \cdot \sin n\vartheta / \sin\vartheta ,$$

$$\frac{T_{n+1}'}{n+1} - \frac{T_{n-1}'}{n-1} = \frac{1}{\sin\vartheta} \left[\sin(n+1)\vartheta - \sin(n-1)\vartheta \right] = 2 \cos n\vartheta = 2 T_n , \quad n \geq 2 .$$

With the definitions

$$d_n \equiv \begin{cases} 0 & n < 0 \\ 1 & n \geq 0 \end{cases} , \quad c_n = \begin{cases} 0 & n < 0 \\ 2 & n = 0 \\ 1 & n \geq 1 \end{cases} , \quad e_n = \begin{cases} 1 & n \leq N \\ 0 & n > N \end{cases} \qquad \text{(T-17)}$$

these relations generalize to

$$\frac{c_n}{n+1} T_{n+1}' - \frac{d_{n-2}}{n-1} T_{n-1}' = 2 T_n \quad , \quad n \geq 0 . \qquad \text{(T-18)}$$

From (T-18) and $\frac{d}{dx} \sum_{k=0}^{N-r+1} a_k^{(r-1)} T_k = \sum_{k=0}^{N-r} a_k^{(r)} T_k$ one obtains by comparing coefficients:

$$2k\, a_k^{(r-1)} = c_{k-1} a_{k-1}^{(r)} - e_{k+r+1} a_{k+1}^{(r)} , \quad 1 \leq k \leq N-r+1 \qquad \text{(T-19)}$$

For $r = 1$ this reads

$$2k\, a_k = c_{k-1} a_{k-1}^{(1)} - e_{k+2} a_{k+1}^{(1)} , \quad 1 \leq k \leq N . \qquad \text{(T-20)}$$

Substitution of (T-19) with $r = 2$ gives

$$a_k = \frac{c_{k-2}}{4k(k-1)} a_{k-2}^{(2)} - \frac{e_{k+2}}{2(k^2-1)} a_k^{(2)} + \frac{e_{k+4}}{4k(k+1)} a_{k+2}^{(2)} \qquad \text{(T-21)}$$

$2 \leq k \leq N.$

This is a linear equation system for the $a_0^{(2)}, \dots, a_{N-2}^{(2)}$ if the a_k are known. The odd and even components are decoupled. Special values are

$$T_k'(\pm 1) = (\pm 1)^{k-1} k^2 \qquad \text{(T-22)}$$

$$T_k''(\pm 1) = (\pm 1)^k \frac{1}{3} k^2 (k^2 - 1) . \qquad \text{(T-23)}$$

From (T-3) one obtains the following algorithms:

a) Evaluation of $f(x) = \sum_{k=0}^{N} a_k T_k(x)$:

$$B_{N+1} = 0, \quad B_N = a_N,$$
$$B_k = a_k + 2x B_{k+1} - B_{k+2}, \quad k = N-1, \ldots, 1$$
$$f(x) = a_0 - B_2 + B_1 x \qquad \text{(T-24)}$$

This is a stable algorithm (Fox & Parker, 1968).

b) Differentiation (from T-20) $f'(x) = \sum_{k=0}^{N} a_k^{(1)} T_k(x)$ with

$$a_N^{(1)} = 0$$
$$c_{k-1} a_{k-1}^{(1)} = e_{k+2} a_{k+1}^{(1)} + 2k a_k, \quad k = N, \ldots, 1. \qquad \text{(T-25)}$$

The result $f'(x)$ is obtained thereafter as above. This algorithm is likely to give accumulation of round-off errors (see Wengle & Seinfeld 1978).

c) Integration (from T-19) with $F(x) = \int_x f(t)\,dt$:

$$F(x) = \sum_{k=0}^{N+1} A_k T_k(x)$$
A_0 = arbitrary integration constant
$$A_k = (c_{k-1} a_{k-1} - a_{k+1})/(2k) \quad k = 1, \ldots, N-1$$
$$A_k = a_{k-1}/(2k) \quad k = N, N+1. \qquad \text{(T-26)}$$

d) Transformation. Let

$$f_j = f(x_j) = \sum_{k=0}^{N} a_k T_k(x_j) \quad j = 0, \ldots, N$$

with $x_j = \cos(j\pi/N)$ (extreme value coordinates), then as a consequence of (T-1)

$$f_j = \sum_{k=0}^{N} b_k \bar{a}_k \cos(kj\pi/N)$$
$$\bar{a}_k = \frac{2}{N} \sum_{j=0}^{N} b_j f_j \cos(kj\pi/N) \qquad \text{(T-27)}$$

($\bar{a}_k = a_k/b_k$, $b_0 = b_N = 1/2$, $b_1 = \ldots = b_{N-1} = 1$). So, fast cosine transform algorithms (Cooley et al., 1970) can be used for Chebyshev transformations.

4. SUBGRID SCALE MODELS

4.1 Overview

As explained in the introduction, a subgrid-scale (SGS) model becomes necessary if the resolution of our direct numerical simulation scheme cannot resolve all important scales of the turbulent flow. Simply speaking, the SGS model introduces an eddy diffusivity which is dependent on the local flow field. The energy dissipation due to this eddy diffusivity simulates the inertial energy transfer from the scales larger than the smallest resolvable ones to the scales below the resolvable ones and finally to the very fine structure where this energy is dissipated into heat. At very high Reynolds numbers, the magnitude of this SGS energy dissipation can be estimated from simple dimensional analysis. However, since one can only adjust the integral effect of the SGS model, considerable arbitrariness is involved. Again, as explained in the introduction, the accuracy requirements are much smaller here in comparison to statistical turbulence models aiming towards description of all scales of turbulence.

As yet, virtually all SGS models have been developed and applied within finite difference schemes. Application within spectral methods (SM) seems possible. However, the advantages of the SM become less important in this connection because the overall accuracy of the method will then mainly be determined by the SGS model whereas the importance of truncation errors decreases. For the same reason fourth order finite differences would not be principally superior to second order schemes. Moreover, the efficiency of the SM is reduced if a non-linear eddy viscosity is to be computed from any field in addition to the discrete real space velocity and vorticity fields because this would require additional transforms. A very simple SGS model has been applied, however, with success by Siggia & Patterson (1978) in a Fourier SM for the box problem. Here a flow independent eddy viscosity is introduced rather artificially at high wave-numbers.

Perhaps for the first time, SGS models have been introduced in a finite difference scheme by Smagorinsky (1963). The relation to inertial subrange theories has been elaborated by Lilly (1967). Successful application at infinite Reynolds numbers has been reported by Deardorff for Poiseuille flow (1970, 1971, 1973, 1974) and the planetary boundary layer including temperature and moisture transport under gravity. The Poiseuille flow problem has been also investigated by Kau & Peskin (1972) and Peskin (1974). Proper formulation of SGS models for finite difference schemes accounting for the grid geometry (in particular the effect of unequal grid spacings) has been deduced by Schumann (1973a,b,1975a) for momentum and Grötzbach (1977a) for heat transport. They have also developed models which account for the near wall effects (which cannot be modeled by reference to inertial subrange theories) and moderate Reynolds numbers. Grötzbach (1977a) considered cases with $Re \geq 18\,700$ based on the channel width and mean velocity. Moin et al. (1978) adopted these ideas to a simulation with variable grid spacings near the walls for a Poiseuille flow at about the same Reynolds numbers. Both present comparisons to (different) experiments with satisfying agreement.

Fox & Lilly (1972) and Rose (1977) have discussed an obvious drawback of all yet existing SGS models, i.e. the deterministic nature. The models are not able to describe the randomness effects of the fine scale motion on the large scale flow. Although these effects are likely to be small for most properties of the large scale flow because of the net "one-way" energy transfer from large to small scales, they can become important with respect to the predictability question (Herring et al., 1973).

SGS models are presently becoming more and more sophisticated by accounting for all kinds of effects as indicated above. The need for such refinements stems from the desire to get sufficient accuracy at very low resolution (e.g. 16^3 grid points or less). Certainly this approach has the disadvantage of making the models less universal. Also, it is not possible here, to give a self-contained description of the state of the art.

To illustrate the main ideas we subse ntly explain the SGS model for heat transport as developed by Grötzbach (1977a). This model is similar in structure to the SGS momentum transport model of Schumann (1975a). An overview over the complete model is given in Grötzbach & Schumann (1977).

4.2 Temperature SGS Model for FDM

4.2.1 Splitting into "Locally Isotropic" and "Inhomogeneous" Parts

The derivation of finite difference equations in § 2.1 has shown that the fine scale motion results in SGS heat fluxes of the form $\overline{u_j' T'}$, $j = 1,2,3$, where the bar denotes the average over a grid cell surface and the prime the local difference thereof. Far away from walls and at high Reynolds numbers we may assume that the fine scale or subgrid scale turbulence is locally isotropic and possesses an inertial subrange. Near walls, and in fact already quite far away from them, the turbulence and even the fine structure becomes inhomogeneous. Therefore, the SGS flux is split into two parts, termed (I) "locally isotropic" and (II) "inhomogeneous" parts, for both of which a Boussinesq approximation is introduced:

$$\overline{u_j' T'} = \underbrace{-a_t \delta_j \left(\overline{T} - \langle \overline{T} \rangle\right)}_{\text{I}} \underbrace{- a_t^* \delta_j \langle \overline{T} \rangle}_{\text{II}} \qquad (4\text{-}1)$$

The coefficients a_t and a_t^* are eddy diffusivities accounting for locally isotropic and inhomogeneous subgrid scale turbulence, respectively. The time mean value $\langle \overline{T} \rangle$ is split off from part I so that the mean value of $\overline{u_j' T'}$ is zero for the locally isotropic part as it should be in order to be consistent with the assumptions which are used for this part.

4.2.2 Locally Isotropic SGS Eddy Diffusivity

The eddy diffusivities are proportional to a length scale and a fluctuating velocity. For the locally isotropic part, the characteristic length scale is taken from F which is the size of the grid cell surface over which the average (denoted by the bar) is taken. The characteristic velocity is the root value of the SGS kinetic energy (per unit volume) within the area F:

$$\overline{E'} \equiv 1/2 \; \overline{(u_i - \overline{u_i})^2} \qquad (4\text{-}2)$$

This value is taken from a separately integrated differential equation. With these assumptions the model is

$$a_t = c_{T2} \, c_T \, (F \, \overline{E'})^{1/2} / \sigma_T \qquad (4\text{-}3)$$

where σ_T is a parameter which is to be adjusted as described in § 4.4; here we assume $\sigma_T = 1$; c_T is a factor of order one accounting for geometrical anisotropies of the grid and c_{T2} the dominating coefficient. It has to be determined so that the production of SGS temperature variances caused by the isotropic part of the SGS model (4-1, 4-3)

$$\text{production} \sim \langle P_T \rangle \sim \langle \overline{u_j' T'} \, \delta_j \overline{T} \rangle \qquad (4\text{-}4)$$

is equal at least in the statistical mean to its dissipation

$$\text{dissipation} \sim \langle \overline{\varepsilon_T'} \rangle \sim a \left\langle \left(\frac{\partial \overline{T}}{\partial x_j}\right)^2 - \left(\delta_j \overline{T}\right)^2 \right\rangle . \qquad (4\text{-}5)$$

These correlations can be evaluated using the theory of isotropic turbulence (Hinze 1975) if the temperature energy spectrum $E_T(k)$ with $\int_0^\infty E_T(k)\,dk = \langle T'^2 \rangle$ and the energy spectrum $E(k)$ with $\int_0^\infty E(k)\,dk = 1/2 \langle u_i'^2 \rangle$ are known. This evaluation becomes rather complicated if all geometrical details of the anisotropic grid are taken into account. For the comprehensive description of the method of computing c_{T2} and a_t as realized in the computer code TURBIT-2 see Grötzbach (1977a). For demonstration purposes only an approximative formula for an equally spaced grid and large Reynolds numbers is given in the following.

In this special case the characteristic length scale $F^{1/2}$ becomes equal to the characteristic grid width $h = (\Delta x_1 \, \Delta x_2 \, \Delta x_3)^{1/3}$. Therefore using the isotropic part of (4-1) and (4-3) the production (4-4) may be written as:

$$\langle P_T \rangle \approx c_{T2}\, h \langle {}^{j}\overline{E'} \rangle^{1/2} \langle ({}^{j}\delta_j\, {}^{j}\overline{T})^2 \rangle \qquad (4\text{-}6)$$

and the SGS dissipation gets equal to the total dissipation ε_T. The energy and temperature gradient squared in (4-6) is calculated according to the statistical theory of isotropic turbulence:

$$\langle {}^{j}\overline{E'} \rangle \approx \int_{\pi/h}^{\infty} E(k)\, dk \qquad (4\text{-}7a)$$

$$\langle ({}^{j}\delta_j\, {}^{j}\overline{T})^2 \rangle \approx \int_{0}^{\pi/h} k^2\, E_T(k)\, dk \qquad (4\text{-}7b)$$

The complete theory additionally accounts for all averages and for all chosen finite difference approximations. At large Reynolds numbers and at Prandtl numbers near unity both energy spectra are governed mainly by an inertial subrange for which the well known Kolmogorov and Batchelor formulations are introduced (see Fig. 1-2).

$$E(k) = \alpha \langle \varepsilon \rangle^{2/3} k^{-5/3} \qquad (4\text{-}8a)$$

$$E_T(k) = \beta \langle \varepsilon \rangle^{-1/3} \langle \varepsilon_T \rangle k^{-5/3} \qquad (4\text{-}8b)$$

The coefficients α and β are usually assumed to be constants. We use the empirically determined values $\alpha = 1.5$ and $\beta = 1.3$ (Grötzbach 1977a). So finally one gets from the equality of production and dissipation:

$$c_{T2} = \frac{\langle \varepsilon_T \rangle}{h \langle {}^{j}\overline{E'} \rangle^{1/2} \langle ({}^{j}\delta_j\, {}^{j}\overline{T})^2 \rangle} \approx \frac{4}{3\pi\alpha^{1/2}\beta} \left(\frac{2}{3}\right)^{1/2} = 0.22 \qquad (4\text{-}9)$$

This approximative value is somewhat larger than the exact value $c_{T2} = 0.18$ obtained with the complete theory.

For small Peclet numbers ($Pe = Re\, Pr$) the SGS dissipation (4-5) may not be approximated by the total dissipation, because the main parts of the temperature variances dissipate in the directly resolved large scale structure. If one takes the SGS dissipation $\sqrt{\varepsilon_T}$ alone then the dissipation ε does not cancel out from (4-9). In turbulent channel flows ε is

strongly dependent on the distance from the wall and therefore c_{T2} too. It was this extension which made it possible to use the SGS model discussed for calculations of liquid metal flows with very small molecular Prandtl numbers (Grötzbach 1977a, 1977b). (The analogous extension should also be used in the SGS model for momentum if one tries to resolve directly the near wall region down to the viscous sublayer!)

4.2.3 Inhomogeneous SGS Eddy Diffusivity

The inhomogeneity of the flow would have negligible effects on the SGS temperature transport if the sizes of the grid surfaces ${}^{j}F$ were extremely small. However, this limit cannot be accomplished, especially in the near-wall region. Here the characteristic eddy length scale for temperature, i.e. the mixing length ℓ_T, becomes smaller than $({}^{j}F)^{1/2}$. Also, the characteristic velocity is (according to Prandtl) $\ell\, |\delta_i \langle u_i \rangle|$, i.e. the mixing length ℓ for momentum transport times the mean velocity deformation (in finite difference form) which equals the mean velocity gradient in the channel flow situation. According to van Driest (1956) ℓ accounts for wall roughness effects and according to Cebeci (1973) ℓ_T for influences of the molecular Prandtl number. The resultant model is

$${}^{j}a_t^* = \delta_{ij}\, \ell \ell_T\, |\delta_i \langle {}^{i}\overline{u}_i \rangle|\, f_T(h)\, c_{T1c}^{1/2} \qquad (4\text{-}10)$$

with the Kronecker delta δ_{ij} and a damping function f_T which goes to zero for very small mesh sizes h and to one for very large mesh sizes. For details see Grötzbach (1977a). The factor c_{T1c} is varied in the sensitivity study but set to one finally, see § 4.4.

4.3 Boundary Conditions

In § 2.3 we have seen that boundary conditions are required for the wall shear stress components τ_{wi} of the tangential velocity components ($i = 1,2$) and for the normal heat flux at the wall $\dot{q}$. From the underlying boundary conditions (2-11, 2-17) simple finite difference approximations were derived in case of laminar

flow, i.e. under the assumption of nearly linear velocity and temperature profiles in the wall adjacent grid cells. This assumption is no longer valid at high Reynolds numbers where the thickness of the wall adjacent grid cells by far exceed the thickness of the viscous sublayer.

Therefore, additional models are necessary. The boundary conditions used in TURBIT-2 are based on assumptions which guarantee that the wall stresses and heat fluxes are in accordance with common turbulence models at least with respect to the predicted statistical mean values but fluctuate in phase with the wall adjacent grid values:

$$ {}^{3}\overline{\tau}_{1,3}\big|_{w} = \frac{\langle \tilde{\tau}_{w1} \rangle}{\langle {}^{1}\overline{u}_{1}\big|_{1} \rangle} \; {}^{1}\overline{u}_{1}\big|_{1} \qquad (4\text{-}11) $$

Here, $\langle {}^{1}\overline{u}_{1}\big|_{1} \rangle$ is a mean value of the axial velocity in the wall adjacent grid cell where the average is taken over the (homogeneous) plane parallel to the wall and (in case of stationary turbulence) over the past simulation results (a sliding weight is used in which the more recent results appear with more weight than earlier ones which is necessary if the computed turbulence is still non-stationary). The mean wall shear stress $\langle \tilde{\tau}_{w1} \rangle$ for the axial direction is specified as a function of $\langle {}^{1}\overline{u}_{1}\big|_{1} \rangle$ according to empirical laws like the logarithmic velocity profile. For details, see Grötzbach (1977a), p. 68. Similarly, the wall heat flux at large Peclet number flows is specified as

$$ {}^{3}\overline{q}\big|_{w} = \langle \dot{q}_{w} \rangle \frac{{}^{v}\overline{T}_{1} - \overline{T}\big|_{w}}{\langle {}^{v}\overline{T}_{1} - \overline{T}\big|_{w} \rangle} \qquad (4\text{-}12) $$

where either $\langle q_{w} \rangle$ or $\langle \overline{T}\big|_{w} \rangle$ is prescribed from the underlying boundary condition and a relationship between the computational average $\langle {}^{v}\overline{T}_{1} - \overline{T}\big|_{w} \rangle$ and the heat flux $\langle \dot{q}_{w} \rangle$ is obtained from empirical laws (Grötzbach, 1977a, p. 67). At low Peclet and Prandtl numbers we use the linear gradient approximation (2-18).

We are not completely satisfied with this approach because of the heavy dependence on empirical information, the restriction to statistically steady state conditions and the linear (in phase) relationship between wall fluxes and the adjacent grid values. But in the applications these boundary conditions gave sufficient or even good agreement with experiments.

4.4 Sensitivity Study with the Dominating SGS Coefficients

The subgrid scale coefficients are calculated employing the Kolmogorov spectra (4-8) for the total wave number range. It is well known that the real spectra show abrupt transitions to zero energy at very small and very large wavenumbers. The influence of these deviations from the idealized spectra on the subgrid scale coefficients for momentum c_2 are estimated in Grötzbach (1977a, appendix 5). By assistance of the experimental results of Lörcher (1977) it can be shown that for turbulent channel flows with Reynolds numbers between 10^4 and 10^5 the coefficient c_2 has to be enlarged by 25 to 15 %. On the other hand experience has shown that the theoretically determined value of c_2 is even too large by a factor of about 1.4. Therefore one may assume that the coefficient c_{T2} from the subgrid scale model for heat (4-9) has to be corrected too.

Table 4-1: Grid specifications for the calculations of channel flows (IM, JM, KM are the numbers of grid cells in the x_1, x_2, x_3 directions)

grid	X_1	X_2	IM	JM	KM	IM·JM·KM
K7	2	1	16	8	16	2048
K8	2	3	16	16	16	4096
Z2.2	3.2	π	32	32	16	16384
K2.3	4	2	64	32	16	32768

Table 4-2: Case specifications for the calculations of channel flows. (R_{42} = radius of inner, outer cylinder, NT = number of time steps)

Case	grid	R_1/R_2	Re	Pr	NT	CPU-time / min / IBM 370/168	CPU-time / sec / NT IM JM KM
sensitivity study	K7	1	300.000	0.7	1088	~ 20 each	539
Hsu	K7	1	18.700	0.71	2128	39	537
Baumann	K7	1	194.900	7.	1500	29	566
Hinze	K8	1	80.000	0.7	2730	101	542
K3	K2.3	1	250.000	0.7	3224	996	566
Ball	22.2	0.25	25.000	0.7	2625	410	572

For this reason the correction factors γ_T (eq. 4-3) and c_{TK} (eq. 4-10) have been included in the subgrid scale temperature transport model. To find adequate values for these unknown factors a sensitivity study has been undertaken for an infinite plane channel (Fig. 2-1) with a coarsely resolving mesh of only 2048 grid cells (grid $K7$ in Table 4-1). Such a coarse mesh and the high Reynolds number (based on channel width D and bulk velocity) of 300 000 (Table 4-2) was chosen to get very strong influences of the SGS model. For comparison with experimental results from pipe flows the molecular Prandtl number of air was used; the dimensionless volumetric heat source in the fluid was set to $\dot{q}=2$ and zero wall temperature was prescribed.

Several runs have been undertaken with different values for c_{TK} and γ_T. The results are summarized in Fig. 4-1. The main influence comes from the inhomogeneous model. For zero or small values of c_{TK} the maximum temperature and the rms value of the temperature fluctuations decrease and become nearly constant for larger c_{TK}. This growing damping of the large scale temperature fluctuations mainly is what one expects for increasing SGS coefficients. A consistent behaviour is found for the isotropic SGS model. The temperature fluctuations increase with increasing γ_T. But the influence is very weak only.

To find final values for both correction factors the numerical results have to be compared with experimental results. The dashed regions in Fig. 4-1 are taken from the compilation of experimental results by Grötzbach (1977a). The scattering of the data is so large that the only conclusion from this comparison is: c_{TK} should be larger than about 0.5. Therefore $c_{TK}=1$ was chosen arbitrarily, that means no correction is introduced for the inhomogeneous part.

The value of γ_T is fixed so that the SGS turbulent Prandtl number $Pr_{tSGS} = c_2/c_{T2}$ resulting from the approximative theory (§4.2.2) is consistent with the exact theoretical result. Using the same simplified theory as that which resulted in (4-9),

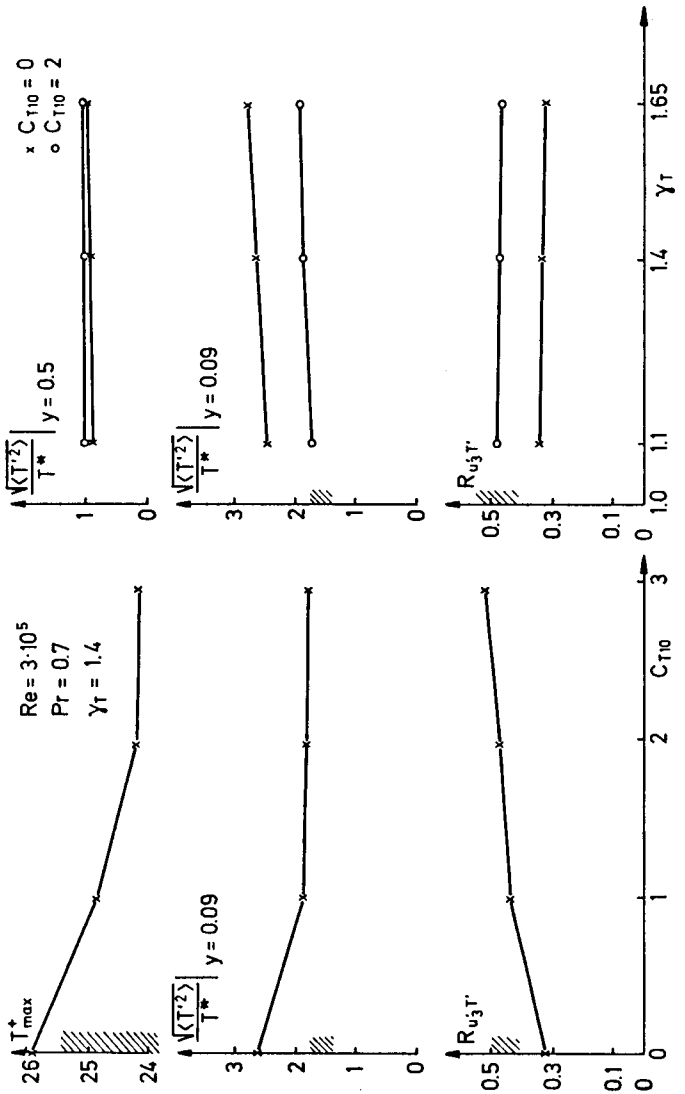

Fig. 4-1 Results from the sensitivity study for the maximum temperature, the rms-values of the temperature fluctuations at different distances y from the walls, and the turbulent heat flux correlation coefficient. T^* is the friction temperature $q_w/(\beta c_p u_z)$.

Schumann (1975 a) found $c_z = 0.044$ for the SGS momentum transport model. This value and the result (4-9) lead to a SGS turbulent Prandtl number of $Pr_{t\,SGS} = c_z/c_{T2} \approx 0.43$. This ratio is in accordance with the experience of Deardorff (1971) that $Pr_{t\,SGS}$ should be between 0.33 and 0.5. Now, the actual value used for c_z in the simulations is reduced by a factor 1.4 in comparison to the theoretically expected exact value. In order to be consistent, the same factor is used for the temperature SGS model, i.e. we use $\alpha_T = 1.4$ for all calculations.

To show that the correction factors deduced above for high Reynolds number flow are also appropriate for low Reynolds number flow, two comparisons with experimental results will be shown. In Fig. 4-2 the numerical result for the mean temperature profile in an annulus with a heated inner wall and an adiabatic outer one is compared with experimental results. The Reynolds number of this case, called "Ball" in Tab. 4-2, is $Re = 25\,000$. The agreement with the experimental data of Lee (1964) and Barrow (1957) is satisfactory except for the results of Ball (1972) which depart probably due to relatively densly located spacers and a rather short thermal entry length. For a plane channel, called "Hsu" in Tab. 4-2, with a Reynolds number of 18 700 only,

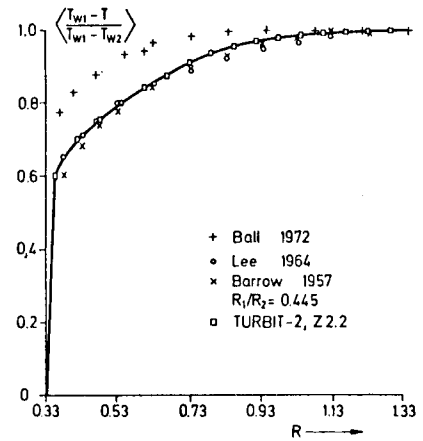

Fig. 4-2 Time mean temperature profile in an annulus, $Re = 25\,000$, case "Ball". The profile is normalized by the wall temperatures at the inner and outer walls (T_{w1}, T_{w2})

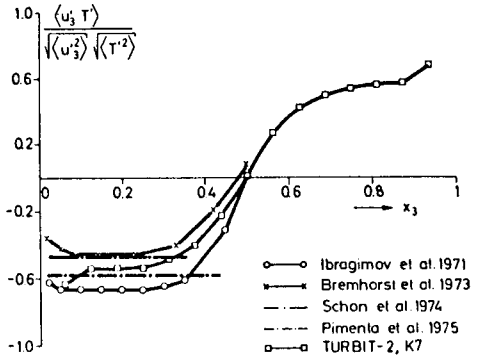

Fig. 4-3 Radial turbulent heat flux correlation coefficient in a plane channel, $Re = 18700$, case "Hsu".

we give the radial turbulent heat flux correlation coefficient in Fig. 4-3. In this case the fluid is heated by a volumetrical heat source within the fluid and cooled at both walls by prescribing constant and equal wall temperatures. For the resulting type of temperature profile no equivalent experimental data are known for a plane channel. We, therefore, refer to the pipe data of Ibragimov et al. (1971) and Bremhorst & Bullock (1973) and to the boundary layer data of Schon et al. (1974) and Pimenta et al. (1975). The numerical results for the heat flux correlation coefficient are well within the widely scattering experimental data. The good agreement shows that the turbulent heat flux is correctly simulated. This is mainly a consequence of the inhomogeneous part of the SGS heat flux model; the sensitivity study above shows (Fig. 4-1) that neglection of the inhomogeneous part ($c_{T4c} = c$) results in higher temperature rms values, which cause smaller turbulent heat flux correlation coefficients.

Further results with respect to varying molecular Prandtl numbers (Grötzbach 1977a, 1977b) show also good agreement with consistent experimental results. As has been shown for example by Lawn (1977) such experiments are likely to show large errors. The numerical results for the temperature fields are rather insensitive with respect to the SGS model coefficients. Thus it is nearly impossible to tune the numerical data in an arguable manner.

4.5 Discussion on e Filtering Approach

In § 2.1 we started by performing the grid cell volume average of the basic equations. By partial integration it was shown that the SGS effects appear in the form of surface averaged Reynolds stresses. Others prefer the filtering approach (Leonard 1974, Ferziger 1977). In this approach one first defines a smoothing operator which serves for filtering out the fine scale motion. When this filter is applied to the basic equations SGS stresses appear in the form of volume averages. In addition the nonlinear terms give rise to non-zero filtered interactions of filtered velocities, the so-called Leonard stresses. Then the filtered equations are solved by an approximative discrete method. This seems to be ideal if the filtered equations could be integrated without any (spatial) discretization errors. Such would be the case, e.g., in a Fourier spectral method (see § 3.2) in which the filter can be defined such that it eliminates all contributions of the fine scale motion above a selected cut-off wave number but does not alter the modes below this cut-off. With finite differences, however, such a filter has not been found yet so that some inconsistency remains. In fact, the filter theories are unable to account for the irregularities introduced by the finite differences. For instance, a mesh cell is never isotropic simply because of its cubic form. Even more, discretization anisotropies appear if non-equal or non-equidistant grid spacings are used in the different space directions. Therefore, to our opinion the filter theory does not offer any advantage rather than it complicates the method and pretends more than actually achieved. Of course, the grid cell average procedure presented in § 2.1 is not free of deficiencies. In particular, here too finite difference approximations are introduced after identification of the SGS terms. But the present method has the advantage that the basic equations are converted into the final finite difference formulation in a formal manner as far as possible. Further, Leonard stresses simply do not appear in the present method.

5. APPLICATIONS

Subsequently several case studies will be reported in which the above methods are applied. Most of the results have been published previously. The purpose of this chapter is to demonstrate the type of applications amenable to direct numerical simulation.

The first two examples are obtained with the Fourier SM described in § 3.2. Here no SGS model is applied. For examples three to six the TURBIT codes are used with and without SGS models.

For each example some results used for verification of the method and some problematic aspects are discussed.

5.1 Pressure Fluctuations in Low Reynolds Number Isotropic Turbulence

5.1.1 The Problem

Pressure fluctuations are of interest with respect to sound generation, turbulent diffusion, structural vibrations and momentum and kinetic energy transport. Experimental investigations of pressure fluctuations are rare because of measurement difficulties. Subsequently, results of a study of pressure fluctuations in isotropic turbulence are summarized which have been obtained using the Fourier-Spectral-Method described in § 3.2 (with $N=32$) for moderate Reynolds numbers without use of subgrid-scale models (Schumann & Patterson, 1978a). The results are comparable to wind tunnel studies of grid generated turbulence.

5.1.2 Case Specifications

Four cases, labeled $I1$ to $I4$, have been studied. The initial velocity field is generated from Gaussian random numbers with a prescribed energy spectrum $\hat{E}(k, t=0)$ (Orszag, 1969). The

main paramet : of the four cases are the form of this spectrum and the initial Reynolds numbers

$$Re_\lambda = v\,\lambda/\nu \qquad (5\text{-}1)$$

where $v = \langle 1/3\ \underline{u}\cdot\underline{u} \rangle^{1/2}$ is the root mean square velocity, λ the Taylor micro scale defined by

$$\lambda^2 = \nu^2 / \langle (\partial u_1/\partial x_1)^2 \rangle \qquad (5\text{-}2)$$

and ν the kinematic viscosity. The parameters are given in the following table:

case	Re_λ	$\hat{E}(k, t=0)$
I1	36	$k^4 \exp(-k^2)$
I2	28	$k^4 \exp(-k^2)$
I3	13	$k \exp(-k)$
I4	4	$k^4 \exp(-k^2)$

Typical run times are 13 minutes on a CDC 7600.

5.1.3 Verification

We first present some of the results which are in accordance with other theories and experiments:

The skewness $S = -\langle (\partial u_1/\partial x_1)^3 \rangle / \langle (\partial u_1/\partial x_1)^2 \rangle^{3/2}$ is a measure for the nonlinear energy transport from small to high wave numbers, see Fig. 5-1. Initially it is zero because of the Gaussian initial values. After a short time it reaches values of the order 0.4 in accordance with measurements of Comte-Bellot & Corrsin (1966) and other theories (Herring & Kraichnan, 1972; Clark et al., 1977). For the very low Reynolds number, case I4, the skewness is reduced due to the strong viscous damping.

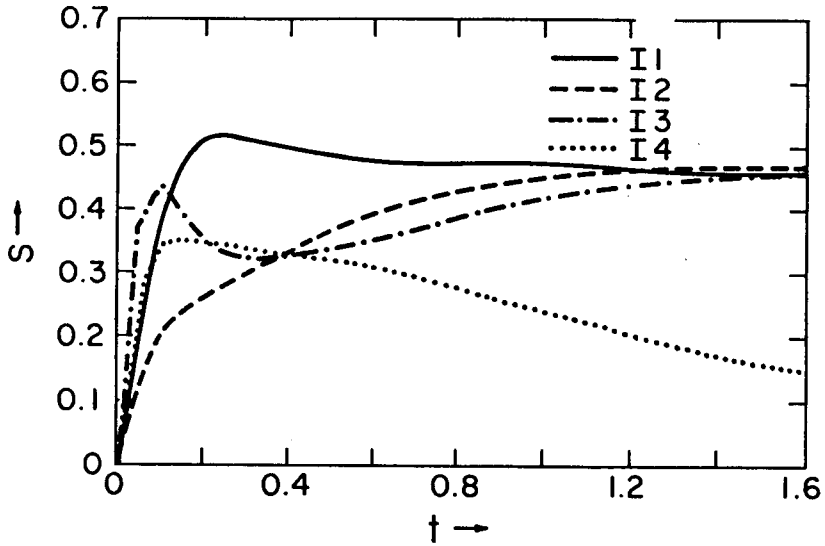

Fig. 5-1 Skewness of the velocity derivative in isotropic turbulence versus time

Several theories and experiments have predicted a decay of the kinetic energy in form of a power law, $E(t) \equiv \frac{3}{2} v^2(t) \sim t^{-n}$, but with different values of n. For example, the measurements of Comte-Bellot & Corrsin (1966) indicate $n = 1.1 \pm 0.2$; Sato & Yamamoto (1974) measured $n \approx 1.5$, while Bennet (1976) measured $n \approx 2.5$. Our numerical results, see Fig. 5-2 give a final power law with $n = (2.5, 1.0)$ in cases $(I1, I3)$. This shows that the exponent n is mainly a function of the initial shape of the energy spectrum.

5.1.4 Problems

A spectrum of the form $k \exp(-k)$ (case I3) is clearly much wider than one proportional to $k^4 \exp(-k^2)$ (other cases). Therefore, in case I3 truncation errors due to insufficient spectral resolution are likely. This becomes obvious from the dissipation spectra $\hat{\varepsilon}(k,t)$ plotted in Fig. 5-3. Whereas the dissipation $\hat{\varepsilon}$ is small at high wave numbers in case I1

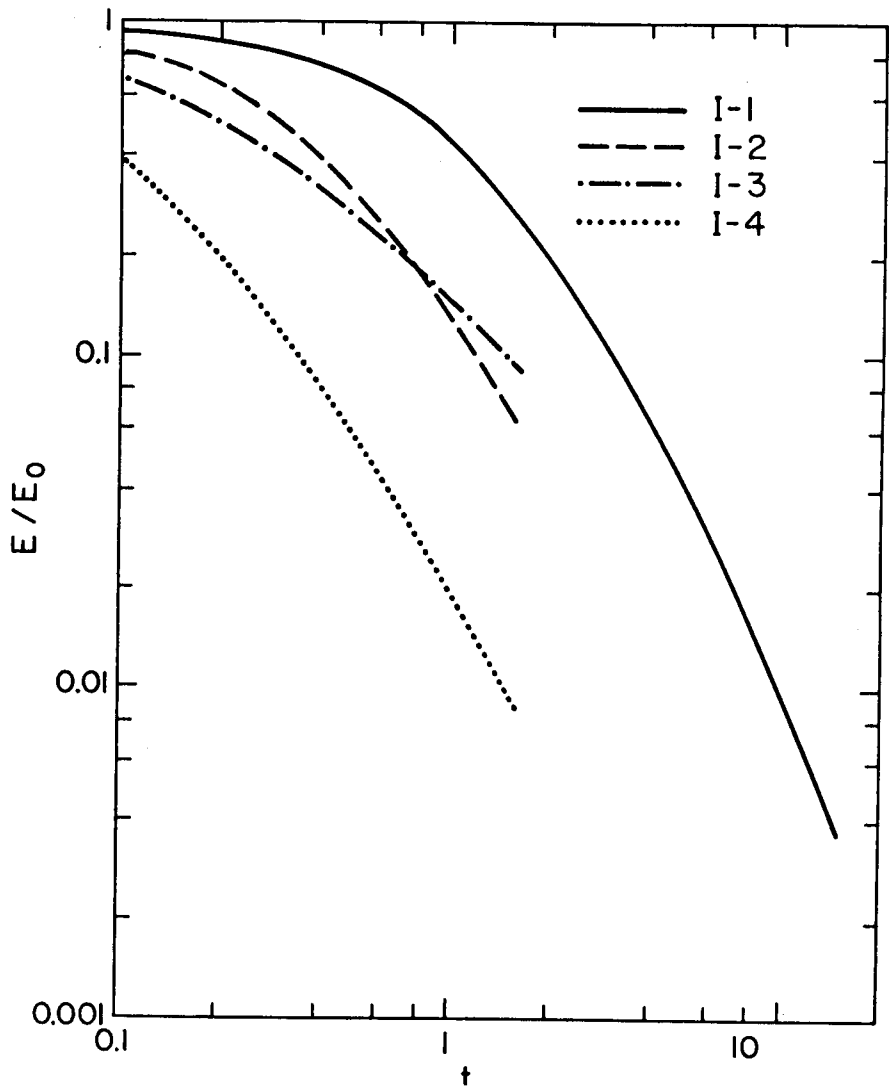

Fig. 5-2 Energy $E(t)$ normalized by $E_0 = E(0)$ versus time showing a final power decay law $E \sim t^{-n}$

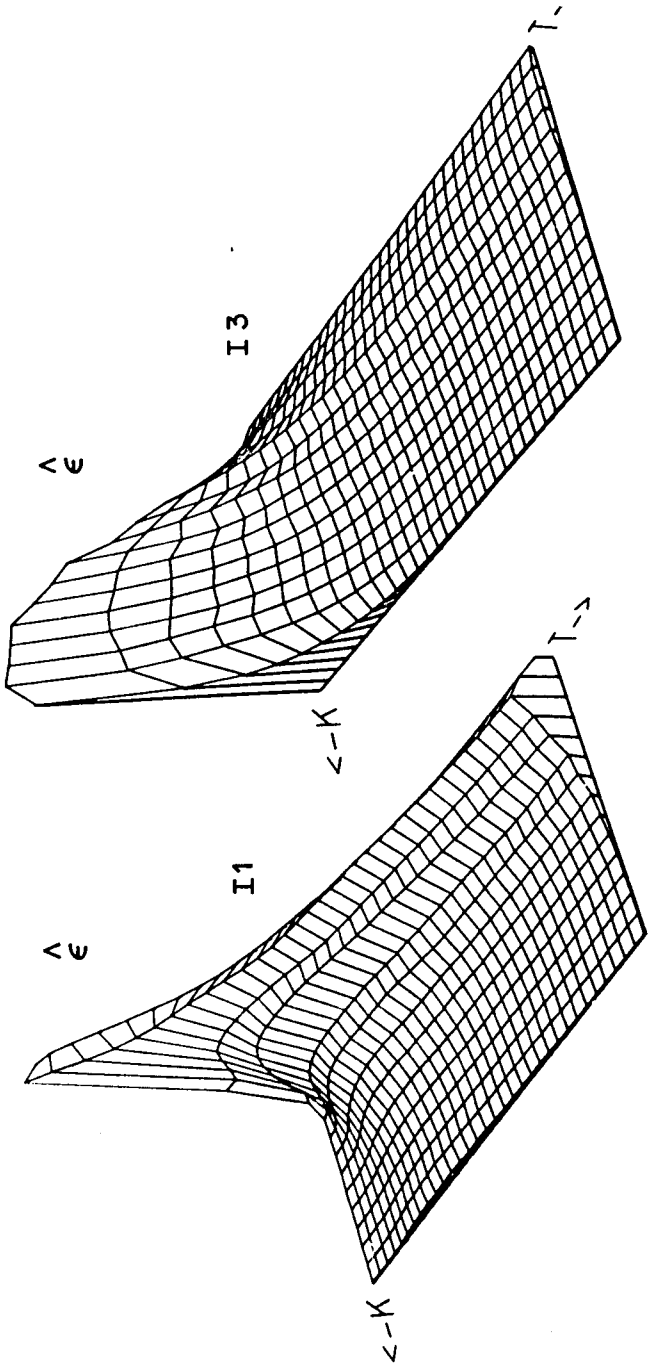

Fig. 5-3 Spectral distribution of energy dissipation rate $\hat{\varepsilon}(k,t)$ for isotropic turbulence. The large values at high wave-numbers k for case I3 indicate truncation errors.

(though having the largest Reynolds number) it is quite large there in case I3. So, case I3 should have been run with a higher maximum wave number, but this would have been very time consuming. The truncation produces errors in the non-linear energy transport as indicated by the reduction of the skewness S for times around $t \approx 0.4$ (non-dimensional) shown in Fig. 5-1.

Another problem arises from the departure from isotropy. If

$$\hat{E}_{ij}(k_c,t) = \sum_{k_c-\Delta k \le |k| < k_c+\Delta k} \hat{u}_i(\underline{k},t)\,\hat{u}_j^*(\underline{k},t) \qquad (5\text{-}3)$$

is the tensorial energy spectrum, then this should be an isotropic tensor $(\hat{E}_{11} = \hat{E}_{22} = \hat{E}_{33}\,;\ \hat{E}_{12} = \hat{E}_{13} = \hat{E}_{23} = 0)$ for isotropic turbulence. However, this is not so completely in the numerical simulation because of the finite number of wave numbers $\underline{k}$ which fall in the interval of summation, see Fig. 5-4.

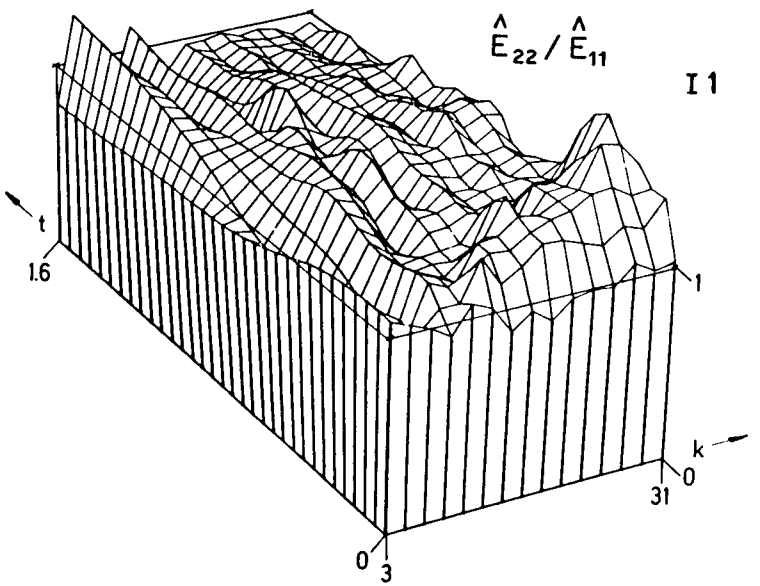

Fig. 5-4 Ratio of energies of the first and second velocity components as a function of wave-number k and time t showing departure from the isotropic value one.

Since the number of discrete modes retained in ₂ simulation varies like k^2, the anisotropy is largest at small wave-numbers. These modes decay slower than the high wave-number modes where the viscous forces are larger. Therefore, the anisotropy grows with time to some extent, limited only by the non-linear energy exchange between the different velocity components due to the pressure forces (see § 5.2). However, similar departures from isotropy have been found in experiments as well, where the initial turbulence is anisotropic at low wave-numbers due to the nature of turbulence generation by a grid (see Bennett, 1976, e.g.).

5.1.5 Pressure Fluctuations - Results

In Fig. 5-5, the computed rms value of the pressure fluctuations is plotted versus time. The results are nearly independent of the initial values. The results are compared in Fig. 5-6 with those reported by Uberoi (1954). The experimental results are derived

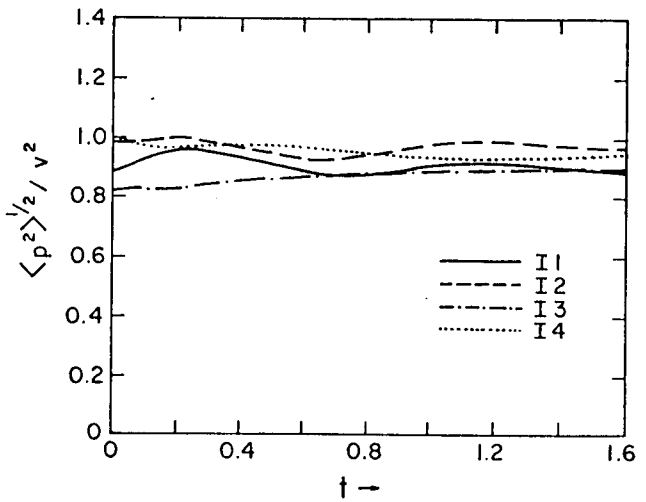

Fig. 5-5 Root-mean-square pressure fluctuations normalized by the mean square velocity fluctuations for different isotropic turbulence runs versus time.

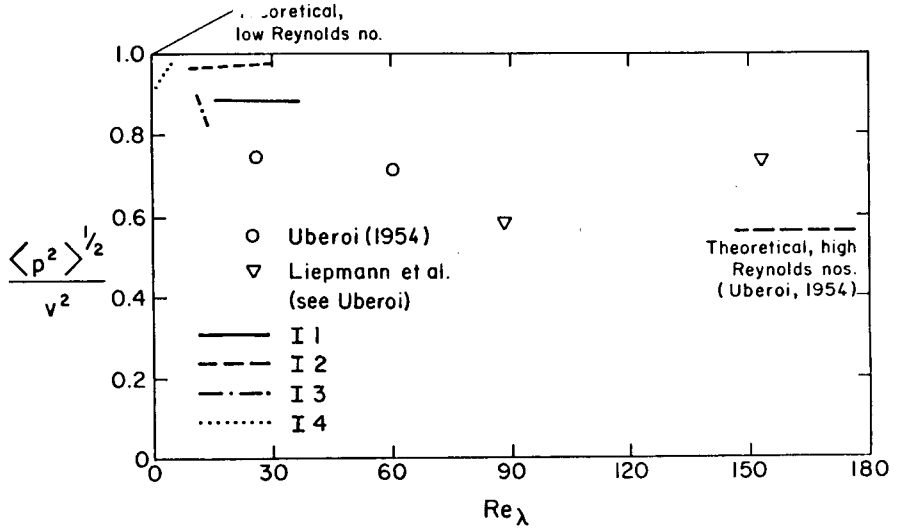

Fig. 5-6 Root-mean-square pressure fluctuations normalized by mean-square velocity fluctuations versus Reynolds number in comparison to experiments and theories.

from second-order velocity correlations assuming Gaussian velocity distributions. The numerical results agree with the theoretical prediction for $Re_\lambda \to \infty$. Fig. 5-7 shows the ratio of microscales λ_p and λ, where λ_p is a measure for the pressure gradients:

$$\lambda_p = \langle p^2 \rangle / \langle (\partial p / \partial x_1)^2 \rangle \qquad (5\text{-}4)$$

Again the theoretical value for $Re_\lambda \to \infty$ is confirmed. Moreover, the scatter of the numerical results appears to be smaller than for the experimental values (for references see Uberoi 1954). For further discussions see Schumann & Patterson (1978a).

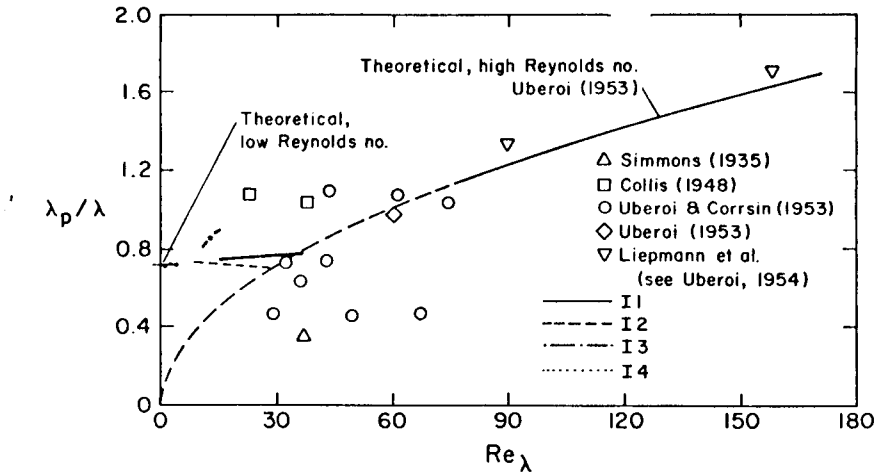

Fig. 5-7 Ratio of microscales λ_p/λ for pressure and velocity fluctuations versus Reynolds number in comparison to experiments and theories.

5.2 Return of Axisymmetric Turbulence to Isotropy

5.2.1 The Problem

The pressure-strain correlation

$$\Phi_{ij} = \left\langle p' \left(\frac{\partial u_i}{\partial x_j} + \frac{\partial u_j}{\partial x_i} \right) \right\rangle \qquad (5\text{-}5)$$

in which p' is the fluctuating pressure with zero mean value affects the energy transfer between the different components of fluctuating velocities and balances the production of shear stresses. Thus, it controls both the relative and absolute magnitude of the Reynolds stresses and is, therefore, one of the most important terms to be approximated in Reynolds stress models of turbulence (see Rotta, 1972, e.g.). The pressure fluctuations tend to produce a return to isotropy. Therefore, one often uses Rotta's (1951) "return-to-isotropy model"

$$\Phi_{ij} = -C \frac{\varepsilon}{E} \Delta E_{ij} \qquad (5\text{-}6)$$

or

$$\Phi_{ij} = -C' \frac{E^{1/2}}{L} \Delta E_{ij} \qquad (5\text{-}7)$$

where ε equals the mean kinetic energy dissipation rate, $E = \langle 1/2\, \underline{u}' \cdot \underline{u}' \rangle$, L is the integral length scale, and

$$\Delta E_{ij} = \langle u_i' u_j' \rangle - \frac{1}{3} \delta_{ij} \langle u_i' u_i' \rangle \qquad (5\text{-}8)$$

is the departure from isotropy of the Reynolds stresses. Simple theories assume C or C' to be universal constants. Subsequently, we first report results of direct spectral simulations of axisymmetrically anisotropic homogeneous turbulence (Schumann & Patterson, 1978b and Schumann & Herring, 1976) from which C and C' are evaluated. Later, a similar analysis of channel flow simulations using SGS models will be described.

5.2.2 Case Specifications

As for isotropic turbulence the decay of turbulence is studied at Reynolds numbers $Re_\lambda \lesssim 40$ using the Fourier spectral scheme of § 3.2 starting from Gaussian random initial conditions. Here, not only the initial kinetic energy but also the initial departure of isotropy is described spectrally. Several cases with different shapes of the energy spectra, different Reynolds numbers and different degrees of anisotropy have been studied. For rigorous definitions much space would be necessary. Therefore, we do not repeat these details; the reader interested in more information is referred to the original papers cited above.

5.2.3 Verification

Most of the cases have been studied also using the Direct Interaction Approximation (DIA), which is a statistical theory

(Kraichnan, 1964), developed for axisymmetric h ogeneous turbulence by Herring (1974). Although this too is an approximative turbulence model, it serves as an independent benchmark. Fig. 5-8 shows the energy $E(t)$ and dissipation $\varepsilon(t)$ versus time for a case with medium anisotropy. Actually, eight runs have been made for the same type of initial conditions differing in the random numbers only. Plotted are the DIA results and the average values ("ensemble mean") of the direct numerical simulation with the standard deviations as deduced from the eight cases indicated by error bars. We see that the results of both methods are in excellent agreement. The initial growth of dissipation is an effect of the nonlinear energy transfer from low to high wave-numbers where the viscous dissipation prevails.

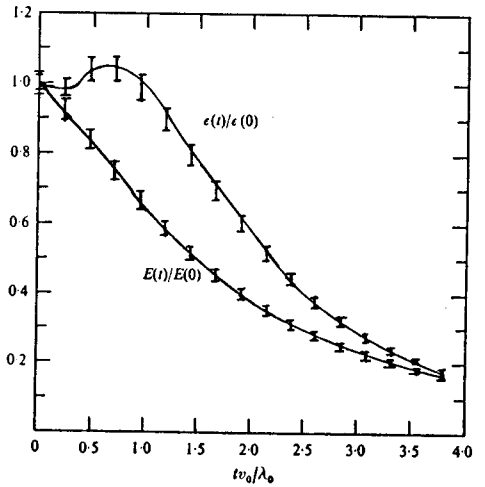

Fig. 5-8 Energy $E(t)/E(o)$ and dissipation $\varepsilon(t)/\varepsilon(o)$ versus time t for axisymmetric turbulence. The error bars indicate the scatter of the results of direct numerical simulations. The curves are for the DIA results.

5.2.4 Problems

The main problems of the direct numerical simulation, which will become obvious in this case, are significant statistical fluctuations about the ensemble mean. The averages taken over the discrete values of the velocity field covered by the SM are not large enough in order to make these mean values equal to the ensemble mean. This is true especially for those quantities which depend sensitively upon the contributions from small wave-numbers where only a few modes are retained. This has been noted already for the isotropic turbulence simulations in § 5.1.4. Statistical errors become even more important if we study effects of small anisotropy because here small differences appear. This in effect virtually excludes applications of the direct numerical simulation to the study of very small departures from isotropy.

5.2.5 Results

Fig. 5-9 shows the evolution of different statistical parameters versus time. These results are obtained from three realizations of extreme initial anisotropy where the u_3-velocity is set to zero initially. The gradual return to isotropy is obvious together with a general decay due to dissipation. Fig. 5-10 shows that a departure from isotropy at some low wave-number results in a pressure-strain correlation at a larger wave-number. This can result in the creation of anisotropy at larger wave-numbers while the low wave-number components are becoming isotropic. Fig. 5-11 shows the computed "Rotta-coefficients" C and C' for several cases. Their values are zero initially as are the pressure-strain correlations for two reasons: First, the initial velocity field is Gaussian and triple correlations are consequently zero. It takes a time of the order $0.2\ L/v$ to build up the triple correlations. Second, from definition, the pressure strain correlation is zero if $\partial u_i/\partial x_j + \partial u_j/\partial x_i = 0$ everywhere as is the case if we start with $u_3 = 0$. Both facts are not accounted for by the simple model (5-6,7). Also, we see that C' is less dependent than C on variations of the

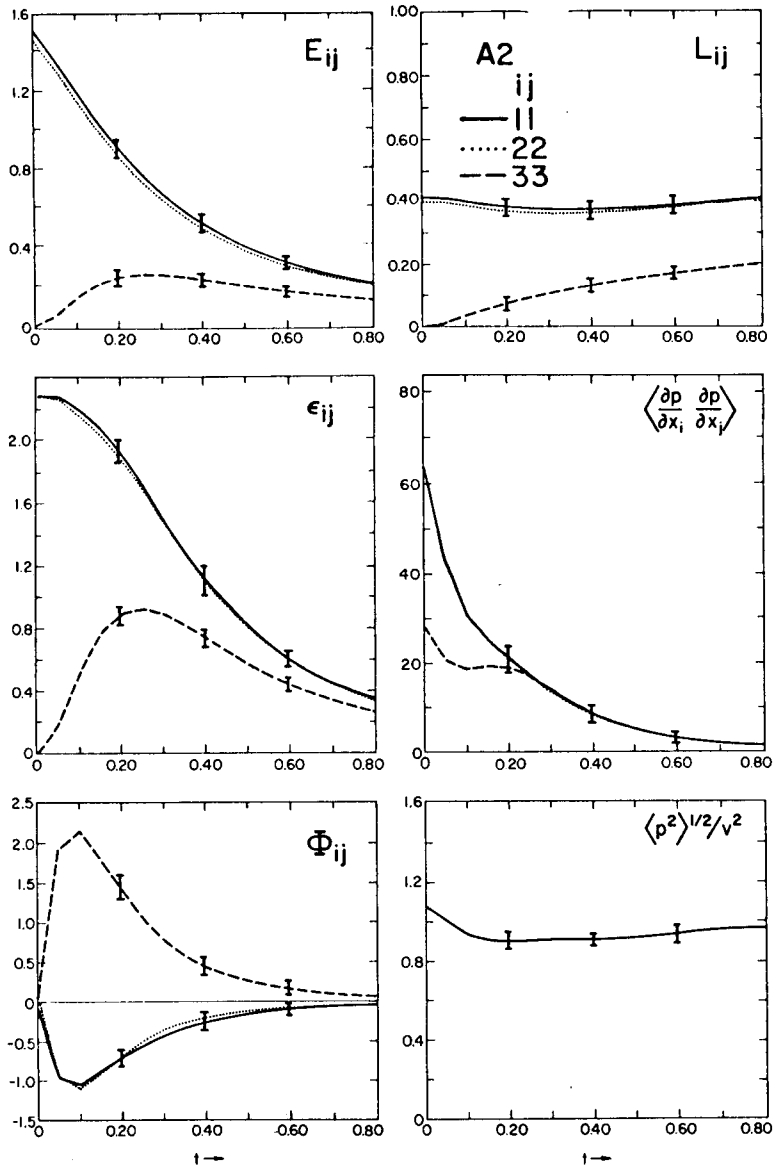

Fig. 5-9 Left column from top to bottom: kinetic energy, dissipation and pressure-strain tensors versus time. Right column: Length scale tensor, mean-square pressure gradients and root-mean-square pressure fluctuations (normalized by the mean-square velocity) versus time for axisymmetric turbulence.

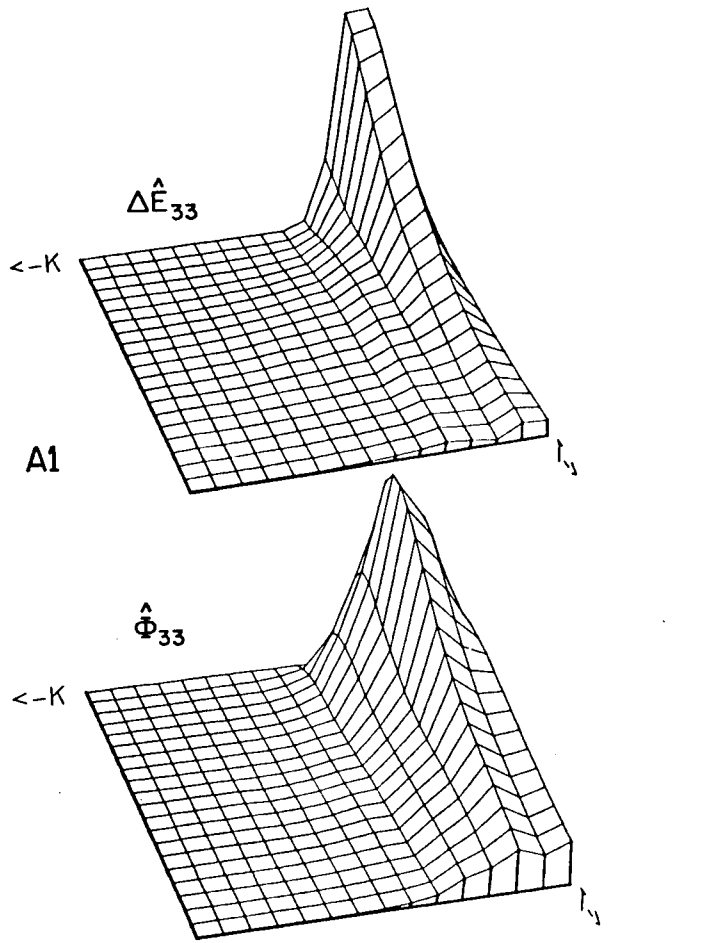

Fig. 5-10 Departure from isotropy for the axial velocity component $\Delta\hat{E}_{33}$ and pressure-strain rate $\hat{\Phi}_{33}$ versus wave-number $k \equiv K$ and time $t \equiv T$

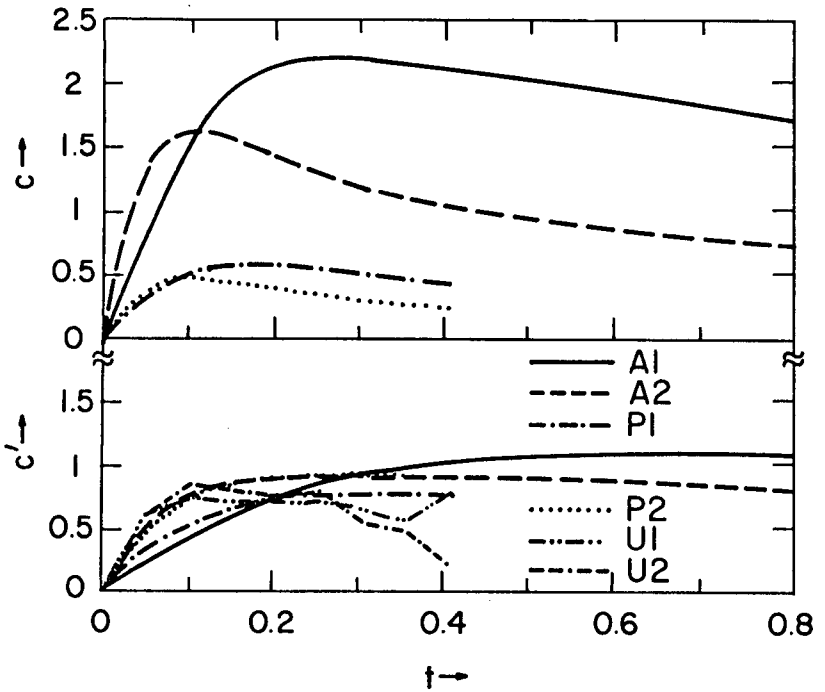

Fig. 5-11 Rotta's constants c and c' (see eqs. 5-6, 5-7) versus time for several axisymmetric anisotropic cases.

initial values. In fact, it appears that c' is virtually independent of the Reynolds number. For very large Reynolds numbers one expects from the inertial range theory that

$$\frac{\varepsilon}{E} \approx A \frac{E^{1/2}}{L} \qquad (5\text{-}9)$$

where A is a constant of order one. From our numerical simulations A is estimated to be in the range $0.6 \leq A \leq 0.9$ (Schumann & Patterson, 1978a). With $c \approx 1.0$ this results in $1.1 \leq C \leq 1.7$ for large Reynolds numbers. This last result well agrees with the value of Rotta's constant used in many empirical turbulence models.

5.3 Pressure-Strain Correlation in Channel Flow

5.3.1 The Problem

The meaning and importance of the pressure-strain correlation has been explained in § 5.2.1. In this chapter we will report results obtained from numerically simulated turbulent channel flows, using the TURBIT-2 code.

Already Rotta (1951) stated that the "return-to-isotropy model", eq. (5-6), is incomplete for shear flows. Additional terms have been proposed (see Launder et al. 1975, e.g.), which are mainly proportional to the mean strain rate using at least one additional constant. Moreover, in confined flows an additional effect which contributes to the pressure-strain is the "wall-suppression" effect: Any fluctuating eddy moving towards the wall is decelerated by the increasing pressure between wall and eddy. This causes energy to be transferred from the normal component to the tangential components. Proposals to account for this effect have been made by Daly & Harlow (1970), Shir (1973), and Launder et al. (1975).

In this chapter it will be shown that a fourth effect exists which influences the pressure-strain correlation. As it is connected with the anisotropic shape of turbulent eddies, we call it "eddy-geometry-effect."

5.3.2 Case Specifications

We consider a plane channel. All dimensional variables are made dimensionless by the friction velocity $u_\tau = (\tau_w/\rho)^{1/2}$ and the distance D between the walls. The grid and other numerical parameters are as given in Table 4-1 and 4-2 for case "K3". The grid resolution is 64x32x16.

From the numerically simulated velocity, pressure and subgrid scale kinetic energy the statistical quantities are evaluated. Here, we assume that the fine-scale structure is suffi-

ciently isotropic so that the pressure-str ı correlation contains no SGS contribution. The Reynolds stresses are computed from the large scale flow and the SGS model. Also, the dissipation rate is determined in this way.

5.3.3 Verification

Experimental data for the pressure statistics in turbulent channel flows have been compared with numerical results from TURBIT-1 in Schumann (1975c) and TURBIT-2 in Grötzbach (1977a). The time mean pressure profiles in the plane channel flows are within the scattering of the experimental data for pipe flows (Grötzbach & Schumann 1977). For the relating profiles in annular flows no experimental data are known to the authors. The rms values of the pressure fluctuations at the wall of the plane channels are in excellent agreement with experimental data too. The two-point correlations of the pressure fluctuations behave as expected by comparison with adequate experimental and theoretical data. The structure of the instantaneous fluctuating pressure fields at the wall of a plane channel (Fig. 5-12) are very similar to the experimental results of Dinkelacker et al. (1977). Both plots are scaled so that the spatial dimensions are directly comparable. In both figures we observe the same spatial extension of the structures which show a 45° inclination against the main stream direction x_1. In addition, the time mean convection velocity of the pressure field at the wall is in agreement with the same experimental results (see Grötzbach 1978c).

5.3.4 Problems

In our time dependent three-dimensional channel flow simulations the averages are taken over planes parallel to the walls and in addition over some different equally spaced time steps in between a prescribed time interval. For the following results of

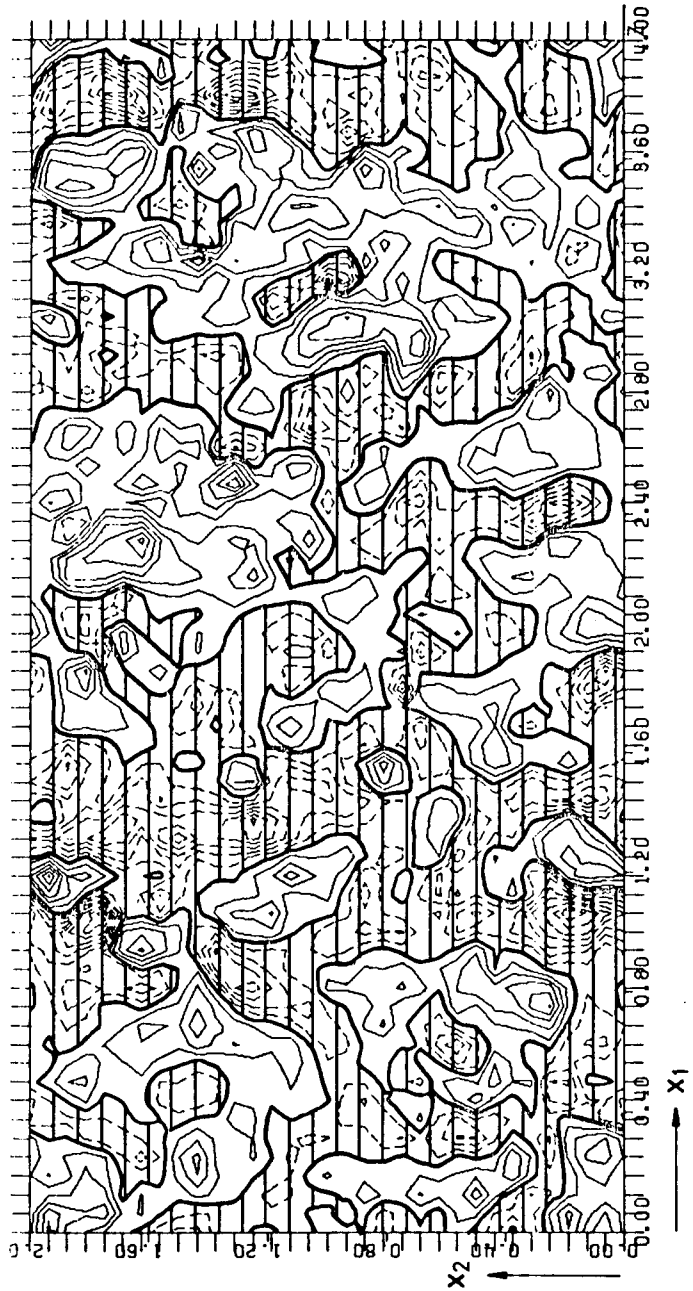

Fig. 5-12 Instantaneous pressure fluctuations at the wall. The dashed regions contain negative fluctuations. Δ is the contour-line increment of the numerical results for case K3

case K3 we used the results from 21 time step ithin a time interval of $\Delta t = \Delta\hat{t}\,\hat{u}_\tau/\hat{\delta} = 0{,}7t$. However, as will be seen from the results, there are still statistical fluctuations. This is mainly a consequence of the energy distribution of the pressure fluctuations in wave number space. Compared to the velocity- or temperature fluctuations the pressure fluctuations are mainly associated with large wave lengths. Therefore, relative large time intervals are necessary for time averaging and relative large periodicity lengths for space averaging. To study such large wave length phenomena quantitatively with high accuracy, larger simulation times or periodicity lengths are desirable.

5.3.5 Results

Fig. 5-13 shows the resultant pressure-strain correlations ϕ_{ij} for different values of i and j . The general behavior is as expected: ϕ_{11} is negative, whereas ϕ_{22} and ϕ_{33} are positive.

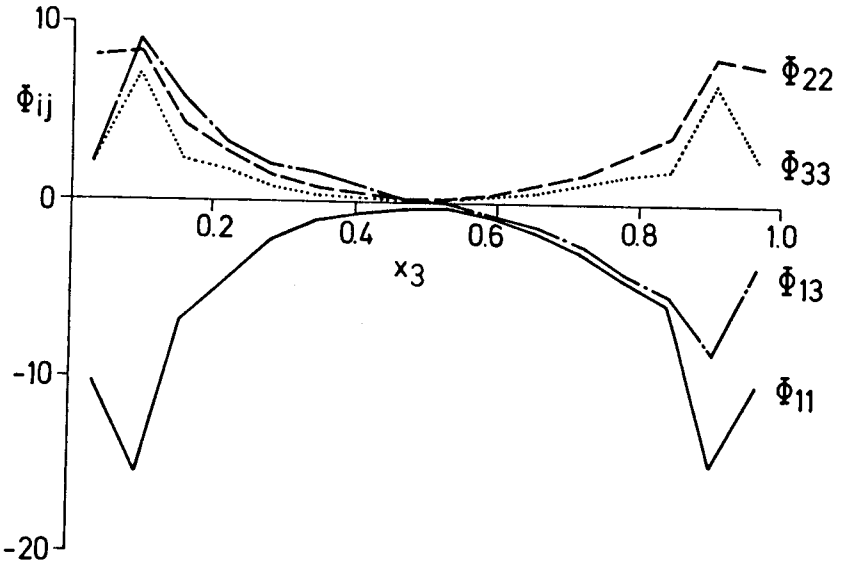

Fig. 5-13 Pressure-strain correlations ϕ_{ij} for high Reynolds number turbulent channel flow versus cross-stream coordinate x_3.

So energy is transferred by this correlation from the axial fluctuations to the other components. The contraction of ϕ_{ii} is zero, which is the consequence of the continuity equation. The sign of ϕ_{13} is opposite that of $\overline{u_1' u_3'}$ so this term acts as the sink term in the conservation law for this stress component. Near the walls the pressure-strain values are reduced. This is partly a consequence of the neglected SGS contributions. Partly it is also a consequence of the wall-suppression effect. In particular ϕ_{33} is much more reduced than the other components due to this effect.

Neglecting the effects of mean strain and of the walls, the constant C appearing in Eq. (5-6) has been calculated out of these results for different values of j and i , and is plotted in Fig. 5-14. Due to the other effects we cannot expect C to be a constant here. But we might have expected to get the same value of C for all values of i and j in the middle of the

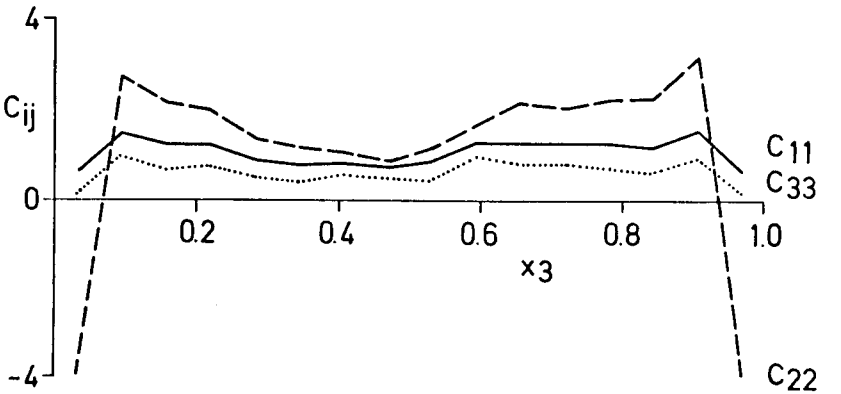

Fig. 5-14 Rotta's constant (eq. 5-6) as obtained from the numerical results for ϕ_{ij} for different indices i and j versus cross-stream coordinate x_3 .

channel where the mean strain is zero and the wall-suppression effect is negligible. Instead, we find

$$C_{33} < C_{11} < C_{22} . \qquad (5\text{-}10)$$

Here we subscript C corresponding to the subscript of $\bar{\phi}_{ij}$ from which it is calculated. Near the walls C_{22} becomes negative as a consequence of the wall-suppression effect.

5.3.6 Discussion: The Eddy-Geometry Effect

In the following it shall be shown that the result of Eq. (5-10) can be explained by deficiencies in the return-to-isotropy assumption, Eq. (5-6). This assumption accounts for the anisotropy in the different mean-square-values of the fluctuating velocities only. However, it is possible to think of a turbulent flow which is anisotropic in these fluctuating velocities despite having zero values of $\bar{\phi}_{ij}$ even for $i=j$. Consider, for example, the Taylor-Green solution for an inviscid two-dimensional flow:

$$u_1 = L_2 \sin(L_1 x_1)\cos(L_2 x_2); \quad u_2 = -L_1 \cos(L_1 x_1)\sin(L_2 x_2); \qquad (5\text{-}11)$$
$$L_1 \neq L_2 ; \qquad u_3 = 0$$

This velocity field satisfies the continuity equation and is steady-state. The pressure-strain correlation is zero, as no energy is transferred from one direction to the other, although the flow is anisotropic.

$$\overline{u_1^2} \sim L_2^2 \neq \overline{u_2^2} \sim L_1^2$$

It looks as though the anisotropy of the different length scales cancels out the anisotropy of the velocity fluctuations. In fact, the quantities $\overline{u_{[i]}^2}/L_{[i]}^2$, $i=1,2$ are "isotropic". A better theory to describe the return to isotropy should therefore account for the anisotropy in the eddy geometry. A relationship which accounts for this effect in a heuristic manner (it is not tensorial invariant) is this:

$$\bar{\phi}_{ij} = -C\,\varepsilon\,\frac{1}{Q_{kk}}\left(Q_{ij} - \tfrac{1}{3}\delta_{ij} Q_{kk}\right)$$

$$Q_{ij} = \frac{\overline{u_i u_j}}{L_{[i]} L_{[j]}} \qquad (5\text{-}12)$$

L_i is any integral length scale proportional to the extention of turbulent eddies in the i-direction. In the denominator of Q_{ij} the bracketed subscripts take the same values as in the numerator. A more rigorous formulation seems to be possible only by introducing an additional empirical constant.

To further support this proposal, let us consider eddies moving in opposite directions as shown in Fig. 5-15. This picture is very similar to that used by Rotta (1951) but here the eddies

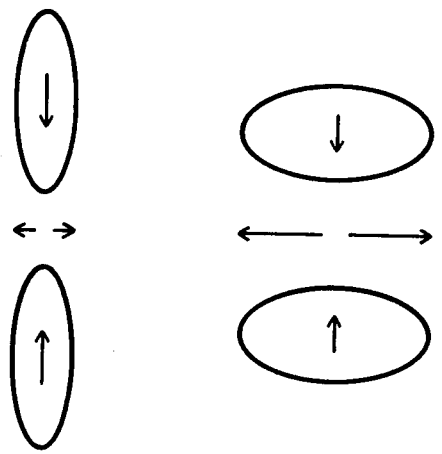

Fig. 5-15 Sketch to explain the influence of the eddy's shape on the pressure-strain correlation.

have different characteristic lengths in different directions. We see from this figure that if the eddies are moving on their axis of elongation, the cross flow velocity caused by the pressure between them is lower than the velocity of the eddies themselves. The converse is true if the eddies move in the direction normal to the axis of elongation. So the energy transfer

from a large fluctuating component to the other is smaller than predicted by Eq. (5-6) if the eddies are elongated in that direction. This results in a relatively small value of the constant C for this direction.

Finally, the present explanation can be supported by the measurements of Champagne et al. (1970). They found for homogeneous shear flow with $\partial\langle u_1\rangle/\partial x_3 > 0$ and a centerline velocity U_c:

$$\left\{ \overline{u_1'^2}^{1/2},\ \overline{u_2'^2}^{1/2},\ \overline{u_3'^2}^{1/2} \right\} = \{ 0.018,\ 0.014,\ 0.013 \}\, U_c$$

and estimated $\{\tilde{\Phi}_{11}, \tilde{\Phi}_{22}, \tilde{\Phi}_{33}\} = \{-2, 1, 1\}\varepsilon/3$. These values result in

$$\{ C_{11},\ C_{22},\ C_{33} \} = \{ 2.4,\ 3.4,\ 1.9 \}$$

if Eq. (5-6) is used, i.e., the same inequality as shown in Eq. (5-10). If we demand a single constant for all three cases using Eq. (5-12), we find for these experimental values a ratio

$$L_1 : L_2 : L_3 = 1 : 0.88 : 0.82$$

for the different length scales and $C = 3$ as the appropriate constant. The experiments show, indeed, $L_1 > L_2 \approx L_3$ if we use the correlation values to estimate L_i.

It should be noted that other models explain the difference in values found for C_{ij} as due to the neglected effect of mean strain. So the above theory is only an alternative to explain this difference for a shear flow. However, the explanation in terms of mean strain does not apply in the middle of the channel because the strain is zero there.

5.4 Turbulent Bénard Convection

5.4.1 The Problem

Most numerical studies of Bénard convection suffer from either of the following deficiencies: they are two-dimensional models or they contain many adjustable model coefficients. Two-dimensional models are unable to resolve turbulence in a sense by

definition. Statistical turbulence models have to undergo the "battle of the constants". However, only very few experimental data on statistical properties are available for this case. The onliest known complete three-dimensional direct simulations from Lipps (1976) ended at the upper end of the transition region from laminar to turbulent flow at a Rayleigh number of $Ra = 20000$. The purpose of our work on this subject is to study high Rayleigh number turbulent natural convection for nuclear reactor safety studies. In a first step we try to determine the resolution requirements for direct simulation of Bénard convection. For later reference in testing SGS models at high Rayleigh numbers we first study lower Rayleigh number cases. Hereby all SGS contributions are set to zero.

5.4.2 Case Specifications

For the numerical simulations the code TURBIT-3 is used, which is an extended version of TURBIT-2, including the buoyancy terms in the momentum- and SGS energy-equation (Grötzbach 1978a, 1979). The SGS models are not used in all following cases. The boundary conditions are approximated in a linear manner as described in § 2.3. Therefore, the results do not depend on any open or empirical parameter. If appropriate grids will be used, there is not a single possibility to tune the numerical results.

Table 5-1: Case specifications for the calculations of Bénard convection in air ($Ra = g\beta\,\Delta T_w\, D^3/(\nu a)$)

Ra	X_1	X_2	IM	JM	KM	NT	CPU-time IBM370/168MVS [min]	$\frac{\text{CPU-time}}{NT \cdot IM \cdot JM \cdot KM}$ [μsec]
1500	2.8	2.8	16	16	8	500	7.5	439
4000	2.8	2.8	16	16	8	1060	15.5	428
7000	2.8	2.8	16	16	8	1060	15.5	428
87300	2.8	2.8	16	16	16	1880	~55	429
381225	(5.6) 2.8	2.8	32	16	16	920	57.7	459

The case specifications for some runs are summarized in Tab. 5-1. For the Rayleigh number we prescribed values from 1500 up to 381225. Using 2.8 and 5.6 as periodicity lengths X_i in the horizontal directions, meshs with 2048 to 8192 grid cells are applied. For the cases with $Ra = 81300$ and greater non-equidistant meshs are used in the vertical direction with the minimum grid width $\Delta x_3 = 0.02$ near the wall. As initial conditions the velocity fields are set to zero, the mean temperature profiles are prescribed linearly, and to start the flow small temperature fluctuations are superposed by a random number generator. The resulting computing times per node and time step are smaller as is in the channel flow calculations (Tab. 4-2) because most of the subroutines containing the SGS models have been replaced by appropriate dummy routines. Thus the TURBIT-3 version used is in principal the equivalence to the code EDDY (§ 2.6).

5.4.3 Verification

One can get a qualitative judgement on the numerical data looking on the flow regimes. The smallest Rayleigh number is smaller than the critical value $(Ra_c \approx 1700)$. The flow field which is caused by the initial temperature fluctuations goes therefore to zero correctly. At $Ra = 4000$ a stationary two-dimensional flow field develops consisting of pairs of eddies with straight horizontal axes. Three-dimensional time-periodic flow fields appear at $Ra = 7000$. The horizontal axes of the pairs of vortices are periodically elongated to serpentines (Fig. 5-16). For the remaining larger Rayleigh numbers the results become three-dimensional and aperiodic. No regular structures can be detected (Fig. 5-17). The flow fields really show turbulence. All these results for the fluid air are in agreement with the flow regime diagram given by Krishnamurti (1973).

For a quantitative verification the numerical results for the Nusselt number are given in Fig. 5-18 together with some experimental data and empirical approximations. The experimental data show very large uncertainties. The numerical data follow nearly exactly the empirical formula from Busse & Whitehead (1974) deduced from an extensive literature overview. Even at the largest

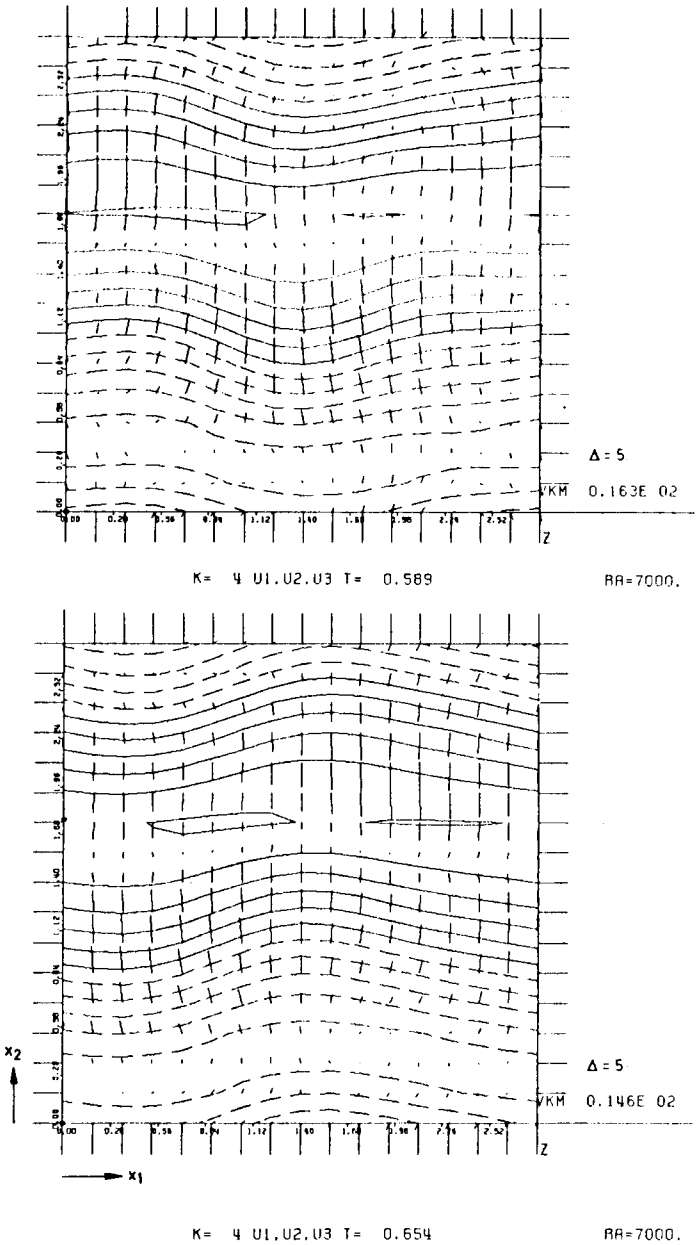

Fig. 5-16 Vector- and contour line plots of the instantaneous horizontal- and vertical velocity fields at two times. Horizontal cut at $x_3 \approx 0.44$ for $Ra = 7000$.

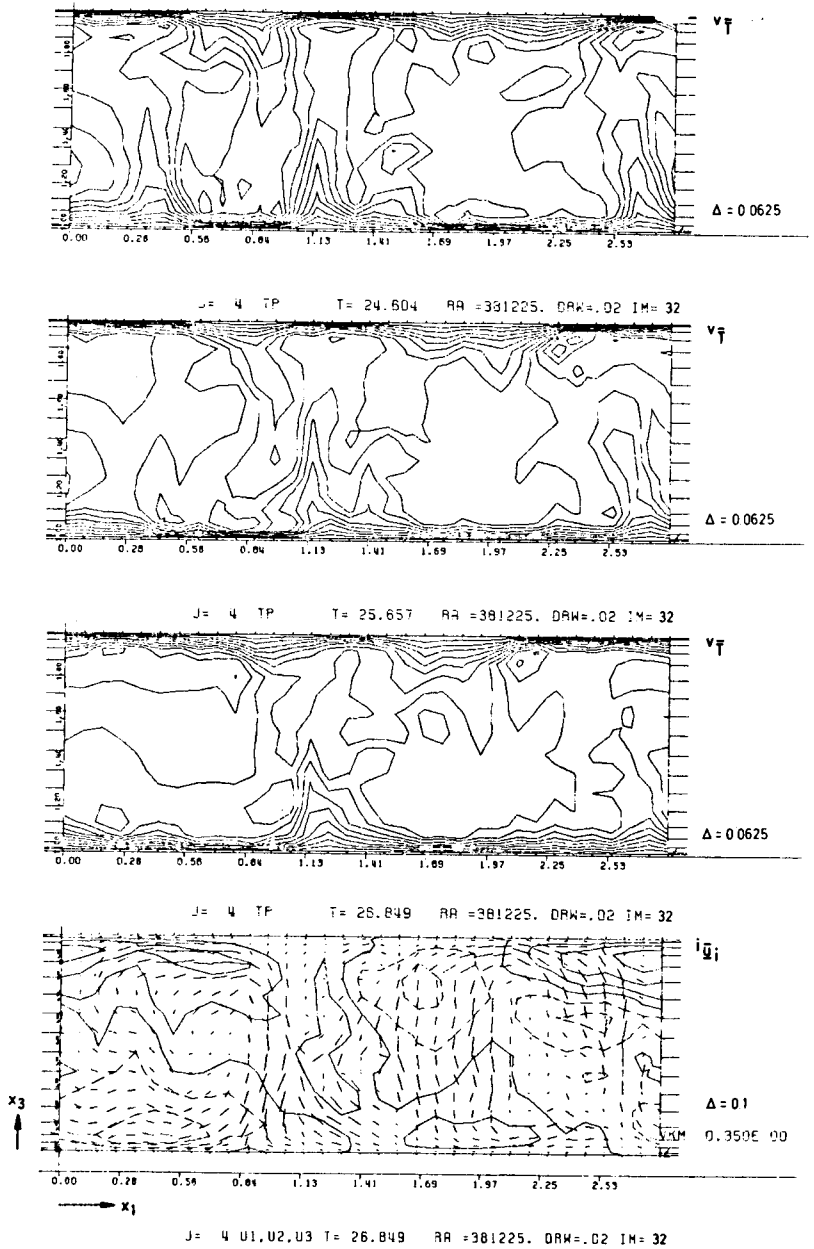

Fig. 5-17 Contour line and vector plots of the instantaneous temperature- and velocity fields at different times. Vertical cut at $x_2 \approx 0.7$ for $Ra = 38\,1225$.

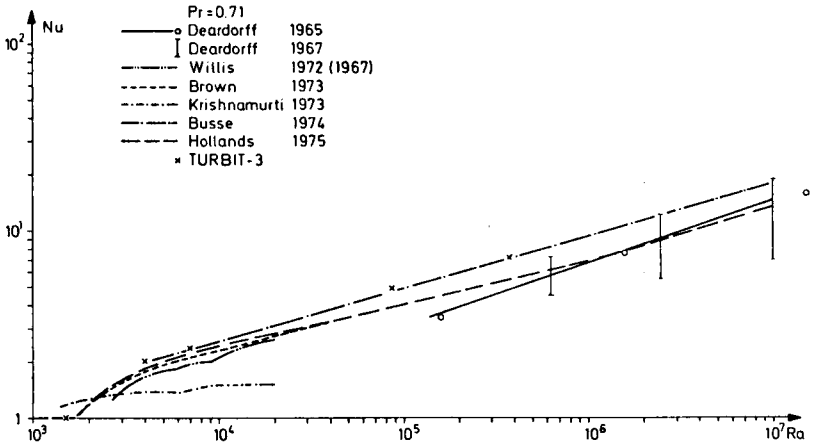

Fig. 5-18 Comparison of numerical results for the Nusselt number in Bénard convection with experimental results.

Rayleigh number the chosen mesh seems to have sufficient spatial resolution. This is also confirmed by the vertical time mean temperature profile for the same case (Fig. 5-19) which is in excellent accordance with the experimental data from Deardorff & Willis (1967). The data from Thomas & Townsend (1957) are in some doubt, because they are not symmetrical to the centre of the channel.

Thus we find excellent agreement with some of the widely scattering experimental data.

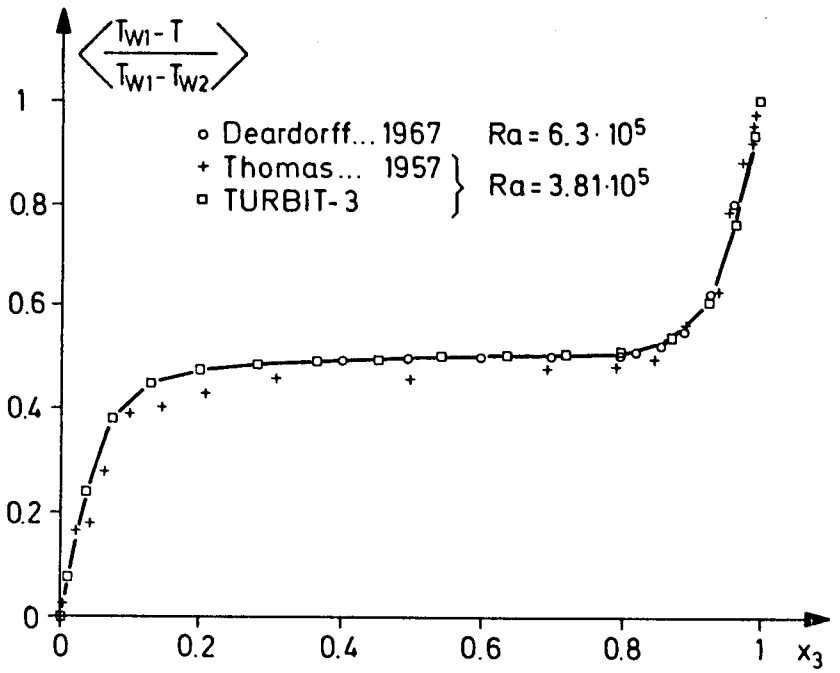

Fig. 5-19 Vertical time mean temperature profile for Bénard convection in air with $Ra = 381225$

5.4.4 Problems

Nevertheless there are still some problems which mainly arise from choosing appropriate meshs. A simpler one is the selection of the vertical grid width near the wall. For this an approximation can easily be done using empirical formula for the Nusselt number, or by some numero-empirical experience. A larger problem arises from choosing adaquate periodicity lengths X_i because it is well known from experiments and theory that the wavelength λ, which is a measure for the possible characteristic eddy size, increases (at small and medium Rayleigh numbers) with increasing Ra. Extrapolation of this behaviour to large Rayleigh numbers

would lead the necessity for large periodicity lengths, and therefore to immense computing times.

Fortunately two phenomena come to help us here: Firstly the numerical results for the low Rayleigh number flows show, that, although the periodicity lengths were not adopted in any way, the numerical results for the Nusselt number are in good agreement with experimental results. The antipodal behaviour was found in two-dimensional simulations and in the results of ambitious statistical turbulence models. It might be suspected that the infinite number of possible wave lengths in real three-dimensional turbulence is the reason for this good-natured behaviour. Secondly the quantitative evaluation of the two-point correlations of the vertical fluctuations from the numerical results shows us that the characteristic eddy size becomes smaller again at larger Rayleigh numbers. Thus the order of magnitude of the chosen periodicity lengths should also be sufficient for larger Rayleigh numbers.

5.4.5 Results

In contrast to the results given in chapter 5.4.3, which were easy to verify, here we add some evaluations of our numerical data which are difficult to verify, but which we need for future tests of our SGS model. In Fig. 5-20 we compare the numerically obtained rms values of the temperature fluctuations with the experimental data from Thomas & Townsend (1957) and Deardorff & Willis (1967). Our maximum value is 30 % greater than that of Deardorff and 160 % greater than that of Thomas. In the core of the channel the numerical results are nearly equal to that of Deardorff. To show the reliability of the numerical result the vertical heat flux correlation coefficient can be used, given in Fig. 5-21. From the experience from channel flows one would expect, that this coefficient should be constant over the whole channel, except of the near wall region, where molecular conduction becomes dominant. Indeed this behaviour is found in the

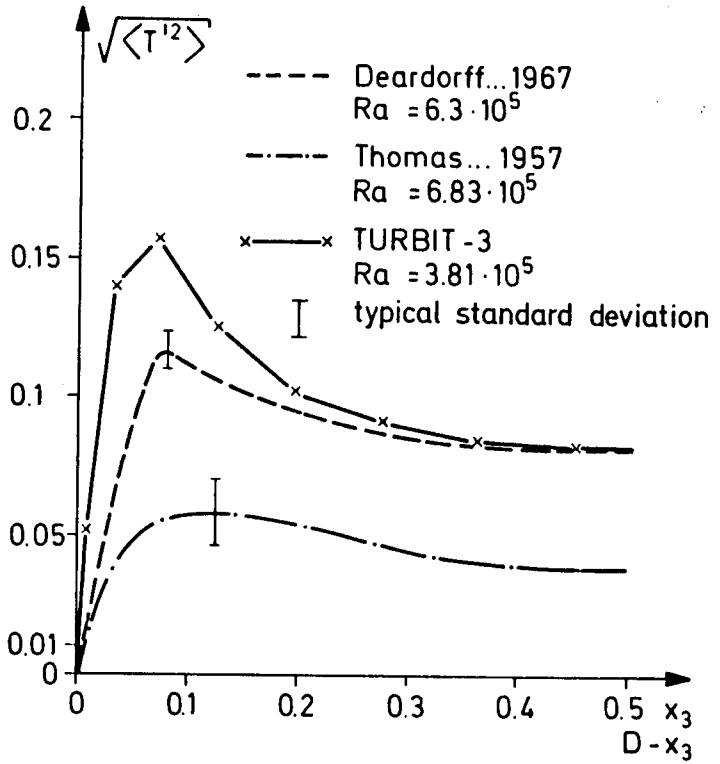

Fig. 5-20 Vertical rms value profile of the temperature fluctuations for Bénard convection in air with $Ra = 381225$, normalized with wall temperature difference.

numerical simulation in more or less satisfying agreement with the experimental data of Adrian (1975). The data of Deardorff are smaller and are not constant in the upper fourth of the channel. It should be noted that the numerical results for the vertical rms velocity fluctuations are in relative good accordance with that of Deardorff. In addition it has been shown above that the Nusselt number, which mainly represents the turbulent heat flux $\langle u_3' T' \rangle$ can be verified. Therefore we are able to conclude that the numerically found rms temperature fluctuations are even more trustworthy than the experimental data cited above.

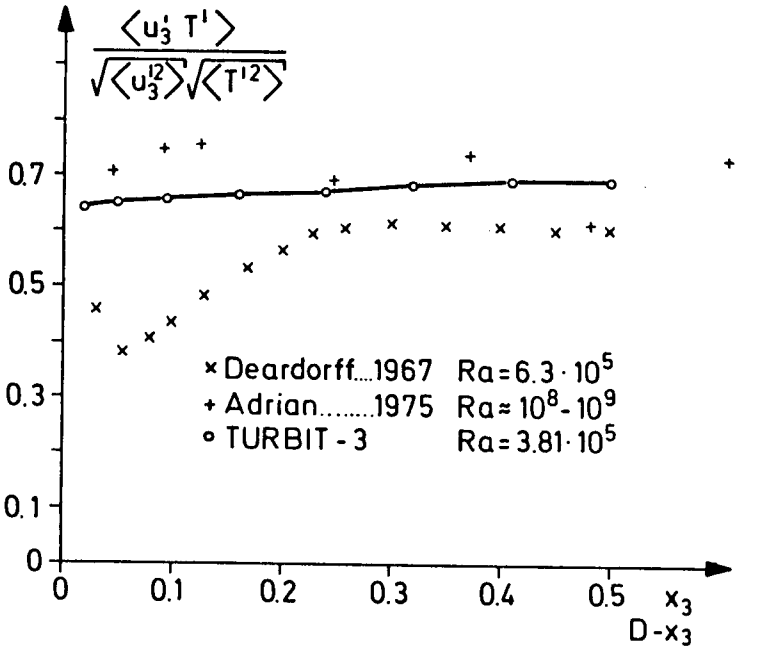

Fig. 5-21 Vertical profile of the vertical heat flux correlation coefficient, corresponding to Fig. 5-20.

5.5 Radial Mixing in Buoyancy Influenced Vertical Channel Flows

5.5.1 The Problem

Within the scope of the reactor safety research programme at the shut down HDR nuclear reactor at Kahl (Fed. Rep. Germany) blowdown experiments shall be performed. They serve to study the fluid- and structure-dynamical loadings on the reactor vessel and its internals in the case of sudden depressurization by rupture of a coolant pipe. As initial condition for these tests one aims at setting a temperature distribution within the vessel which is typical for a water cooled nuclear reactor during normal operation. For this purpose the pressure vessel is fed with two mass flows of different temperatures (Fig. 5-22): A hot water flow $\dot{m}_h$ to the upper plenum and a cooler one $\dot{m}_c$ to the lower plenum. Both water flows are removed through the annular space between core barrel and pressure vessel.

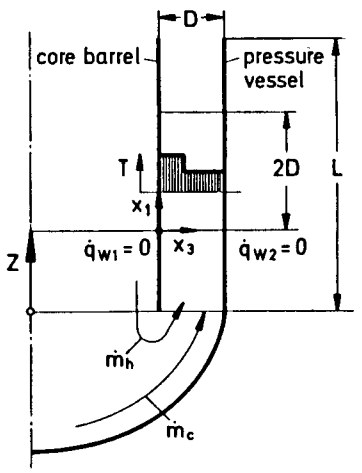

Fig. 5-22 Schematic sketch of the flow paths within the HDR-reactor in setting initial conditions for blowdown experiments. The sketch is not to scale ($D = 0{,}15\,m$, $L = 7.87\,m \approx 50{,}5\,D$).

In planning these experiments it was feared that in the case of non sufficient mixing of both flows in the lower plenum and the annulus secondary currents will be produced by buoyancy influences which lead to nonuniform initial temperature distributions. To investigate these phenomena and the mixing capabilities in the strongly buoyancy influenced pressure driven flow in the annular space the direct numerical simulation code TURBIT-3 has been used (Grötzbach 1978a). It includes the buoyancy influences in the momentum- and SGS energy equation in a consistent manner.

5.5.2 Case Specifications

With the present computer generation it is not feasible to treat the total length $L \approx 50.5\,D$ of the annular space. Therefore we restrict ourselves to a crude approximation only and use the small mesh K7 (see Tab. 4-1) to simulate a control volume with length 2D with periodic boundary conditions within the annular space

moving with the bulk velocity through it (Fig. 5-22). In this approximation the small axial gradients within the adiabatic annulus are not included, but we come to a rather realistic approximation with tolerable computing times (Tab. 5-2).

As a limiting case no mixing of both mass flows has been assumed in the lower plenum. This leads to a step change in the initial conditions for the ensemble mean temperature profile at the entrance to the annular space (see Fig. 5-22) and to zero initial turbulent heat fluxes. For this reason small temperature fluctuations have been superimposed, while the velocity fields have been assumed to be fully developed and were therefore taken from former calculations with the same grid K7. Using the friction velocity u_τ and the wall temperature difference ΔT_w at the entrance for normalization, the friction Reynolds number $Re_\tau = u_\tau D / \nu$ was set to $Re_\tau = 3300$ and the molecular Prandtl number to $Pr = 0{,}89$. To study the influence of the buoyancy forces in the first case no buoyancy was included, that means the initial Grashof number was set to $Gr_{01} = 0$. In the second case $Gr_{01} = -2.27 \cdot 10^{10}$ was used. The Grashof number is negative because the gravitation vector opposes the flow direction.

Tab. 5-2 Some results for the radial mixing investigations; max. denotes the final values of the simulations at the end of the prescribed computing time. NT = number of time steps.

Gr_{01}	NT	CPU-time IBM 370/168 MVS [min.]	t_{max}	$\Delta T_w(t_{max})$	$Gr(t_{max})$
0	1020	18.3	50.38	0.285	0
$-2.27 \cdot 10^{10}$	2280	44.3	32.36	0.0005	$-1.1 \cdot 10^{7}$

5.5.3 Verification

No experimental data are known to the authors which are directly comparable to this special kind of problem. Therefore verification of the numerical data can only be done by analogy. Here we discuss the resulting decay laws for the wall temperature difference along the annulus (Fig. 5-23). In the case of zero buoyancy influence a decrease is found following a $\bar{z}^{-m}$-law with $m = 0.7$. This value for m lies well in between the laws for plane jets with $m = 0.5$ and round jets with $m = 1$ (Chen & Rodi 1978), and is very near to $m = 0.8$ for the adiabatic wall effectiveness in turbulent boundary layers with slot injection (Goldstein 1971) which gives the more relevant comparison. Thus one may conclude that the numerical result is realistic.

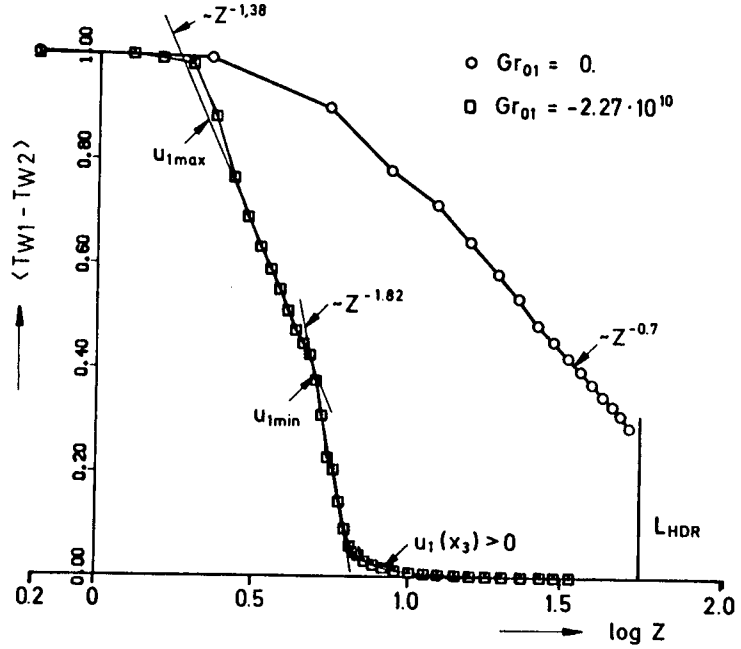

Fig. 5-23 Decay of the wall temperature difference within the annular space. The axial coordinate $\bar{z}$ is defined in Fig. 5-22.

In the case with buoyancy influence we find a steeper decrease with different laws in different regions. The first power law regards to the region where the mixing layer reduces only the temperature at the hot wall. In the second region the power law is steeper because of additional increase of the temperature at the cold wall by the more extended mixing layer. Here the exponent $m = 1.38$ for the first law is nearly comparable to $m = 1$ for plane, and $m = 5/3$ for round buoyant jets (Chen & Rodi 1978). As in the case without buoyancy forces here the numerical result is in between the data for plane and round jets too. For further point-wise verifications using the results for the friction factor or the rms temperature fluctuations the reader is referred to the complete documentation in Grötzbach (1978a).

5.5.4 Problems

It has been discussed above that no axial gradients and no axial coupling in general have been included because of the periodic boundary conditions. This is only one of the problems which reduce the numerical data to qualitative results. A further problem arises from the wall boundary conditions, which do not include any influence of buoyancy on the logarithmic laws of the wall. But, considering that the turbulence production comes here mainly from buoyancy forces within the core of the flow and not from the shear forces near the wall, one may conclude that this leads to minor uncertainties only. This suggestion has been supported by the reliable results for the friction factor.

An additional more general restriction comes from the SGS model. The space dependent results given here are in our simulation time-dependent results, because the control volume is moving through the annulus. But the theory to calculate the SGS coefficients is based only on equations and energy spectra for statistically stationary turbulence. Thus it is possible throughout that the SGS coefficients calculated with the stationary theory

are in some doubt. That the numerical resul are nevertheless quantitatively well within experimental experience shows again that the direct numerical simulation with proper SGS models is very insensitive to model deficiencies.

5.5.5 Results

The detailed radial velocity- and temperature profiles for the first nine channel widths are given in Fig. 5-24. At $\hat{z} = 0$ we start with a fully developed velocity profile and a step change in the temperature profile. For $\hat{z} > 0$ the fluid is accelerated in the hot zone, reaching its local maximum value at $\hat{z} = 2.7$ where the mixing layer in the temperature field reaches the hot wall, and decelerates for larger $\hat{z}$. In the cold zone the fluid is accelerated in the negative $\hat{z}$ direction reaching its maximum value at $\hat{z} = 5$, where the temperature mixing layer reaches the cold wall, and decelerates for larger $\hat{z}$. At $\hat{z} = 9$ the velocity is positive whole over the channel again and the temperature profile is nearly constant. The fast radial mixing is caused by a fast build up of high correlations between radial velocity fluctuations, temperature fluctuations and axial velocity fluctuations, that means by a very fast build up of the radial turbulent heat flux and shear stress. The radial fluxes are more efficient than in the non buoyant case, so that the initially developed flow reversal is suppressed not too far from the entrance. Therefore no extended hot chimney or secondary currents can develop. On the contrary already beyond the half length of the adiabatic channel the temperature differences are leveled out (see Tab. 5-2), so that buoyancy effects are negligible for the upper half of the channel.

Thus in the investigated case of upward forced convection with strong buoyancy influences, the buoyancy forces act as an additional stabilizing factor making the flow distribution within the annular space inherently stable against nonuniformities in the temperature field at the entrance. Therefore no difficulties have to be expected with the chosen method for setting initial conditions for blowdown experiments in the HDR reactor.

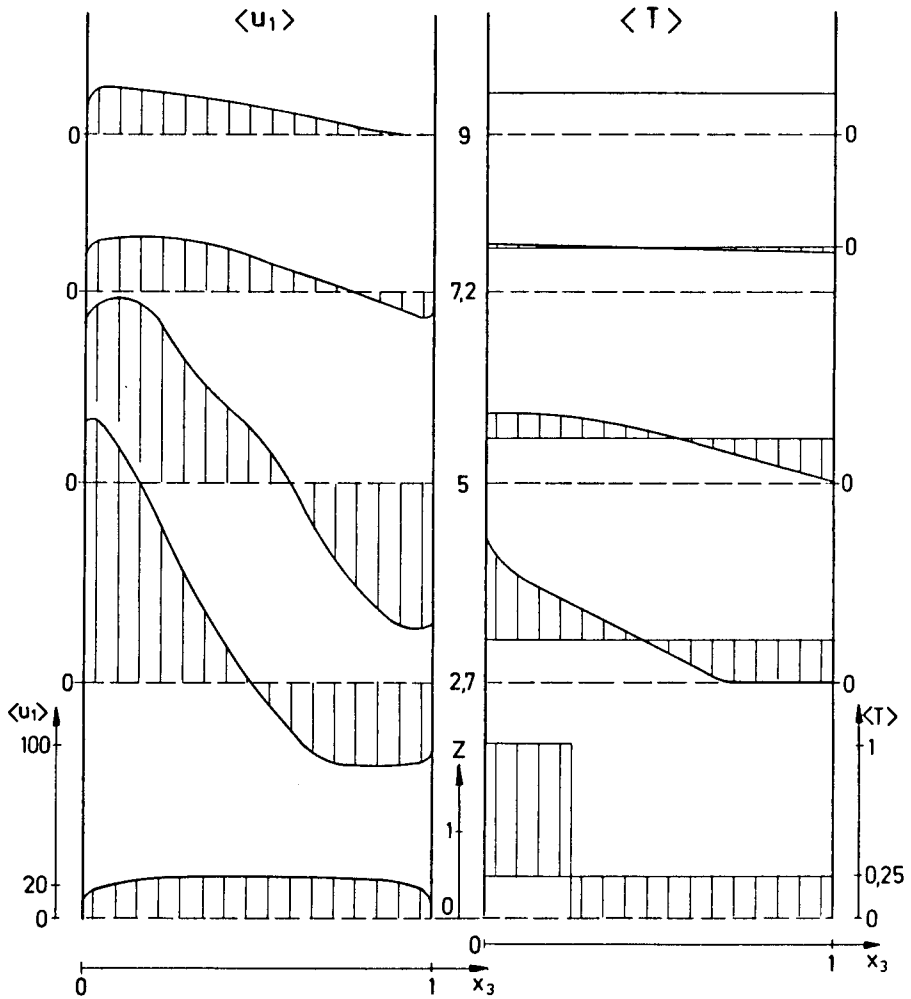

Fig. 5-24 Radial velocity- and temperature profiles for the first nine channel widths within the annular space. The coordinates $\hat{z}$ and x_3 are scaled different.

After closing this theoretical investigation, measurements of the temperature field have been made in the HDR reactor which are in accordance with this conclusion (Mösinger et al. 1978).

5.6 Secondary Flows in Partly Roughened Channels

5.6.1 The Problem

The method of direct numerical simulation of turbulent channel flows with the code TURBIT-2 provides a good possibility to study the effect of secondary currents, which occur in many technical flow problems like in rectangular or square ducts, eccentric annuli, or in fuel elements of nuclear reactors. Some of the models usually used to calculate the detailed flow in such geometries do not include secondary flows, but only non-isotropic eddy diffusivities. Some include secondary flows, but use eddy diffusivities which do not depend on the secondary flow. In some models additional approximative transport equations are used for all Reynolds stresses. Nevertheless all models are of moderate accuracy. This is due to the large number of unknown 'constants' included in the models. By appropriate estimation of these 'constants' from proper experimental results one can reproduce similar numerical results with very different models. But the same values of the 'constants' may not be used for other types of flows or geometries. The models are therefore not universal. The purpose of this chapter is to show that the direct numerical simulation with the code TURBIT-2 is also feasible to treat channel flows with secondary flows caused by wall roughness discontinuities without making any additonal assumptions or corrections (Grötzbach 1978b, 1978d).

5.6.2 Case Specifications

For the verification of the code in the case of rough walled channels an experiment of Baumann has been recalculated. The experiment was performed in a plane channel with one rib-roughened wall. The measured velocity profiles were used to

determine the equivalent sandgrain roughness height $h_1^+ = h_1 Re_\tau / D = 465$. All input data used for the calculation of this test case, called "Baumann", using the grid K7, are listed in Tab. 4-2. To study the consequences of secondary currents on characteristic turbulence data the turbulent flow through a channel with one smooth wall and one wall divided into rough and smooth stripes was calculated. The channel looks like that of Hinze (1973), except for the infinity in the x_2-direction of the channel in the numerical simulation. As a consequence, the pattern of the secondary flow is not directly comparable. With this in mind, to save computing time the lateral periodicity length of the walls was reduced to $X_2 = 3$ (grid K8 in Tab. 4-1). For the same reason the mesh width Δx_2 was chosen to be $\Delta x_2 = X_2 / JM = 3/16$ only. The data given by Hinze are not sufficient to estimate an equivalent sand-grain roughness height for the rough stripes. A crude approximation using the real height of the wall roughness elements gives us $h_1^+ = 180$.

In addition to this input data in both cases the wall roughness height at the second wall was set to $h_2^+ = 0$; the wall temperatures were $T_w = 0$; the volumetrical heat source was set to $\dot{Q} = 2$ to obtain a stationary time mean temperature field. For both cases the complete sets of theoretical values for the SGS coefficients are published in Grötzbach (1978d).

5.6.3 Verification

For the case "Baumann" with one constant roughened wall some typical vector- and contour-line plots are given in Fig. 5-25, which shows the instantaneous fields of the resolved fluctuating velocities, the total turbulence energy, the turbulent pressure, and the resolved fluctuating temperature. The main flow direction is from left to right. The lower boundary represents the roughened wall, the upper boundary the smooth wall. All the contour lines and velocity vectors show the known quasi-random behaviour. The velocity-, energy-, and temperature contour lines show some inclination against the flow direction towards the middle of the channel; this can be observed in all plots of this type. As expected

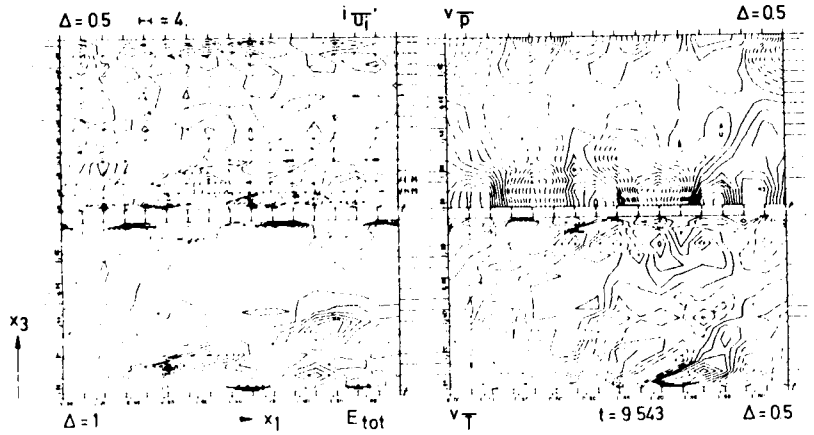

Fig. 5-25 Instantaneous resolved fluctuating velocities $'\overline{u}_i' = {}'\overline{u}_i - \langle {}'\overline{u}_i \rangle$, total energy $E_{tot} = {}'\overline{u}_i'^2/2 + {}^v\overline{E'}$, fluctuating pressure ${}^v\overline{p'}$ and temperature ${}^v\overline{T'}$ in the K7-Baumann channel. Δ = contour line increment; dashed curves correspond to negative values.

from experimental results the fluctuations are larger near the roughened wall than near the smooth wall. A correlation between the pressure field and the other fields is not obvious. Indeed, the quantitative results for this cross-correlations are almost close to zero (see appendix in Grötzbach 1978d).

The time mean value of the velocity profile, calculated from the simulated time dependent velocity fields, is shown in Fig. 5-26. The computed profile is in very good agreement with the experimental data of Baumann (1978), except in the near roughness region. This deviation may be due to the different types of roughnesses (rib roughness with recirculation zones behind the roughness elements in the experiment and sand grain roughness without resolved recirculation zones in the calculation) and due to the different types of variables compared: The experimental data are given as local mean values, while according to § 2.1 the numerical data are given as surface mean values.

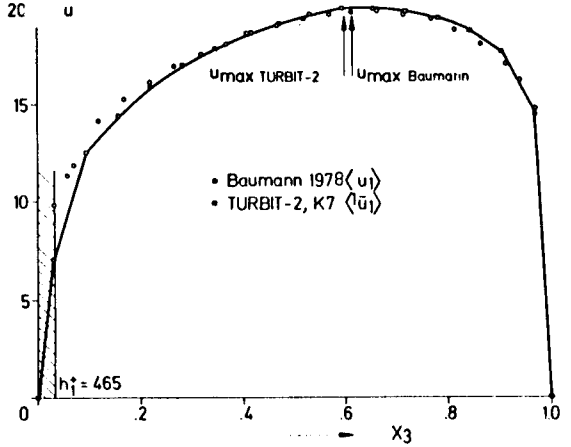

Fig. 5-26 Time mean velocity profile between the rough ($h_1^+ = 465$) and smooth ($h_2^+ = 0$) wall in the constantly roughened channel normalized by the friction velocity u_τ averaged over both walls.

The root mean square values of the velocity fluctuations calculated from the simulated time-dependent velocity fields are shown in Fig. 5-27. As remarked above the fluctuations are larger near the rough wall than near the smooth wall. No experimental data from Baumann are available for comparison. Some measurements of Hanjalić & Launder (1972) have therefore been included to show the general agreement. The experimental data are transformed in such a way, that the minima appear at the same cross-stream position as the minima of the numerical results. This position has been found numerically to lay between the positions of maximum velocity and zero shear stress, perhaps nearer to the last one. This is in qualitative agreement with some experimental results (see complete documentation) but this is discordant to the experimental results of Hanjalić & Launder (1972). These experimental results are anyway not yet fully understood regarding to the behaviour of the rms-values of the x_3 - component beyond the position of the minima.

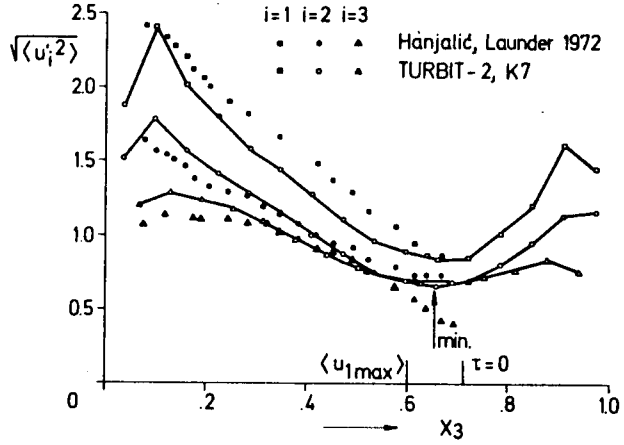

Fig. 5-27 Root-mean-square values of the velocity fluctuations $\sqrt{\langle u_i'^2 \rangle} = \sqrt{\langle \overline{u}_i'^2 \rangle + \frac{2}{3}\langle E^T \rangle}$ in the K7-Baumann channel

The quantitative comparison with some further characteristic data as the position of the maximum velocity, of the zero shear stress, the wall shear stresses and the friction factor shows excellent agreement with the data of Baumann. The deviations are smaller than 3-5 % although a rather coarse grid and a short computing time have been used. The accuracy of the numerical results seems to be comparable to that of experimental results nevertheless.

5.6.4 Problems

Near rough walls the turbulence level is larger than near smooth walls, and the energy spectra become more extended to the high wave number region. By this the SGS models become more important and thus the numerical results more sensitive to model assumptions. In a first calculation for the Baumann channel an Escudier-type formulation of the mixing length in connection with a van Driest damping function was used in the inhomogeneous parts of the SGS model. Using a roughness independent maximum

value for ℓ in the core of the channel this formulation accordingly led to minor accuracy especially in the logarithmic presentation of the velocity field and in the linearity of the radial turbulent shear stress profile. Therefore we changed to the Nikuradse parabola for ℓ in connection with the van Driest damping function which contains no discontinuity in the radial profile of the mixing length. The following second calculation, shown here, immediately was in accordance with the experimental data. Therefore the Nikuradse-type formulation is used now in general for rough and smooth channels, in connection with the same unchanged set of correction factors.

A further problem arises from statistical uncertainties by insufficient time averaging especially in the case of secondary flows which are in the order of 1 % of the main stream velocity that means within the statistical uncertainties of our numerical simulations. Moreover, the averages can not be taken over planes parallel to the walls but only over lines in the x_1-direction. As a result, larger computing times are necessary to find the secondary currents, if at all, in the evaluations of the numerical results. To get reliable results with shorter computing times, at one time step within the time intervall averages have been taken over the resulting time mean fields in a proper way using the symmetry of the Hinze channel. By this means we got qualitatively acceptable results with computing times which were only 50 % larger than those for homogeneous boundary conditions (Tab. 4-2).

5.6.5 Results

In Fig. 5-28 for the case "Hinze" vector- and contour-line plots are given for the time averaged fields of the velocities, the temperature, the resolved parts of the turbulent shear stresses and heat fluxes. The main stream direction is perpendicular to the plots. The roughness discontinuities at the lower wall cause secondary currents in the plane perpendicular to the mean velocity, which are represented by the vectors. For instance in the plane of symmetry in the smooth region the secondary flow

carries fluid of low momentum and temperat from the cooled walls in the cross-stream direction to the middle of the channel. By that means the maxima of mean velocity and temperature do not appear in this region. These maxima are rather found near the boundaries between the smooth and rough stripes in regions, in which the secondary flow is almost zero. In the rough region the secondary flow carries fluid of high momentum from the near smooth wall region to the near rough wall region. The resulting velocity- and temperature fields are more symmetrical in the partly roughened regions of the channel than in the smooth center.

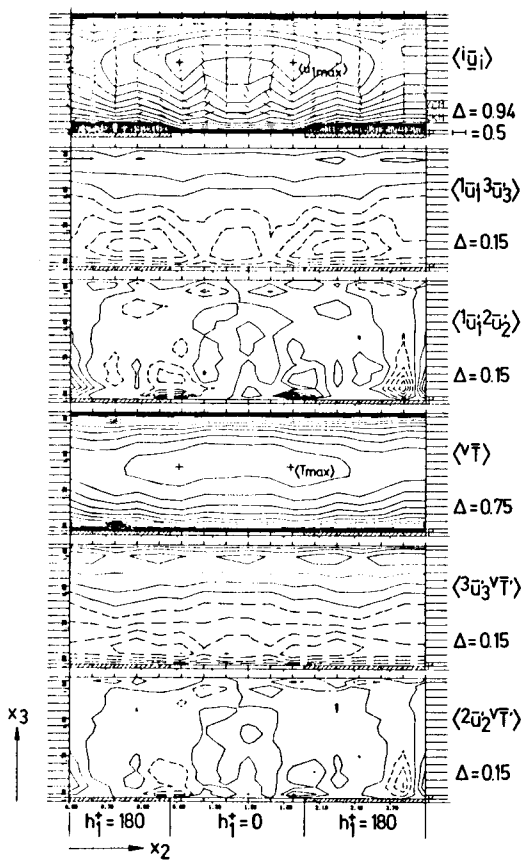

Fig. 5-28
Vector- and contour-line plots of the resolved time mean velocities $\langle {}^{i}\bar{u}_i \rangle$, shear stresses $\langle {}^{1}\bar{u}_1' {}^{3}\bar{u}_j' \rangle$, $j = 2, 3$, temperature $\langle {}^{v}\bar{T} \rangle$, and heat fluxes $\langle {}^{3}\bar{u}_j' {}^{v}\bar{T}' \rangle$ for the case "Hinze". The lower wall is divided into rough $(h_1^+ \approx 180)$ and smooth $(h_1^+ \approx 0)$ stripes. Δ = contour-line increment; dashed curves correspond to negative values.

The isolines of the resolved part of the radial turbulent shear stress $\langle {}^{3}\bar{u}_3' {}^{1}\bar{u}_1' \rangle$ and heat flux $\langle {}^{3}\bar{u}_3' {}^{v}\bar{T}' \rangle$ show regions of constant values especially near the lower wall. Some of the isolines are even parallel to the secondary flow vectors. This behaviour is not so obvious for the lateral turbulent shear stress $\langle {}^{2}\bar{u}_2' {}^{1}\bar{u}_1' \rangle$ and heat flux $\langle {}^{2}\bar{u}_2' {}^{v}\bar{T}' \rangle$ which is mainly dominated by extrema at positions at which the mean flow or temperature field shows larger lateral gradients. Except for these plots most of the isolines are distored in the direction of the secondary flow. It is therefore supposed that the secondary flow is not only carrying momentum and heat, but also other turbulence data like the turbulent shear stress and heat flux. In Grötzbach (1978d) it has been shown that the influence of the secondary currents on the mean velocity and temperature field is different from that on the cross-correlations. Therefore the eddy diffusivities for momentum and heat become convectable quantities too and are dependent on the secondary flows therefore.

6. CONCLUDING DISCUSSION

In the preceding chapters we have given an overview and for some parts a detailed description of the philosophy, the methods, applications and some results of direct numerical simulation of turbulence.

We have stressed the significance of a clear understanding of what is resolved by finite differences because this defines what has to be approximated by SGS models. Here our philosophy is in contrast to other "schools" which start from the definition of filters (see § 4.5).

A general serious problem of direct numerical simulation is the proper formulation of boundary conditions. Because our models are based on the Navier-Stokes equations we have to specify appropriate boundary conditions on all surfaces of our computational domain. It is very difficult to define such conditions for domains extending to infinity. Examples are boundary layers, jets, wakes, inflow and outflow conditions. Here, one has to use either suitable transformations into finite domains or has to change the type of the differential equation from elliptic to parabolic near the boundaries.

As explained in § 3.1 the main advantage of spectral methods are their high convergence order. However, one should not overemphasize this point, because the "infinite" convergence order becomes relevant only after the resolution has been made fine enough to resolve all important length scales of the flow.

Otherwise the accuracy of spectral methods and finite difference schemes are comparable and the former might give unrealistic spatial oscillations. On the other hand, one can expect that sufficient resolution is obtained in the spectral methods with less numbers of degrees of freedom.

The main area for application of spectral methods is the low to moderate Reynolds number range. Studies of decaying homogeneous turbulence have been very successful in this respect.

In the future larger and larger resolutions will be made possible by faster computers (Patterson 1978), optimized programming (Orszag 1976) or simply by spending more computer time. Similar studies for homogeneous shear layers, Poiseuille, Couette and plane boundary layer flows will be done in the near future or have been initiated already.

In fact, one can ask why not to spend, say, a year computing time on perhaps a mini-computer for a special case at Reynolds numbers that are large enough to be of general interest. To our opinion, the reason why this has not been done yet originates from the doubts with respect to the generalizability of the results of such a super-simulation to our understanding of turbulence. But, perhaps one should carry this risk.

Another area of application of spectral methods is the transition problem. Here accuracy plays an essential role because both the non-linear convective forces and the viscous forces have to be analysed with comparable accuracy but the magnitude of the latter is many orders of magnitude smaller as expressed by the high critical Reynolds number. Here SGS models might help to extend the simulations at least a bit further beyond the breakdown into turbulence.

Coming from the other end of the Reynolds number axis, finite difference methods with SGS models remain to be attractive. First, of course, they are considerably simpler to construct. Second their accuracy does not play such an essential role because the convergence order is limited by the importance of the SGS part. Third, they are already now able to produce answers for practical questions at very coarse resolutions. We have shown that even with 16 x 16 x 8 grid points the results of the simulations agree very well with experimental data and the accuracy of the latter is by no means superior in all instances.

At very high Reynolds numbers the SGS models are strictly based on universal turbulence laws like Kolmogorov's inertial spectrum and Prandtl's law of the wall. Approaching the critical

Reynolds number from above, the required number of empirical input data grows but slowly. At the same time the importance of the SGS models decreases because more and more all important effects are resolved.

In comparison to statistical turbulence models, direct numerical simulation offers several advantages. First, it accounts for three-dimensional effects which is essential for turbulence. Second, the SGS models are without doubt more universal so that these methods are truly predictive. Third, at a certain stage, they are simpler and thus more intelligible than the statistical theories which are becoming more and more complicated. Fourth, the pressure - an important quantity in many applications - is much easier accessible. Fifth, SGS models - in particular the simple eddy viscosity models - are free of the realizability problem (Schumann 1977). Sixth, direct numerical simulations can resolve effects like bursts, intermittency etc. in the large scale flow which are very difficult to describe by statistical models. Finally, in some cases at least, direct numerical simulation is no longer more expensive than solution of statistical turbulence models. For example, the Bénard natural convection problem discussed in § 5.4 has been studied by Daly (1974) using a two-dimensional Reynolds-stress model consisting of seven partial differential equations with ten empirical coefficients. The required computing time was ten times larger than the time required by TURBIT-3 for the same parameters.

Regarding the progress made until today, one can expect that direct numerical simulation will become more and more a tool for engineers to study practical problems.

REFERENCES

R.J. Adrian (1975) Turbulent convection in water over ice, J. Fluid Mech. 69, 753-781

A.A. Amsden, F.H. Harlow (1970) The SMAC method: a numerical technique for calculating incompressible fluid flows, LA-4370

H.D. Ball (1972) Experimental investigation of eddy diffusivities of air in turbulent annular flow, Ph. D. thesis, Kansas State Univ.

H. Barrow (1957) Fluid flow and heat transfer in an annulus with a heated core tube, Proc. IME 169, 1113-1124

W. Baumann (1978) Geschwindigkeitsverteilung bei turbulenter Strömung an rauhen Wänden, Dissertation, Univ. Karlsruhe, KfK 2618

J.C. Bennet (1976) Measurements of grid-generated, nearly isotropic turbulence at small Reynolds numbers, Thesis, John Hopkins Univ.

R. Betchov (1975) Numerical simulation of isotropic turbulence, Phys. Fluids 18, 1230-1236

K. Bremhorst, K.J. Bullock (1973) Spectral measurements of turbulent heat and momentum transfer in fully developed pipe flow, Int. J. Heat Mass Transfer 16, 2141-2154

W. Brown (1973) Heat flux transitions at low Rayleigh number, J. Fluid Mech. 60, 539-559

D.M. Burridge, C. Temperton (1977) A fast Poisson-solver for large grids, Submitted to J. Comp. Phys.

F.M. Busse, J.A. Whitehead (1974) Oscillatory and collective instabilities in large Prandtl number convection, J. Fluid Mech. 66, 67-79

T. Cebeci (1973) A model for eddy conductivity and turbulent Prandtl number, J. Heat Transfer 95, 227-234

F.H. Champagne (1978) The fine-structure of the turbulent velocity field, J. Fluid Mech. 86, 67-108, in particular pp. 100/101

F.H. Champagne, V.G. Harris, S. Corrsin (1970) Experiments on nearly homogeneous turbulent shear flow, J. Fluid Mech. 41, 81-139

C.J. Chen, W. Rodi (1978) On decay of vertical buoyant jets in uniform environment, Proc. 6-th Int. Heat Transfer Conf., Toronto, Aug. 7-11,1978

R.A. Clark, J.H. Ferziger, W.C. Reynolds (1977) Evaluation of subgrid-scale turbulence models using a fully simulated turbulent flow, Report No. TF-9, Thermoscience Div., Stanford

G. Comte-Bellot, S. Corrsin (1966) The use of a contraction to improve the isotropy of grid-generated turbulence, J. Fluid Mech. 25, 657-682

J.W. Cooley, P.A.W. Lewis, P.D. Welch (1970) The Fast Fourier Transform algorithm: programming considerations in the calculation of Sine, Cosine and Laplace transforms, J. Sound Vibr. 12, 315-337

J.W. Cooley, J.W. Tukey (1965) An algorithm for the machi calculation of complex Fourier series, Math. Comput. 19, 297-301

B.J. Daly (1974) A numerical study of turbulence transitions in convective flow, J. Fluid Mech. 64, 129-165

B.J. Daly, F.H. Harlow (1970) Transport equations in turbulence, Phys. Fluids 13, 2634-2649

J.W. Deardorff (1970) A numerical study of three-dimensional turbulent channel flow at large Reynolds numbers, J. Fluid Mech. 41, 453-480

J.W. Deardorff (1971) On the magnitude of the subgrid-scale eddy coefficient, J. Comp. Phys. 7, 120-133

J.W. Deardorff (1973) Three-dimensional numerical modeling of the planetary boundary layer, Workshop in Micrometeorology, A.M.S. (ed: D.A. Haugen) 271-311

J.W. Deardorff (1974) Three-dimensional numerical study of turbulence in an entraining mixed layer, Boundary Layer Meteorology 1, 199-226

J.W. Deardorff, G.E. Willis (1965) The effect of two-dimensionality on the suppression of thermal turbulence, J. Fluid Mech. 23, 337-353

J.W. Deardorff, G.E. Willis (1967) Investigation of turbulent thermal convection between horizontal plates, J. Fluid Mech. 28, 675-704

A. Dinkelacker, M. Hessel, G.E.A. Meier, G. Schewe (1977) Investigation of pressure fluctuations beneath a turbulent boundary layer by means of an optical method, Max-Planck-Institut für Strömungsforschung, Göttingen, Bericht 105

E.R. van Driest (1956) On turbulent flow near a wall, J. Aeronaut. Sci. 23, 1007-1011

S.Dütting (1976) Darstellung eines numerisch simulierten turbulenten Strömungsfeldes mit Hilfe von mitbewegten Punkten, Diplomarbeit, Inst. für Reaktortechnik, Uni. Karlsruhe

J.H. Ferziger (1977) Large eddy numerical simulations of turbulent flows, AIAA J. 15, 1261-1267

B.A. Finlayson (1972) The method of weighted residuals and variational principles, Academic Press, New York

B. Fornberg (1975) On a Fourier method for the integration of hyperbolic equations, SIAM J. Numer. Anal. 12, 509-528

D.G. Fox, J.W. Deardorff (1972) Computer methods for simulation of multi-dimensional, nonlinear, subsonic, incompressible flow, J. Heat Transfer 337-346

D.G. Fox, D.K. Lilly (1972) Numerical simulation of turbulent flows, Rev. of Geophys. and Space Phys. 10, 51-72

D.G. Fox, S.A. Orszag (1973) Pseudospectral approximation to two-dimensional turbulence, J. Comp. Phys. 11, 612-619

L. Fox, I.B. Parker (1968) Chebyshev polynomials in numerical analysis, Oxford Uni. Press, London

R.J. Goldstein (1971) Film Cooling, Advances in Heat Transfer 7, 321-379, Academic Press

D. Gottlieb, S.A. Orszag (1977) Numerical analysis of spectral methods: theory and applications, NSF-CBMS Monograph 26, SIAM, Philadelphia

G. Grötzbach (1977a) Direkte numerische Simulation turbulenter Geschwindigkeits-, Druck- und Temperaturfelder bei Kanalströmungen, Dissertation, Uni. Karlsruhe, KFK 2426

G. Grötzbach (1977b) Numerische Experimente zur Untersuchung des Wärmetransports in turbulenter Flüssigmetallströmung, Reaktortagung, Mannheim, 29.3.-1.4.1977, 7-10

G. Grötzbach (1978a) Numerische Untersuchung der Quervermischung bei auftriebsbeeinflußter turbulenter Konvektion in einem vertikalen Kanal, KFK 2648

G. Grötzbach (1978b) Direct numerical simulation of secondary currents in turbulent channel flows, Lect. Notes in Phys. 76, 308-319, Springer Verl.

G. Grötzbach (1978c) Convective velocities of wall pressure fluctuations in a turbulent channel flow deduced from a computer-generated movie, Lect. Notes in Phys. 76, 320-324, Springer Verl.

G. Grötzbach (1978d) Numerical investigation of the influence of secondary flows on characteristic turbulence data, KFK 2553

G. Grötzbach (1979) Direct numerical simulation of laminar and turbulent Bénard convection, to be published

G. Grötzbach, U. Schumann (1977) Direct numerical simulation of turbulent velocity-, pressure-, and temperature-fields in channel flows, Symposium on turbulent shear flows, April 18-20, Pennsylvania State Univ., 14.11-14.19, Proceedings in press, Springer Verlag, to appear 1979

G. Grötzbach, G. Lörcher, U. Schumann (1975) Anwendung und experimentelle Absicherung der direkten numerischen Simulation turbulenter Strömungen, DAtF(ed.) Reaktortagung, Nürnberg, 8.4.-11.4.1975, 145-148

K. Hanjalić, B.E. Launder (1972) Fully developed asymmetric flow in a plane channel, J. Fluid Mech. 51, 301-335

T. Herbert (1977) Die neutrale Fläche der ebenen Poiseuille-Strömung, Habilitationsschrift, Univ. Stuttgart

J.R. Herring (1974) Approach of Axisymmetric Turbulence to Isotropy, Phys. Fluids 17, 859-872, Corrigendum, 19, 167

J.R. Herring, R.H. Kraichnan (1972) Comparison of some approximations for isotropic turbulence, In Statistical Models and Turbulence, Springer Verlag, Berlin, 148-194

J.R. Herring, J.J. Riley, G.S. Patterson Jr., R.H. aichnan (1973) Growth of uncertainty in decaying isotropic turbulence, J. Atmos. Sci. 30, 997-1006

J.O. Hinze (1973) Experimental investigation on secondary currents in the turbulent flow through a straight conduit, Appli. Sci. Res. 28, 453-465

J.O. Hinze (1975) Turbulence, 2nd ed., Mc Graw Hill, New York

C.W. Hirt, J.D. Ramshaw, L.R. Stein (1978) Numerical simulation of three dimensional flow past bluff bodies, Comp. Meth. Appl. Mech. Eng. 14, 93-124

J.K. Hodge (1975) Numerical solution of incompressible laminar flow about arbitrary bodies in body-fitted curvilinear coordinates, Ph. D. Thesis, Mississipi State University

K.G.T. Hollands, G.D. Raithby, L. Konicek (1975) Correlation equations for free convection heat transfer in horizontal layers of air and water, Int. J. Heat Mass Transfer 18, 879-884

M.Kh. Ibragimov, V.I. Subbotin, G.S. Taranov (1971) Velocity and temperature fluctuations and their correlations in the turbulent flow of air in pipes, Int. Chem. Eng. 11, 659-665

C.J. Kau, R.L. Peskin (1972) Numerical simulation of turbulence and diffusion in three-dimensional flow, Rutgers Univ., New Brunswick, New Jersey, Tech. Rept. 101

L. Kleiser, U. Schumann (1978) Simulation of 3D incompressible flows between parallel plates with a Fourier-Chebyshev spectral method, EUROVISC Working Party on Transition in Boundary Layers, Univ. Stuttgart, Oct. 2-3.

W. Kollmann (1972) Berechnung der Turbulenzstruktur in einer Couette-Strömung, Dissertation TH Aachen

A.N. Kolmogorov (1941) The local structure of turbulence in incompressible viscous fluid for very large Reynolds numbers, C.R. Acad. Sci. URSS, 301-305

R.H. Kraichnan (1964) Decay of isotropic turbulence in the Direct Interaction Approximation, Phys. Fluids 7, 1030-1048

R. Krishnamurti (1973) Some further studies on the transition to turbulent convection, J. Fluid Mech. 60, 285-303

B.E. Launder, G.J. Reece, W. Rodi (1975) Progress in the development of a Reynolds-stress turbulence closure, J. Fluid Mech. 68, 537-566

C.J. Lawn (1977) Turbulent temperature fluctuations in liquid metals, Int. J. Heat Mass Transfer 20, 1035-1044

Y. Lee (1964) Turbulent flow and heat transfer in concentric and eccentric annuli, Ph. D. thesis, Univ. of Liverpool

A. Leonard (1974) Energy Cascade in Large-Eddy Simulations of Turbulent Fluid Flows, Adv. in Geophysics 18A, 237-248

D.K. Lilly (1965) On the computational stability of numerical solution of time-dependent nonlinear geophysical fluid dynamics problems, Mon. Weather Rev. 93, 11-26

D.K. Lilly (19 The representation of small-scale turbulence in numerical simulation experiments, Proc. of the IBM Sci. Comp. Symposium on Env. Sci., IBM-Form No. 320-1951, 195-210

F.B. Lipps (1976) Numerical simulation of three-dimensional Bénard-convection in air, J. Fluid Mech. 75, 113-148

G. Lörcher (1977) Laser-Doppler-Messungen von Energiedichtespektren in turbulenter Kanalströmung, Dissertation, Univ. Karlsruhe, KfK 2448

M.D. Love, D.C. Leslie (1977) Studies of sub-grid modelling with classical closures and Burger's equation, Symp. on turbulent shear flows, April 18-20, Pennsylvania, 14.1-14.10

H. Mösinger, H. Schnauder, U. Schumann (1978) Auswertung der Temperaturschichtversuche, unpublished

P. Moin, W.C. Reynolds, J.H. Ferziger (1978) Large eddy simulation of incompressible turbulent channel flow, Report No. TF-12, Thermoscience Div., Stanford

J.W. Murdock (1977) A numerical study of nonlinear effects on boundary-layer-stability, AIAA J. 15, 1167-1173

S.A. Orszag (1969) Numerical Methods for the Simulation of Turbulence, Phys. Fluid, Suppl. II, II-250 - II-257

S.A. Orszag (1971a) Numerical Simulation of Incompressible Flow within Simple Boundaries, I. Galerkin (Spectral) Representations, Stud. Appl. Math. 50, 293-327

S.A. Orszag (1971b) Numerical simulation of incompressible flows within simple boundaries, J. Fluid Mech. 49, 75-112

S.A. Orszag (1971c) Galerkin approximations to flows within slabs, spheres and cylinders, Phys. Rev. Let. 26, 1100-1103

S.A. Orszag (1972) Comparison of pseudospectral and spectral approximation, Stud. in Appl. Math. 51, 253-259

S.A. Orszag (1974) Numerical simulation of turbulent flows, Flow Research Rept. No. 52, M.I.T., Cambridge

S.A. Orszag (1976) Turbulence and transition: a progress report, Lect. Notes in Phys. 59, 32-51

S.A. Orszag, M. Israeli (1973) Numerical flow simulation by spectral methods, in: Numerical Models of Ocean Circulation, Washington (1975), 284-300

S.A. Orszag, M. Israeli (1974) Numerical Simulation of Viscous Incompressible Flows, Ann. Rev. of Fluid Mech. 6, 281-318

S.A. Orszag, L.C. Kells (1978) Transition to turbulence in plane Poiseuille and plane Couette flow, to be published

S.A. Orszag, G.S. Patterson, Jr. (1972a) Numerical Simul. on of Turbulence, In Statistical Models and Turbulence, Springer Verlag, Berlin, 127-147

S.A. Orszag, G.S. Patterson, Jr. (1972b) Numerical Simulation of Three-Dimensional Homogeneous Isotropic Turbulence, Phys. Rev. Let. 28, 76-79

G.S. Patterson, Jr. (1971) Personal communication

G.S. Patterson, Jr. (1978) Prospects for computational fluid mechanics, Ann. Rev. Fluid Mech. 10, 289-300

G.S. Patterson, Jr., S.A. Orszag (1971) Spectral Calculations of Isotropic Turbulence: Efficient Removal of Aliasing Interactions, Phys. Fluids 14, 2538-2541

R.L. Peskin (1974) Numerical simulation of Lagrangian turbulent quantities in two and three dimensions, Adv. in Geophys. 18A, 141-163

M.M. Pimenta, R.J. Moffat, W.M. Kays (1975) The turbulent boundary layer: an experimental study of the transport of momentum and heat with the effect of roughness, Stanford Univ., Rep. HMT-21

A. Pouquet, G.S. Patterson (1978) Numerical simulation of helical magneto-hydrodynamic turbulence, J. Fluid Mech. 85 (1978) 305-323

W.C. Reynolds (1976) Computation of turbulent flows, Ann. Rev. Fluid Mech. 8, 183-208

J.J. Riley, G.S. Patterson, Jr. (1974) Diffusion experiments with numerically integrated isotropic turbulence, Phys. Fluids 17, 292-297

P.J. Roache (1976) Computational fluid dynamics, Hermosa Publ., Albuquerque, 2nd ed.

R.S. Rogallo (1978) An ILLIAC program for the numerical simulation of homogeneous incompressible turbulence, NASA TM-73, 203

H.A. Rose (1977) Eddy diffusivity, eddy noise and subgrid-scale modelling, J. Fluid Mech. 81, 719-734

H.A. Rose, P.L. Sulem (1978) Fully developed turbulence and statistical mechanics, J. de Physique 39, 441-484

J. Rotta (1951) Statistische Theorie nicht-homogener Turbulenz, Z. Phys. 129, 547-572

J.C. Rotta (1972) Turbulente Strömungen, B.G. Teubner V., Stuttgart

P.G. Saffman (1978) Problems and progress in the theory of turbulence, Lect. Notes in Phys. 76, 273-306

Y. Salu, G. Knorr (1975) Use of the spectral method for two- and three-dimensional guiding center plasmas, J. Comp. Phys. 17, 68-78

Y. Sato, K. Yamamoto (74) The local structure of isotropic turbulence, Bull. Fac. Eng., Yokohama National Univ., 23, 91-120

H. Schamel, K. Elsässer (1976) The application of the spectral method to nonlinear wave propagation, J. Comp. Phys. 22, 501-516

H. Schlichting (1965) Grenzschicht-Theorie, Verlag G. Braun, Karlsruhe

J.P. Schon, J. Mathieu, A. Baille, J. Solal, G. Comte-Bellot (1974) Experimental study of diffusion processes in unstable stratified boundary layers, Adv. in Geophysics 18B, 265-272, Academic Press

U. Schumann (1973a) Ein Verfahren zur direkten numerischen Simulation turbulenter Strömungen in Platten- und Ringspaltkanälen und über seine Anwendung zur Untersuchung von Turbulenzmodellen, Dissertation, Univ. Karlsruhe, KFK-1854

U. Schumann (1973b) Results of a numerical simulation of turbulent channel flows, In: M. Dalle-Donne, ANS, ed., Int. Meeting on Reactor Heat Transfer, Karlsruhe,230-251

U. Schumann (1974) Dynamische Datenblock-Verwaltung in FORTRAN, KFK-Ext. 8/74-2

U. Schumann (1975a) Subgrid scale model for finite difference simulations of turbulent flows in plane channels and annuli, J. Comp. Phys. 18, 376-404

U. Schumann (1975b) Linear stability of finite difference equations for three-dimensional flow problems, J. Comp. Phys. 18, 465-470

U. Schumann (1975c) Numerical Investigation of the Wall Pressure Fluctuations in channel Flows, Nucl. Eng. Design 32, 37-46

U. Schumann (1975d) Experiences with the spectral method for three-dimensional turbulence simulations, GAMM-Conf. on Numerical Methods in Fluid Mech. DFVLR Köln, Oct. 8-10, 209-216

U. Schumann (1976) Numerical simulation of the transition from three- to two-dimensional turbulence under a uniform magnetic field, J. Fluid Mech. 74, 31-58

U. Schumann (1977) Realizability of Reynolds-stress turbulence models, Phys. Fluids 20, 721-725

U. Schumann (ed.) (1978) Computers, fast elliptic solvers, and applications, Adv. Publ. Ltd., London

U. Schumann (1979) Fast elliptic solvers and their applications in fluid dynamics, Von Karman Inst. Lect. Ser., Computational Fluid Dynamics, March 13-17, 1978, Hemisphere Corp.

U. Schumann, J.R. Herring (1976) Axisymmetric homogeneous turbulence: a comparison of direct spectral simulations with the direct interaction approximation, J. Fluid Mech. 76, 755-782

U. Schumann, G.S. Patterson (1978a) Numerical study of pressure and velocity fluctuations in nearly isotropic turbulence, submitted to J. Fluid Mech. 88, 685-709

U. Schumann, G.S. Patterson (1978b) Numerical study of the return of axisymmetric turbulence to isotropy, J. Fluid Mech. 88, 711-735

C.C. Shir (1973) A preliminary numerical study of atmospheric turbulent flows in the idealized planetary boundary layer, J. Atmos. Sci. 20, 1327-1339

J.M. Sicilian, A. Leonard (1974) The use of Fourier expansions in turbulent flow simulations, Report No. TF-2, Thermoscience Div., Stanford

E.D. Siggia, G.S. Patterson Jr. (1978) Intermittency effects in a numerical simulation of stationary three-dimensional turbulence, J. Fluid Mech. 86, 567-592

J.S. Smagorinsky (1963) General circulation experiments with the primitive equations, Mon. Weather Rev. 91, 99-164

D.B. Thomas, A.A. Townsend (1957) Turbulent convection over a heated horizontal surface, J. Fluid Mech. 2, 473-492

M.S. Uberoi (1954) Correlations involving pressure fluctuations in homogeneous turbulence, N.A.C.A. Tech. Note No. 3116, See also J. Aero Sci. 20, 1953, 197-204

H. Wengle, J.H. Seinfeld (1978) Pseudo-spectral solution of atmospheric diffusion problems, J. Comp. Phys. 26, 87-106

G.P. Williams (1969) Numerical integration of the three-dimensional Navier-Stokes equations for incompressible flow, J. Fluid Mech. 37, 727-750

G.E. Willis, J.W. Deardorff, R.C.J. Somerville (1972) Roll-diameter dependence in Rayleigh convection and its effect upon the heat flux, J. Fluid Mech. 54, 351-367

A.A. Wray, M.Y. Hussaini, D. Degani (1977) Numerical simulation of transition to turbulence, 2nd GAMM-Conference on numerical methods in fluid mechanics (E.H. Hirschel & W. Geller, ed.) DFVLR, Köln, 247-254

K. Wright (1964) Chebyshev collocation methods for ordinary differential equations, Comp. J. 6, 358-365

Prediction Methods for Turbulent Flows

Edited by

Wolfgang Kollmann

von Karman Institute for Fluid Dynamics

A von Karman Institute Book

HEMISPHERE PUBLISHING CORPORATION

Washington New York London

DISTRIBUTION OUTSIDE THE UNITED STATES

McGRAW-HILL INTERNATIONAL BOOK COMPANY

New York St. Louis San Francisco Auckland Bogotá Guatemala
Hamburg Johannesburg Lisbon London Madrid Mexico
Montreal New Delhi Panama Paris San Juan São Paulo
Singapore Sydney Tokyo Toronto

Prediction Methods for Turbulent Flows

1 2 3 4 5 6 7 8 9 0 L I L I 8 9 8 7 6 5 4 3 2 1 0

Library of Congress Cataloging in Publication Data

Main entry under title:

Prediction methods for turbulent flows.

"A Von Karman Institute book."
"A collection of the notes for a lecture series on prediction methods for turbulent flows held January 15-19, 1979, by the von Karman Institute."
Bibliography: p.
Includes index.
1. Fluid dynamics—Addresses, essays, lectures. 2. Turbulence—Addresses, essays, lectures. I. Kollmann, Wolfgang, date
TA357.P73 532'0527'0184 79-16852
ISBN 0-89116-178-3